

ABSTRACT

Title of dissertation: Measuring topology of BECs
in a synthetic dimensions lattice

Dina Genkina
Doctor of Philosophy, 2018

Dissertation directed by: Professor Ian Spielman
Department of Physics

Measuring topology of BECs in a synthetic dimensions lattice

by

Dina Genkina

Dissertation submitted to the Faculty of the Graduate School of the
University of Maryland, College Park in partial fulfillment
of the requirements for the degree of
Doctor of Philosophy
2018

Advisory Committee:
Professor Ian Spielman, Chair/Advisor

© Copyright by
Dina Genkina
2018

Table of Contents

List of Tables	8
List of Figures	9
1 Introduction	1
1.1 Condensed matter context	1
1.1.1 Topology	2
1.1.2 Band topology in materials	3
1.1.3 Quantum Hall Effect	5
1.1.4 Hofstadter regime	6
1.2 Ultracold atoms for quantum simulation	6
1 Atom Light Interactions	8
1.1 Atomic structure	8
1.1.1 Fine and hyperfine structure	8
1.1.2 Interaction with static magnetic fields	9
1.2 Near-resonant atom-light interaction	14
1.2.1 Rabi oscillations	14
1.2.2 Scattering	17
1.2.3 Adiabatic rapid passage	17
1.3 Far-off resonant atom-light interaction	19
1.4 Absorption imaging	20
1.4.1 Time-of-flight and in situ imaging	23
1.5 One dimensional optical lattices	24
1.5.1 Lattice Hamiltonian	24
1.5.2 Tight binding approximation	28
1.5.3 Pulsing vs adiabatic loading of the lattice	29
1.6 Raman and rf coupling	34
1.6.1 Rf coupling Hamiltonian	34
1.6.2 Raman coupling Hamiltonian	36
1.6.3 Calibration of Raman and Rf dressed states	39

2	Ultracold Gases and the RbK apparatus	45
2.1	Bose-Einstein condensation	45
2.1.1	Phase transition of a non-interacting Bose gas	45
2.1.2	Interacting Bose gas	50
2.2	Degenerate Fermi Gas	54
2.2.1	Fermi statistics and the onset of degeneracy	54
2.2.2	Interactions and Feshbach resonances	56
2.3	RbK apparatus	59
2.3.1	Laser beams	61
2.3.2	Magnetic coils	63
2.3.3	Procedure for making a BEC	65
2.3.4	Changes to apparatus for Rubidium	67
2.3.4.1	Master laser setup	68
2.3.4.2	Alignment imaging path	70
2.3.4.3	FPGA quad servo	74
2.3.4.4	ODT beam shaping	76
2.3.5	Procedure for making a DFG	79
2.3.6	Current status of Potassium apparatus	82
3	Absorption Imaging with Recoil Induced Detuning	89
3.1	Recoil-induced detuning	89
3.2	Perturbative treatment	90
3.3	Stationary atom model	91
3.4	Traveling atom model	96
3.5	Calibration of saturation intensity	97
3.6	SNR optimization	100
4	Direct Imaging of Scattering Near a Feshbach Resonance	103
4.1	Experimental procedure	104
4.2	Data analysis	107
4.3	Results	110
5	Synthetic Magnetic Fields in Synthetic Dimensions	112
5.1	Synthetic dimensions setup	113
5.2	Hamiltonian of the effective 2-D system	116
5.2.1	Hamiltonian	116
5.2.2	Band structure	119
5.2.3	Calibration	122
5.2.4	Tight binding approximation	125
5.3	Eigenstates of the synthetic 2-D lattice	127
5.4	Chiral edge currents	129
5.5	Observation of skipping orbits	132

6	Measuring Chern Number in Synthetic Dimesnions	135
6.1	Experimental procedure	136
6.1.1	Loading procedures	138
6.1.2	Application of force and measurement	139
6.1.3	Density reduction	142
6.1.4	Rf correction	143
6.2	Quantum Hall Effect interpretation	145
6.2.1	Microscoping view of QHE	145
6.2.2	Chern number from Hall conductivity	147
6.2.3	Inadequacy for narrow systems	149
6.3	Measuring Chern number via Diophantine equation	151
6.4	Results and conclusion	155
	Bibliography	157

List of Tables

List of Figures

1	Topology of baked goods	3
2	5
3	6
4	7
5	7
1	Atomic structure of the ground and first excites states	10
2	Energy structure of hyperfine states of ^{87}Rb	12
3	Adiabatic rapid passage (ARP)	18
4	Absorption imaging	21
5	Lattice band structure in the extended zone scheme	27
6	Lattice pulsing	31
7	Lattice pulsing for calibration	32
8	Adiabatic lattice loading	33
9	Raman and rf coupling schematic	35
10	Band structure of the rf Hamiltonian	37
11	Band structure of the Raman Hamiltonian	40
12	Pulsing on rf coupling	42
13	Pulsing on Raman coupling	43
1	Occupation of energy states of a 3-D harmonic oscillator	48
2	Time-of-flight images of atoms	49
3	In situ measurement of a fraction of bose condensed atoms	53
4	Occupation number as a function of energy for a Fermi gas	56
5	Schematic of a Feshbach resonance	58
6	Photograph of RbK apparatus at NIST Gaithersburg	60
7	Schematic of RbK apparatus	62
8	Schematic of magnetic coils on the RbK apparatus	64
9	New master board layout	68
10	Schematic of the bottom half of the alignment imaging system	71
11	Schematic of the new imaging lens	72
12	Schematic of the top half of the alignment imaging system	73
13	Turn on and off curves of the quad coils	77

14	Output current as a function of computer command voltage	78
15	Schematic of beam shaping optics in the path of the 0th order ODT beam	78
16	Beam waist as a function of propagation distance	80
17	Schematic of the 2D MOT setup	84
18	Picture of 2D MOT cell	85
19	Schematic of 2D MOT optics	87
20	Picture of current 2D MOT apparatus	88
1	Recoil induced detuning	92
2	Optical depth as a function of probe intensity	94
3	Checking stationary atom assumption	95
4	Phase space evolution of the atomic cloud	98
5	Comparison of stationary and moving atom simulations	99
6	Signal-to-noise optimization	102
1	An sample absorption image after 6.8 ms TOF	107
2	Experimental setup and inverse Abel transform	108
3	Normalized scattered population vs bias field B	111
1	Setup of effective 2-D lattice	114
2	Band structure of the synthetic dimensions Hamiltonian	120
3	Calibration of synthetic dimesnions lattice	123
4	Band structure of the tight binding versus full Hamiltonian	126
5	Eigenstates of the synthetic dimensions lattice	128
6	Measuring chiral currents in synthetic dimensions	131
7	Imaging skipping orbits	133
1	Quantum Hall effect in Hofstadter ribbons	137
2	Band structure of the lattice-coupled system in $F = 2$	139
3	Application of a constant force by displacing a Gaussian beam potential	140
4	Band structure in a 5-site wide ribbon	141
5	Correction of oscillations in rf coupled data	144
6	Hall displacement	148
7	Band structure of the synthetic dimesnions lattice with flux $\Phi/\Phi_0 = -4/3$	150
8	Chern number from the TKNN equation	152
9	Calculating Chern number	154
10	Chern number measurement	155

Chapter 1: Introduction

Although quantum mechanics has been well established since the early 20th century, there are still many quantum phenomena that are not well understood and are not easy to calculate. These include high temperature superconductivity, fractional quantum Hall physics, and ground states of frustrated amorphous materials. One of the reasons these problems are proving elusive is that calculation of properties of many-body quantum mechanical systems is computationally intensive enough to be completely prohibitive in a large class of problems.

Quantum simulation provides an attractive alternative to direct computation. In it, a test quantum system, here ultracold atoms, is used to simulate a more complicated, less experimentally accessible quantum system, such as a non-trivial material from condensed matter physics. In order to get to the point where unsolved problems can be solved with quantum simulation, tools must be built up to create and verify Hamiltonians in the test system that are relevant to the more complex target system. In this thesis, we present a technique for creating topologically non-trivial Hamiltonians for ultracold atoms and experimentally measuring their topological properties.

1.1 Condensed matter context

Topology has been a field of mathematics since the 17th century. Its importance in physics, particularly in the study of crystalline materials in condensed matter, was first discovered by Thouless, Kohmoto, Nightingale and den Nijs [1].

They used topology to explain the shockingly precise quantization of resistivity in the quantum Hall effect. Since then, topology has been central to condensed matter, from topological insulators [2] to fractional quantum hall physics [3]. There have been many excellent pedagogical texts written on this matter. Here, we include only a brief overview of the physics that is relevant for motivating Chapters ?? of this thesis.

1.1.1 Topology

Topology is the study of how things can be continuously transformed into other things without tearing or gluing parts together. Things that can be continuously transformed into each other under those rules are called homeomorphic to each other. Classes of objects that are all homeomorphic to each other belong to the same topological class. These classes are characterized by a topological invariant, an integer. Surfaces in 3D can be characterized by their genus g , essentially the number of holes in the shape. Since holes cannot be opened up or closed by a continuous transformation, the number of holes is a topological invariant that can be used for classification.

Figure 1.1.1 shows some examples of objects with different genus g . A loaf of bread has no holes, and is therefore topologically equivalent to a sphere, with $g = 0$. A bagel has one hole, and is topologically equivalent to a torus, or a coffee mug, or any other number of things with a single through hole, with $g = 1$. A pretzel has 3 through holes, and is therefore topologically distinct from both the loaf and the bagel, with $g = 3$.

More formally, the Gauss-Bonnet theorem states that the integral of the Gaussian curvature K over a closed surface S is an integer multiple of 2π :

$$\chi = \frac{1}{2\pi} \int_S K dA, \quad (1.1)$$

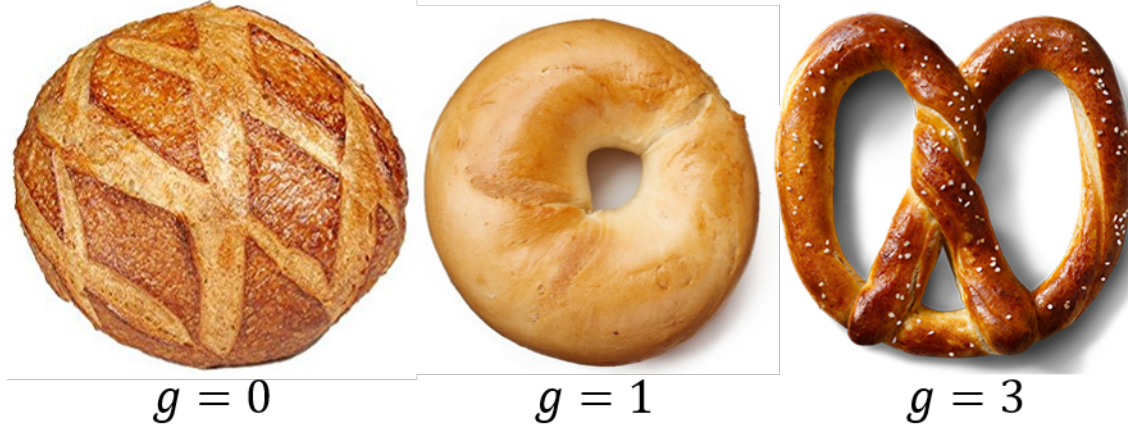


Figure 1: Topology of baked goods. They are classified according to genus g , the number of holes.

where the integer χ is called the Euler characteristic, and is related to the genus via $\chi = 2 - 2g$. Essentially, the total curvature of a closed surface is quantized to integer values, and any closed surface can be classified by that integer. Surfaces with equal χ can be continuously transformed into each other.

1.1.2 Band topology in materials

The same general principles can be applied to the bands within the band structure of a crystalline material. Crystalline materials are characterized by a periodic structure. The primitive unit cell, or the minimal repeating unit of the lattice, can be parametrized by primitive unit vectors \vec{a}_i , where i indexes from 1 to the number of dimensions d . In momentum space, the repeating structure is parametrized by reciprocal lattice vectors \vec{K}_i . According to Bloch's theorem [4], the eigenstate wavefunction for some eigenband in a periodic potential in d dimensions can be written as

$$|\Psi(\vec{k})\rangle = e^{i\vec{k}\cdot\vec{r}} |u(\vec{k})\rangle , \quad (1.2)$$

where \vec{k} is the crystal momentum, \vec{r} is the spatial coordinate, and $|u(\vec{k})\rangle$ is periodic with the reciprocal lattice periodicity. Reciprocal lattice space is well defined for an infinite system, and is a good approximation for a system that is large compared to the primitive lattice size.

There is a phase ambiguity in the definition of the Bloch wavefunction, such that the physics remains invariant under the transformation

$$|u(\vec{k})\rangle \rightarrow e^{i\phi(\vec{k})} |u(\vec{k})\rangle, \quad (1.3)$$

which is reminiscent of gauge invariance in electrostatics. The corresponding non-gauge invariant potential is called the Berry connection \vec{A} , and is given by

$$\vec{A} = -i \langle u(\vec{k}) | \nabla_{\vec{k}} | u(\vec{k}) \rangle. \quad (1.4)$$

Under the transformation eq. 1.3, $\vec{A} \rightarrow \vec{A} + \nabla_{\vec{k}}\phi(\vec{k})$. The gauge invariant field is therefore $\vec{\mathcal{F}} = \nabla \times \vec{A}$, where $\vec{\mathcal{F}}$ is known as the Berry curvature.

From this, the geometric phase, or Berry phase γ_c , can be defined as the phase acquired over a closed curve in parameter space that is independent of the rate at which the curve is traversed:

$$\gamma_c = \int_c \vec{A} \cdot d\vec{k} = \int_S \vec{\mathcal{F}} \cdot dS, \quad (1.5)$$

where S is a surface bounded by the curve c , and in the second equality we have invoked Stoke's theorem.

The Berry curvature integrated over the entire Brillouin zone, or primitive cell in reciprocal lattice space, is quantized in units of 2π :

$$C = \frac{1}{2\pi} \int_S \vec{\mathcal{F}} \cdot dS, \quad (1.6)$$

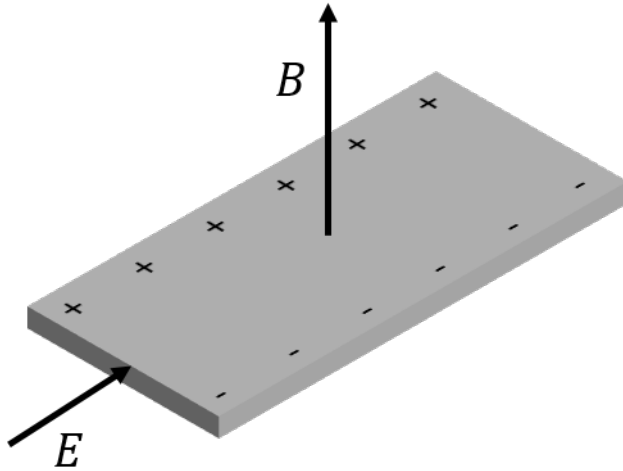


Figure 2:

where C is an integer. This bears a strong similarity to the Gauss-Bonnet theorem, eqn. 1.1, with the Gaussian curvature replaced by the Berry curvature, and the closed surface in real space replaced by the Brillouin zone in momentum space. Similarly, the integer C is a topological invariant and can be used to classify the topological properties of the bands. For periodic structures in 2D, this invariant is called the Chern number.

Integral over the Berry curvature definition in infinite system Bulk-edge correspondence in finite system

1.1.3 Quantum Hall Effect

The iconic example of non-trivial topological structure in condensed matter is the quantum Hall effect. First, let us review the regular Hall effect. In it, a slab of metal, very thin along one dimension such as to be effectively 2D, has a magnetic field threaded through it perpendicular to the plane of the metal, as shown in Figure 1.1.3. Then, a magnetic field is applied along one direction of the 2D material. This accelerates the electrons via the electrostatic force $F = qE$

Quantum Hall Effect (with/without disorder)

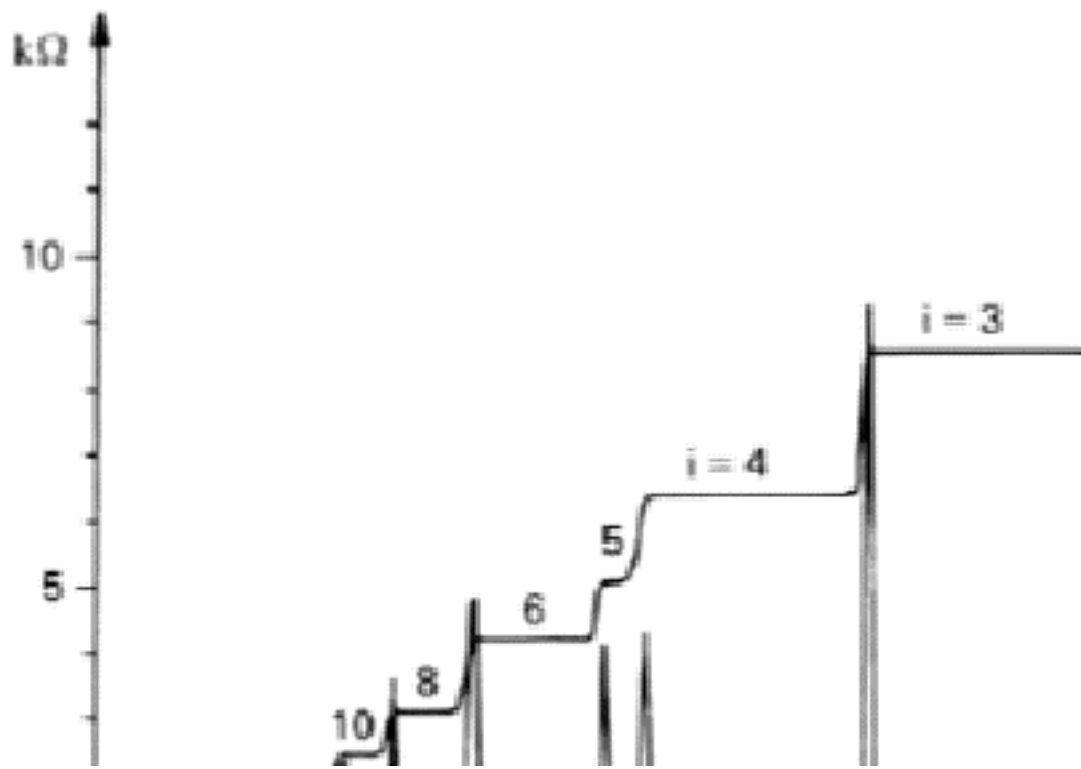


Figure 3:

1.1.4 Hofstadter regime

Aharonov-Bohm effect - phase as magnetic field Hofstadter Butterfly

Diophantine equation Topological insulators

1.2 Ultracold atoms for quantum simulation

They are quantum and well controlled and detected Neutral atoms act as though they're in a magnetic field

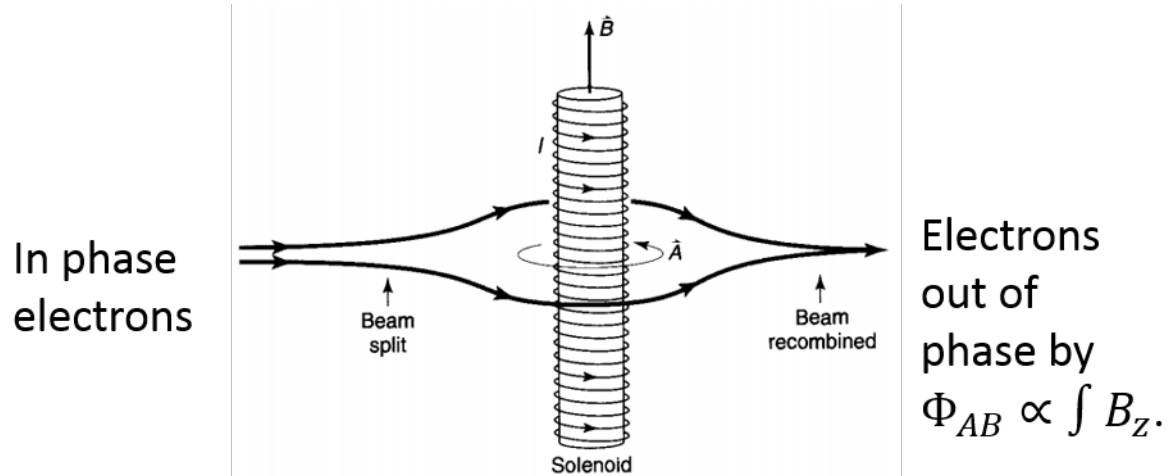


Figure 4:

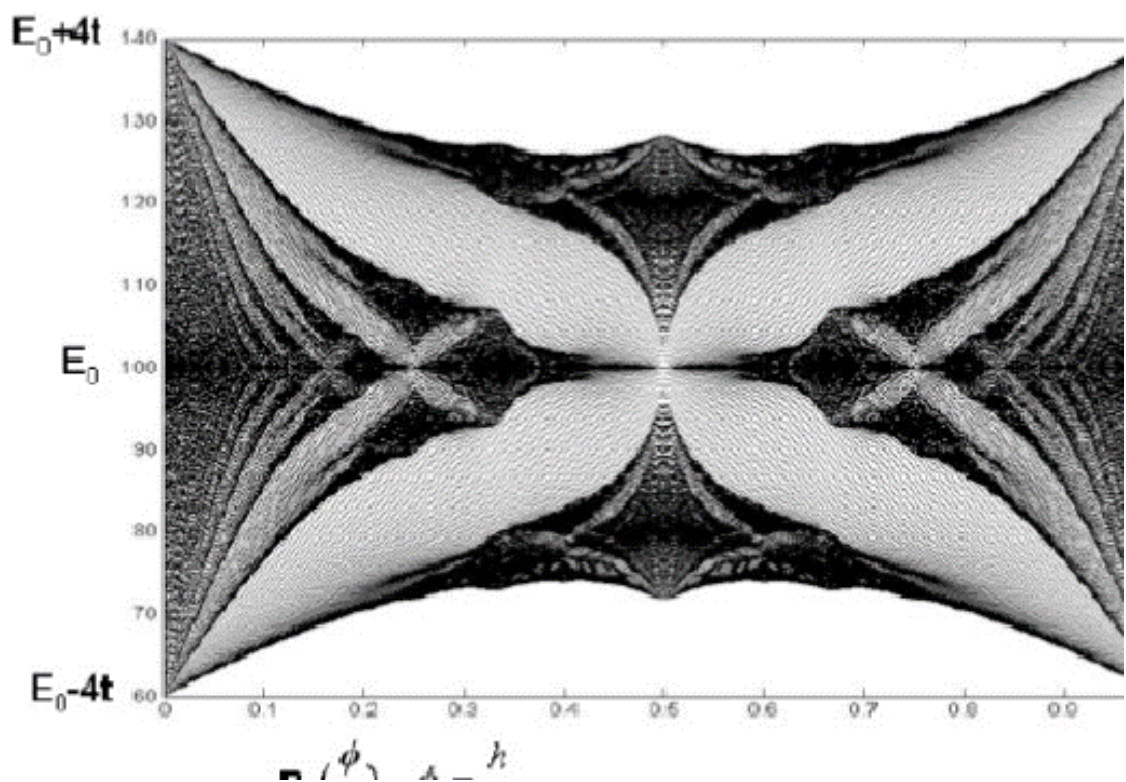


Figure 5:

Chapter 1: Atom Light Interactions

1.1 Atomic structure

Alkali atoms (those in the first column of the periodic table) are the most amenable to laser cooling because their energy level structure is relatively simple. It can be understood as primarily the energy state of the single electron in the outer shell, interacting with the rest of the atom—the nucleus and all the other electrons—as a whole. The quantum numbers that describe the energy levels of the atom are the radial quantum number of the outermost electron N , that electron’s spin S , the orbital angular momentum L , and finally the nuclear spin I . The work described in this thesis was done with alkali species ^{87}Rb and ^{40}K .

1.1.1 Fine and hyperfine structure

The spin orbit interaction, or coupling between L and S , give rise to the fine structure of the atom. This is the splitting of energies according to the quantum number J , where the operator $\mathbf{J} = \mathbf{L} + \mathbf{S}$ and $|L - S| \leq J \leq |L + S|$. The ground state of ^{87}Rb , in term notation $N^{2S+1}L_J$ is $5^2S_{1/2}$, where S is orbital notation indicating $L = 0$. Since $L = 0$, the ground state only has one possible value of $J = 1/2$, and there is no ground state hyperfine splitting. The first excited state 5^2P_J has orbital angular momentum $L = 1$ (as indicated by P in orbital notation). Therefore, J can take on two different values: $1/2$ and $3/2$, producing a hyperfine splitting between the $5^2P_{1/2}$ and $5^2P_{3/2}$. The energy splitting between the ground $5^2S_{1/2}$ and lower

excited $5^2P_{1/2}$ level is conventionally called the $D1$ line, and the splitting between $5^2S_{1/2}$ and $5^2P_{3/2}$ is the $D2$ line. For other alkalis, including ^{40}K , the ground state structure is identical and only the N value is different. Therefore, even though their energies vary, $D1$ and $D2$ lines feature in all alkalis.

There is also a contribution from the nuclear spin \mathbf{I} , which gives rise to hyperfine structure of the states. For ^{87}Rb , $I = 3/2$ and for ^{40}K , $I = 4$. The total spin, including nuclear spin, is indicated by the quantum number F , and $|J - I| \leq F \leq |J + I|$. The interaction with the nuclear spin splits the ground state of ^{87}Rb into two manifolds, $F = 1$ and $F = 2$. Similarly for ^{40}K , it splits the ground state into $F = 9/2$ and $F = 7/2$ manifolds. The structure of the ground and first excited states of ^{87}Rb and ^{40}K , including both the fine and hyperfine splittings, is diagrammed in Figure 1. Note that the $D1$ and $D2$ transitions are in the optical regime, making them amenable to laser cooling. The fine structure splitting of the excited states is in the far infrared, whereas the hyperfine splitting of the ground states is in the microwave regime.

1.1.2 Interaction with static magnetic fields

In a static background magnetic field \mathbf{B} , the atomic angular momentum interacts with the field via the Hamiltonian

$$H_B = \frac{\mu_B}{\hbar} (g_S \mathbf{S} + g_L \mathbf{L} + g_I \mathbf{I}) \cdot \mathbf{B}, \quad (1.1)$$

where μ_B is the Bohr magneton, g_S , g_L and g_I are the spin, orbital and nuclear Lande g-factors correcting their respective magnetic dipole moments. Without loss of generality, we can define the magnetic field to be in the e_z direction, $\mathbf{B} = B_z e_z$, to obtain

$$H_B = \frac{\mu_B}{\hbar} (g_S S_z + g_L L_z + g_I I_z) B_z. \quad (1.2)$$

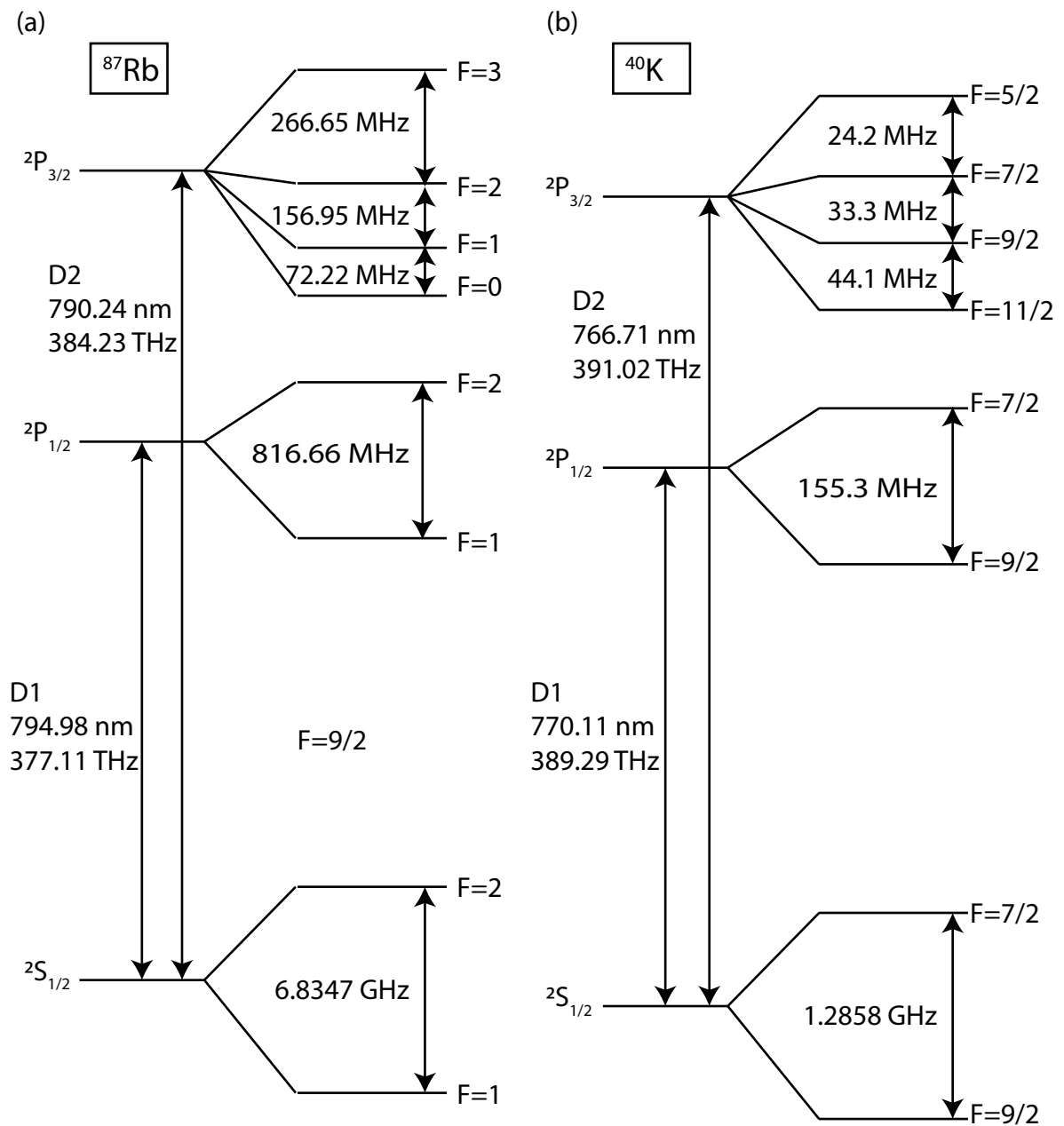


Figure 1: Atomic structure of the ground and first excites states, with fine and hyperfine splittings. (a) ^{87}Rb . Values from [5]. (b). ^{40}K . Values from [6].

At very low magnetic field strengths, where the energy shift due to H_B is small compared to the hyperfine splitting, the total angular momentum F remains a good quantum number, and the Hamiltonian in eqn. 1.3 can be re-written as

$$H_B = \frac{\mu_B}{\hbar} (g_F F_z) B_z, \quad (1.3)$$

where the effective Lande g-factor is dependent on the angular momentum quantum numbers:

$$g_F = g_J \frac{F(F+1) - I(I+1) + J(J+1)}{2F(F+1)} + g_I \frac{F(F+1) + I(I+1) - J(J+1)}{2F(F+1)}. \quad (1.4)$$

In this regime, the levels split linearly according to the F_z projection quantum number, m_F . For the ground state of ^{87}Rb , it splits into three hyperfine states in the $F = 1$ manifold ($m_F = 0, \pm 1$) and five hyperfine states in the $F = 2$ manifold ($m_F = 0, \pm 1, \pm 2$). This regime is at fields $B \leq \approx 1$ Gauss for ^{87}Rb , as seen in Figure 2.

At fields producing energy shifts small compared to the fine structure splitting, but not negligible compared to the hyperfine splitting, F is no longer a good quantum number, and the relevant Hamiltonian becomes

$$H_B = \frac{\mu_B}{\hbar} (g_J J_z + g_I I_z) B_z. \quad (1.5)$$

Here, since $g_I \ll g_J$, the energy dependence on B_z is dominated by a linear dependence on the J_z projection quantum number, m_J , as seen in the higher field limit in Figure 2.

In the intermediate regime, there is in general no analytic solution for the eigenenergies and one must resort to numerics. However, for the specific case of $J = 1/2$ applicable to alkali ground states, there is an analytic solution given by the

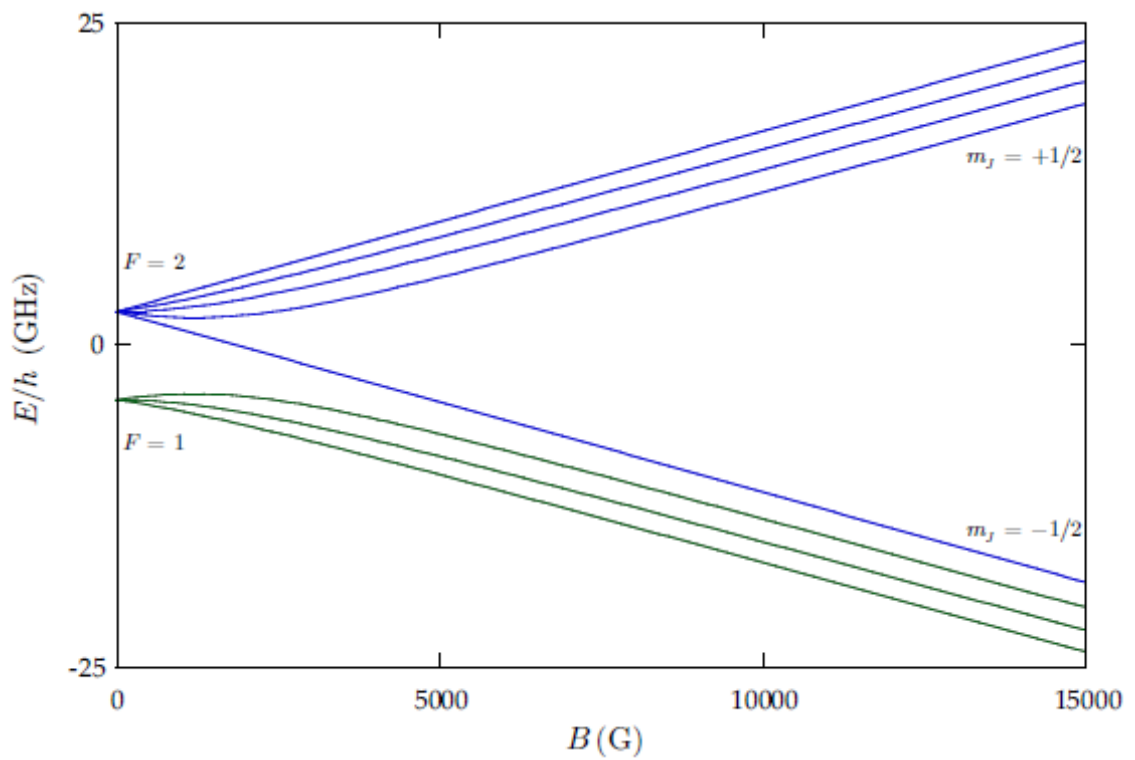


Figure 2: Energy structure of hyperfine states of the ground state of ^{87}Rb as a function of external magnetic field strength in Gauss. Figure from ref. [5]

Breit-Rabi formula [7]:

$$E_{|J=1/2m_JIm_I\rangle} = -\frac{\Delta E_{hfs}}{2(2I+1)} + g_I \mu_B m B \pm \frac{\Delta E_{hfs}}{2} \left(1 + \frac{4mx}{2I+1} + x^2\right)^{1/2}, \quad (1.6)$$

where ΔE_{hfs} is the zero field hyperfine splitting, $m = m_I \pm m_J$, and

$$x = \frac{(g_J - g_I)\mu_B B}{\Delta E_{hfs}}. \quad (1.7)$$

From this we can get a better picture of the shifts at low fields, where $\mu_B B \ll E_{hfs}$.

Expanding eqn. 1.6 to second order in small parameter $4mx/(2I+1) + x^2$, and neglecting the field-independent terms, we obtain

$$\Delta E_{|J=1/2m_JIm_I\rangle} \approx \frac{\Delta E_{hfs}}{2} \left(\frac{1}{2} \left[\frac{4mx}{2I+1} + x^2 \right] - \frac{1}{8} \left[\frac{16m^2x^2}{(2I+1)^2} + \frac{4mx^3}{2I+1} + x^4 \right] \right). \quad (1.8)$$

We recognize the term linear in mx , $E_{hfs}mx/(2I+1) = (g_J - g_I)\mu_B B m / (2I+1)$.

In addition, there is a term quadratic in mx :

$$\Delta E_{hfs} \frac{m^2 x^2}{2I+1} = \frac{(g_J - g_I)^2 \mu_B^2 B^2 m^2}{\Delta E_{hfs} (2I+1)^2} = \epsilon(B) m^2, \quad (1.9)$$

where in the last term we have defined $\epsilon(B)$, the magnitude of this 'quadratic' Zeeman energy shift. For the magnetic field strengths used in experiments described in this thesis, the linear term plus quadratic correction are sufficient for describing the energy levels.

The form of the approximate Hamiltonian in this regime for any value of F is given by

$$H_0 = H_{\text{KE}} + \hbar\omega_z \mathbf{F}_z + \hbar\epsilon \mathbf{F}_z^2, \quad (1.10)$$

where $\hbar\omega_z = \mu_B g_F B_z / \hbar$, and the kinetic energy Hamiltonian $H_{\text{KE}} = \hbar^2 \vec{k}^2 / 2m\mathcal{I}$, and \mathcal{I} is the identity matrix.

1.2 Near-resonant atom-light interaction

In this section, we will assume the atom can be treated as a two-level system: one with a ground and excited atomic state, with an energy difference of energy difference $\hbar\omega_0$. When such an atom, starting in the ground state, is illuminated by a laser beam with frequency $\hbar\omega_L$, there are three kinds of transitions that occur: during absorption the atom absorbs a photon from the laser and goes from the ground to the excited state; during stimulated emission, the atom emits a photon into the field of the laser beam and jump from the excited to the ground state; during spontaneous emission, the atom decays to the ground state from the excited state with no help from the laser, emitting into a random vacuum mode. Stimulated emission results in coherent light co-propagating with the laser beam, while spontaneous emission results in light scattering incoherently in any direction. The rate of spontaneous emission from an excited state is given by the natural transition linewidth of the atomic transition Γ .

1.2.1 Rabi oscillations

On timescales short compared to $1/\Gamma$, spontaneous emission can be ignored, and an atom undergoes coherent Rabi oscillations between the ground and excited states via cycles of absorption and stimulated emission [8]. Let us consider the Hamiltonian

$$H = H_0 + H_L(t), \quad (1.11)$$

where H_0 is the bare atomic Hamiltonian and H_L is the interaction with the laser beam. We can write the wavefunction Ψ as a linear combination of the two eigenstates (for a two-level atom) of the bare Hamiltonian as

$$\Psi = c_g(t)\phi_g(\mathbf{r})e^{-i\omega_g t} + c_e(t)\phi_e(\mathbf{r})e^{-i\omega_e t}, \quad (1.12)$$

where $c_g(t)$ and $c_e(t)$ are the time-dependent coefficients multiplying the eigenstate wavefunctions ϕ_g and ϕ_e of the ground and excited state respectively, and \mathbf{r} is the spatial coordinate. Absorbing any diagonal elements of H_L into H_0 , multiplying both sides of the Schroedinger equation from the left by ψ_j and integrating over \mathbf{r} , we can write down the Schroedinger equation as two coupled equations:

$$i\hbar \frac{dc_g(t)}{dt} = c_e(t)H_L^{ge}(t)e^{-i\omega_0 t} \quad (1.13)$$

and

$$i\hbar \frac{dc_e(t)}{dt} = c_g(t)H_L^{eg}(t)e^{i\omega_0 t}, \quad (1.14)$$

where $H_L^{ge}(t)$ is the off-diagonal element of the laser coupling Hamiltonian that couples the excited to the ground state and $H_L^{ge}(t) = H_L^{eg*}(t)$. This coupling Hamiltonian can be written in terms of the electric field produced by the laser beam coupling to the electric dipole moment of the atom as

$$H_L^{ge}(t) = \hbar\Omega\cos(kz - \omega_L t) \quad (1.15)$$

with

$$\Omega = \frac{-eE}{\hbar} \int \phi_g(\mathbf{r})\mathbf{r}\phi_e(\mathbf{r})dr \quad (1.16)$$

the Rabi frequency, characterizing the coupling strength between the laser field (with amplitude E) and the atom. Here, e is the charge of the electron. The Rabi frequency can also be related to the natural linewidth of the atomic transition Γ via $\Omega^2 = \frac{\Gamma\lambda_L^3}{h(2\pi)^3}I$, with λ_L as the laser wavelength, h as Plank's constant and I as the laser intensity.

To solve this Schroedinger equation, we make the traditional transformation

to the rotating frame:

$$c'_g(t) = c_g(t) \quad (1.17)$$

$$c'_e(t) = c_e(t)e^{-i\delta t}, \quad (1.18)$$

where $\delta = \omega_0 - \omega_L$ is the detuning of laser light from resonance. In this frame, we can write the atom-light Hamiltonian in the $\begin{pmatrix} c'_g \\ c'_e \end{pmatrix}$ basis as:

$$H = \hbar \begin{pmatrix} -\delta/2 & \Omega/2 \\ \Omega/2 & \delta/2 \end{pmatrix}. \quad (1.19)$$

In the limit of no coupling, $\Omega = 0$, in the rotating frame the eigenenergies are $E_{\pm} = \pm \hbar\delta/2$. For non-zero coupling, finding the eigenvalues of H gives

$$E_{\pm} = \pm \hbar\sqrt{\delta^2 + \Omega^2}/2. \quad (1.20)$$

The eigenenergies are shifted in the presence of the light.

Assuming the atom starts in the ground state $c_g(t=0) = 1$, we can solve the Schrödinger equation with the above Hamiltonian

$$i\hbar \frac{d}{dt} \begin{pmatrix} c'_g \\ c'_e \end{pmatrix} = H \begin{pmatrix} c'_g \\ c'_e \end{pmatrix} \quad (1.21)$$

we obtain the oscillating excited state population

$$c'_e(t) = -i \frac{\Omega}{\sqrt{\Omega^2 + \delta^2}} \sin \left(\frac{\sqrt{\Omega^2 + \delta^2}t}{2} \right), \quad (1.22)$$

known as Rabi oscillations. The frequency of these oscillations is the generalized

Rabi frequency $\Omega' = \sqrt{\Omega^2 + \delta^2}$. The amplitude of the oscillation is maximum when the laser is on-resonance, $\delta = 0$. As the detuning increases, the contrast in excited and ground populations decreases, while the frequency of the oscillation increases.

1.2.2 Scattering

In the regime where spontaneous emission cannot be ignored, Rabi oscillations of each individual atom are intermittently interrupted by decay to the ground state. Averaging over an atomic ensemble, on the time scale of a single Rabi oscillation the overall excited state population reaches a steady state, and the rate of spontaneous emission becomes constant. Since during spontaneous emission the ejected photon can go into any vacuum mode, this process can be thought of as the scattering of photons by the atoms. This scattering rate is given by [8]

$$\gamma_{\text{sc}} = \frac{\Gamma}{2} \frac{I/I_{\text{sat}}}{1 + 4(\delta/\Gamma)^2 + I/I_{\text{sat}}}, \quad (1.23)$$

where I_{sat} is the saturation intensity. This is the intensity at which the timescale of spontaneous emission matches the Rabi oscillation rate, reducing the capacity for absorption of extra light.

1.2.3 Adiabatic rapid passage

Suppose there is a two-level atom in its ground state that an experimentalist wants to transfer into the excited state. To transfer it with perfect fidelity using Rabi oscillations, one would need a perfectly on-resonant beam and very precise timing to shut off the coupling field at the maximum of the excited state population. This is challenging and not very stable to small perturbations in background field. A more robust technique is known as adiabatic rapid passage.

Suppose the two energy levels of the atom are sensitive to some external pa-

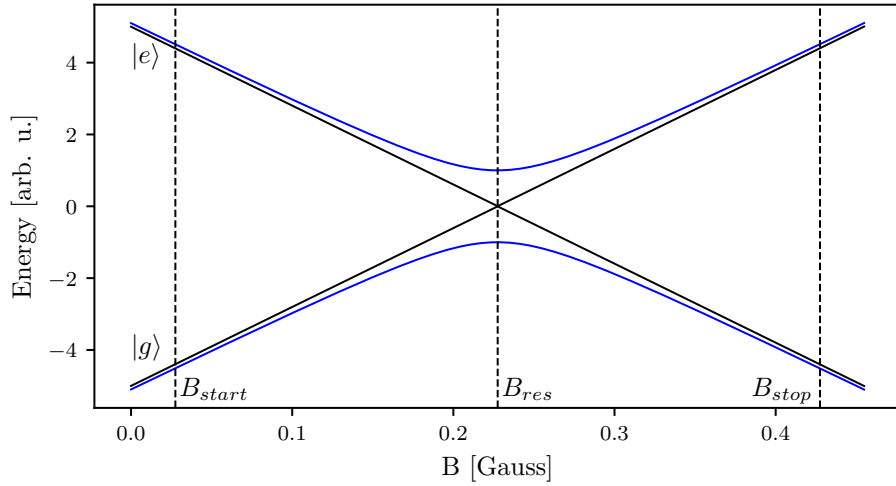


Figure 3: Adiabatic rapid passage (ARP). Black lines represent energies of the ground and excited state, in the rotating frame, with zero coupling. Blue line represent these bands with rf coupling turned on. The dashed lines represent the starting point of an ARP (B_{start}), the resonant field value (B_{res}) and the end point of an ARP (B_{stop}).

parameter. Commonly (as in the case with hyperfine sublevels), they are sensitive to an external magnetic field B , and in the small field limit are linear in B . Therefore, the detuning that goes into the Hamiltonian in eqn. 1.19 becomes $\hbar\delta = A*B - \hbar\omega_L$, where A is the coupling constant in the hyperfine (or other) Hamiltonian. In the limit of zero coupling strength, diagonalizing the Hamiltonian amounts to calculating the eigenenergies in the rotating frame as a function of the control parameter B . These are represented in black in figure 3. Note that the two levels cross each other when their energy difference matches $\hbar\omega_L$, on resonance.

Once the coupling field is turned on (in the case of the hyperfine interaction, and rf-field), the two levels split near the resonance and an avoided crossing appears, as seen in blue in Figure 3. Crucially, away from resonance towards the left, the bottom coupled state overlaps closely with the uncoupled (black state). Far from resonance, the ground state is largely unaffected by the presence of light. On the other hand, far from the resonance on the right, the lower coupled state overlaps

almost perfectly with the excited uncoupled state. Adiabatic rapid passage (ARP) takes advantage of this change.

The ARP protocol is as follows. Start at bias field (or other control parameter) where turning on the coupling field does not significantly perturb the eigenstate (B_{start} in the figure). Turn on the coupling field adiabatically (slow with respect to the time scale associated with the level splitting energy $\tau = h/(E_e - E_g)$), such that the atom remains entirely in the ground state $|g\rangle$. Then, sweep the control parameter across the resonance, again adiabatically with respect to the coupled level splitting (blue in the figure). The sweep rate can be optimized to be faster away from resonance, where $E_e - E_g$ is large and slower closer to the avoided crossing. Then, at a final value of the control parameter where the lowest coupled state overlaps almost perfectly with the bare excited state $|e\rangle$, adiabatically turn off the coupling field, leaving the atoms in the excited state.

The 'rapid' part of adiabatic rapid passage refers to the procedure having to be fast with respect to the spontaneous emission timescale, since in the coupled basis there is some population in the excited state and spontaneous decay would disrupt the process. This procedure is relatively insensitive to field fluctuations (as long as B_{res} is roughly in the middle of the relatively long sweep, the procedure will succeed). It can also be applied to multi-level situations, where the atoms traverse multiple avoided crossings in the same sweep and can be efficiently transferred from one stretch state $m_F = F$ to the other $m_F = -F$, or vice versa.

1.3 Far-off resonant atom-light interaction

We can infer the behavior of atoms in a far-detuned laser field by taking the near resonant solutions from eqns. 1.20 and 1.22 in the limit $\delta \gg \Omega$. First, looking at the excited state population in eqn. 1.22, the amplitude of the excited state population oscillation approaches zero. Therefore, as expected, no absorption of the

light actually takes place and the atom remains in the ground state. However, the light still effects the atom by shifting the eigenenergies via eqn. 1.20. Recalling that the bare eigenenergies in the rotating frame are given by $E_{\pm} = \pm\hbar\delta/2$, the energy shift from bare is given by

$$\Delta E_{\pm} = \pm\hbar\sqrt{\delta^2 + \Omega^2}/2 - \pm\hbar\delta/2 \quad (1.24)$$

Expanding the energy shift in the small parameter Ω/δ , we obtain the shifted energies $E_{\pm} = \pm\hbar\sqrt{\delta^2 + \Omega^2}/2 \approx \pm(\delta/2 + \Omega^2/4\delta)$. The shift from bare energy levels is thus

$$\Delta E_{\pm} \approx \pm\hbar(\delta/2 + \Omega^2/4\delta) - \pm\hbar\delta/2 = \pm\hbar\Omega^2/4\delta. \quad (1.25)$$

This laser intensity dependent energy shift is called the AC Stark shift, and is the basis of most laser created potentials for cold atoms.

For the ground state, and a red detuned laser beam (where the laser frequency is lower than the resonant frequency), this creates energy minima in locations of maximal laser intensity. For the lattice described in this chapter, as well as for the trapping of our atoms in the final stages of cooling, we use high power (up to 10 W) lasers with wavelength $\lambda_L = 1064$ nm.

1.4 Absorption imaging

Absorption imaging takes advantage of the on-resonant interaction described in the previous section. An on or near-resonant laser beam ($\delta/\Gamma \ll 1$) is shined at the atoms, and the aborbed light acts to create a shadow in the shape of the atoms in the laser beam. This beam with the shadow is then imaged on a camera, in our case a CCD, as depicted in Figure 4a (top). This is called the atom image, and the intensity distribution over the camera is denoted by $I_f(x, y)$, where the subscript f stands for final - the intensity after the light has encountered the atoms.

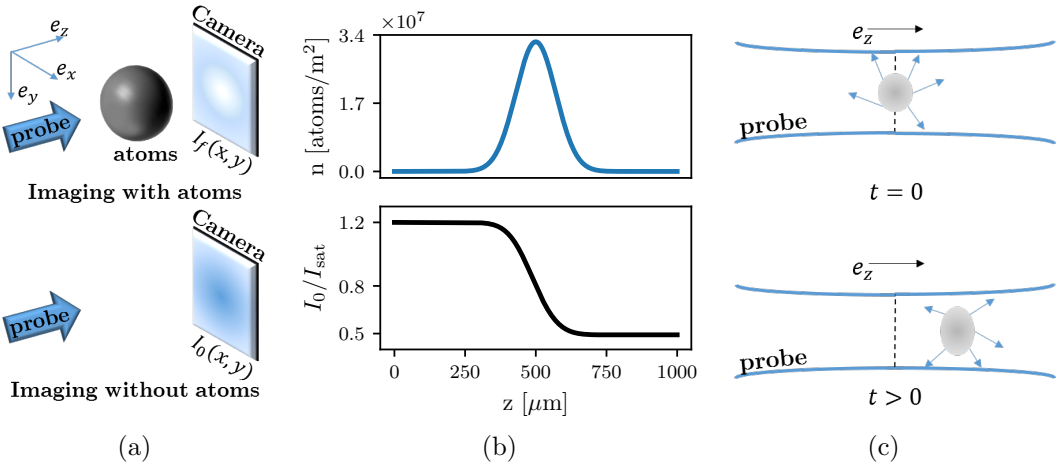


Figure 4: Absorption imaging. (a) Near resonant probe light illuminates the atoms, and the transmitted light (containing a shadow of the atoms) is imaged on the camera. A second image taken with no atoms provides a reference. (b) The probe beam is partially absorbed as it traverses the cloud, and the intensity seen by atoms further along the imaging direction e_z is lowered. (c) An atomic cloud illuminated by a probe light field absorbs photons from the probe and re-emits them in all directions. This process results in a net acceleration of the cloud in the direction of the probe light as well as diffusive spreading in the transverse directions.

To quantify the 'shadowed out' intensity, after the atoms have left the trap the same laser intensity is shined directly at the camera, as in Figure 4a (bottom). This is called the probe image, and the intensity distribution over the camera is denoted by $I_0(x, y)$, where the subscript 0 indicated initial - the intensity before the light had encountered the atoms.

To recover the atom number distribution encountered by the light, consider an atomic cloud with 3D density $\rho(x, y, z)$. Since we can only obtain 2D information from the camera, we can only hope to recover a 2D atomic column density $n(x, y) = \int \rho(x, y, z) dz$. Focusing in on a single pixel of the camera, we can consider a single value of I_0 and I_f to recover a local n . As the laser light propagates through the atomic cloud, the intensity of the light will diminish due to absorption. This absorption as a function of propagation direction z can be expressed using the scattering rate equation Eq. 1.23 as the number of photons scattered by the atoms

(proportional to the atomic density times the scattering rate) times the photon energy $\hbar\omega_L$:

$$\frac{d}{dz} \frac{I(z)}{I_{\text{sat}}} = -\hbar\omega_L \rho(z) \gamma_{sc}(z) = -\rho(z) \sigma_0 \frac{I(z)/I_{\text{sat}}}{1 + 4\delta^2/\Gamma^2 + I(z)/I_{\text{sat}}}, \quad (1.26)$$

where the resonant scattering cross section is $\sigma_0 = 3\lambda_0^2/2\pi$, and λ_0 is the wavelength associated with atomic resonance.

Integrating both sides of Eq. 1.26, we obtain

$$\sigma_0 n = (1 + 4\delta^2/\Gamma^2) \ln(I_0/I_f) + (I_0 - I_f)/I_{\text{sat}}. \quad (1.27)$$

The quantity $OD = \ln(I_0/I_f)$ is called the optical depth of the cloud. When the probe intensity I_0 is much smaller than the saturation intensity, the second term in Eq. 1.27 becomes negligible. Assuming further that the probe light is on resonance, $\delta = 0$, the atomic column density becomes simply $\sigma_0 n = OD$. Figure 4b shows a Gaussian atomic density distribution (top) and the resulting probe intensity as a function of position in the cloud (bottom). The intensity drops from its initial to final value gradually as it traverses the cloud.

However, there is an important effect that the above equations do not account for. Namely, as the atoms absorb light from the probe beam, they also get a momentum kick equal to the momentum of a photon during each collision $\hbar k_r = h/\lambda_L$ in the direction of propagation. It is true that the absorbed photon will then be re-emitted by the atom, inducing a loss of momentum, but since this happens through the process of spontaneous emission into a random vacuum mode, the average momentum kick acquired this way over many re-emissions will average to zero. On average, each photon absorbed will induce a change in velocity of the atom of $v_r = \hbar k_r/m$, where m is the atomic mass, as depicted in Fig. 4c. As the velocity of the atom changes, due to the Doppler effect, the apparent laser frequency will change as well.

Therefore, even if the laser light is exactly on-resonant for a stationary atom, it will become off-resonant for longer imaging times, and Eq. 1.26 will acquire a time dependence. For most experiments, this effect is small and can be neglected. However, if the imaging time becomes of order a recoil time t_r , a time after which the recoil-induced detuning δ becomes of order Γ , this effect becomes significant. We explore this effect in Chapter 3.

1.4.1 Time-of-flight and in situ imaging

There are two commonly used protocols for measuring cold atomic clouds, in situ and time of flight measurements. Generally, the atomic cloud is trapped (in our case by an optical dipole trap) during the experiment. In situ is Latin for in its original place. As suggested by the name, in situ measurements are taken while the cloud is still in its original trap, or immediately after the trap is turned off before any dynamics have had time to occur. These measurements measure the real spatial distribution of the atoms at the end of the given experiment. There is a difficulty associated with making in situ measurements of BECs, however. Namely, BECs in their original trap tend to be relatively dense, with optical depths often in excess of $OD \approx 20$, requiring unrealistic probe light intensities to resolve. One way to bypass this difficulty is to selectively image only a small fraction of the condensed atoms, as was done with microwave imaging for our magnetic field stabilization feedforward protocol [INSERT SECTION REFERENCE HERE ONCE ITS WRITTEN]. Another option is to instead perform a time-of-flight measurement.

In time-of-flight measurements, the trapping potential is abruptly snapped off after the experiment, and the atoms are allowed to free fall and expand for some time t . For our experiments, t was on the order of tens of milliseconds. In the regime where time t is long enough that the atoms travel much further than the initial extent of the cloud in the directions transverse to the imaging axis, the final

position of the atoms is determined almost exclusively by their in situ momentum, not their in situ position. Therefore, time-of-flight imaging in this regime measures the atomic distribution as a function of momentum, not position.

1.5 One dimensional optical lattices

1.5.1 Lattice Hamiltonian

Our 1-D optical lattice is created by retro-reflecting the $\lambda_L = 1064$ nm laser, creating a standing wave of light. Via the AC Stark shift, this creates a periodic potential for the atoms of the form

$$V = V_0 \sin^2(k_L x), \quad (1.28)$$

where $k_L = 2\pi/\lambda_L$ is the wavenumber associated with the lattice recoil momentum. The time-independent Hamiltonian, for some eigenenergy E_n , will be given by

$$-\frac{\hbar^2}{2m} \frac{d^2}{dx^2} \Psi_n(x) + V_0 \sin^2(k_L x) \Psi_n(x) = E_n \Psi_n(x). \quad (1.29)$$

Since the potential is spatially periodic, we can invoke Bloch's theorem [4]:

$$\Psi_{n,q} = e^{iqx} u_{n,q}(x), \quad (1.30)$$

where q is the crystal momentum restricted to $\pm\hbar k_L$, and $u_{n,q}(x)$ is the spatially varying part of the wavefunction. Plugging this in to the Hamiltonian, we obtain

$$-\frac{\hbar^2}{2m} \left(-q^2 + 2iq \frac{d}{dx} + \frac{d^2}{dx^2} \right) u_{n,q}(x) + V_0 \sin^2(k_L x) u_{n,q}(x) = E_n u_{n,q}(x). \quad (1.31)$$

Expanding $u_{n,q}(x)$ in Fourier components commensurate with the lattice period of $2k_L$ as $u_{n,q}(x) = \sum_{j=-\infty}^{\infty} a_j e^{i2k_L j x}$, we obtain

$$\sum_j \left(\frac{\hbar^2}{2m} (q + 2k_L)^2 a_j + V_0 \sin^2(k_L x) a_j \right) e^{i2k_L j x} = E_n \sum_j a_j e^{i2k_L j x}. \quad (1.32)$$

Re-writing $\sin^2(k_L x) = (e^{-2ik_L x} + e^{2ik_L x} - 2)/4$, multiplying both sides by $e^{i2k_L j' x}$ and invoking $\sum c_j e^{ik(j-j')} = \delta_{jj'}$, where $\delta_{jj'}$ is the Kroniker delta and c_j are appropriately normalized coefficients, we get for any value of the index j

$$\frac{\hbar^2}{2m} (q + 2k_L j)^2 a_j - \frac{V_0}{4} (a_{j+1} + a_{j-1}) = E_n a_j. \quad (1.33)$$

This can be expressed in matrix form

$$H_L = \begin{pmatrix} \ddots & & & & & \\ & \frac{\hbar^2}{2m} (q + 4k_L)^2 & \frac{V_0}{4} & 0 & 0 & 0 \\ & \frac{V_0}{4} & \frac{\hbar^2}{2m} (q + 2k_L)^2 & \frac{V_0}{4} & 0 & 0 \\ & 0 & \frac{V_0}{4} & \frac{\hbar^2}{2m} q^2 & \frac{V_0}{4} & 0 \\ & 0 & 0 & \frac{V_0}{4} & \frac{\hbar^2}{2m} (q - 2k_L)^2 & \frac{V_0}{4} \\ & & 0 & 0 & \frac{V_0}{4} & \frac{\hbar^2}{2m} (q - 4k_L)^2 \\ & & & & & \ddots \end{pmatrix}, \quad (1.34)$$

in the basis of momentum orders $|k\rangle = e^{ikx}$ given by:

$$\begin{pmatrix} \vdots \\ |q + 4k_L\rangle \\ |q + 2k_L\rangle \\ |q\rangle \\ |q - 2k_L\rangle \\ |q - 4k_L\rangle \\ \vdots \end{pmatrix}. \quad (1.35)$$

This matrix can be diagonalized for every value of the crystal momentum q , with the resulting band structure shown in Figure 5. It is convenient to define the lattice recoil energy $E_L = \hbar^2 k_L^2 / 2m$. Then, we can re-write the Hamiltonian with V_0 in units of E_L and momenta q in units of k_L as

$$H_L/E_L = \begin{pmatrix} \ddots & & & & & \\ & (q+4)^2 & \frac{V_0}{4} & 0 & 0 & 0 \\ & \frac{V_0}{4} & (q+2)^2 & \frac{V_0}{4} & 0 & 0 \\ & 0 & \frac{V_0}{4} & q^2 & \frac{V_0}{4} & 0 \\ & 0 & 0 & \frac{V_0}{4} & (q-2)^2 & \frac{V_0}{4} \\ & 0 & 0 & \frac{V_0}{4} & (q-4)^2 & \ddots \end{pmatrix}. \quad (1.36)$$

In any numerical simulation, the number of momentum orders that can be included is finite. We determine the value of the parameter $n = \max(|j|)$ as the lowest n at which the eigenvalues stop changing to machine precision from $n-1$. The code for finding and plotting the eigenvalues and eigenvectors of the lattice hamiltonian is included in Appendix [MAKE APPENDIX WITH CODE?].

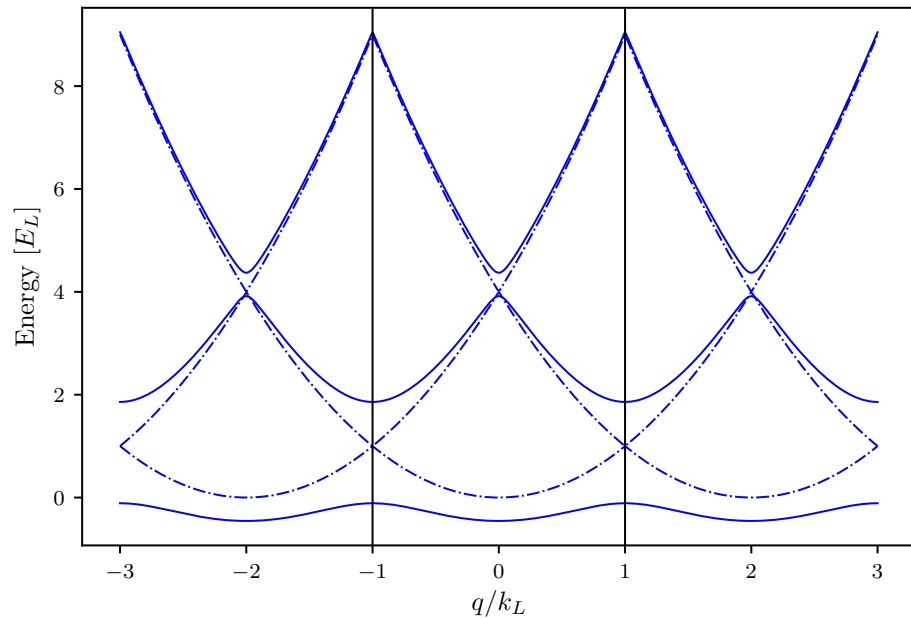


Figure 5: Lattice band structure in the extended zone scheme. The dashed lines represent the limit of zero lattice depth, with the regular parabolic dispersion relation of a free particle repeating with reciprocal lattice period. The solid lines are the dispersion relation at $V_0 = 4.0E_L$, showing the opening of gaps at crossings of the zero lattice depth bands. The black lines demarcate the first Brillouin zone.

1.5.2 Tight binding approximation

In the limit of large lattice depths, $V_0 > \approx 5E_L$, the lattice Hamiltonian is well approximated by the tight-binding model. In the tight binding model, the basis is assumed to be a set of orthogonal functions, called Wannier functions, localized to each lattice site $|j\rangle$. The approximation lies in assuming only nearest neighbor tunnelings between the sites, forming the tight-binding Hamiltonian

$$H_{\text{tb}} = -t |j\rangle \langle j+1| + \text{H.c.}, \quad (1.37)$$

where t is the tunneling amplitude between nearest neighbor sites and H.c. stands for Hermitian conjugate. We have neglected the diagonal kinetic energy term, as it will be equal for every Wannier function $|j\rangle$ and thus represents a constant energy offset. All the information about the lattice depth is therefore reflected in the tunneling amplitude t .

The tight binding Hamiltonian can also be expressed in the momentum basis by Fourier transforming the basis functions:

$$|j\rangle = \frac{1}{\sqrt{N}} \sum_{k_j} e^{-ik_j j} |k_j\rangle, \quad (1.38)$$

giving the Hamiltonian

$$H_{\text{tb}} = -\frac{1}{N} \sum_{k_1} \sum_{k_2} k_2 t e^{-ijk_1} e^{ik_2(j+1)} |k_1\rangle \langle k_2| + \text{H.c.} = 2t \cos(k) |k\rangle \langle k|. \quad (1.39)$$

From this we can directly read off the band structure of the tight binding Hamiltonian. First, we notice that we only obtain one band - to approximate higher bands with the tight binding approximation we would need to construct a different set of Wannier functions and a different tunneling strength. Second, we see that the lowest

band is simply a cosine - therefore we have solved for the band structure without even defining what the basis Wannier functions are! Third, the amplitude of the cosine function is given by the tunneling strength t . This gives us a good clue as to how to determine the appropriate tunneling given a lattice depth V_0 - simply find a t that matches the amplitude of the lowest band, which becomes cosinusoidal in the deep lattice limit.

The precise form of the Wannier functions depends on both the depth of the lattice and the band being reproduced. It is not necessary for us to find their full expression, as the band structure can be calculated without them. The definition, however, is

$$|j\rangle = \int_{\text{BZ}} e^{i\phi(q) - iqja} \Psi_q(x) dq, \quad (1.40)$$

where the integral is over the Brillouin zone, from $-k_L$ to k_L , a is the lattice spacing $\lambda_L/2$, and Ψ_q is the Bloch wavefunction at crystal momentum q , and $\phi(q)$ is the phase associated with each Bloch wavefunction. The Bloch wavefunctions individually have arbitrary phase. The phase plays an important role in combining the Bloch wavefunctions into a Wannier function, finding the proper phase relationship to make the wavefunction maximally localized at each site [9].

1.5.3 Pulsing vs adiabatic loading of the lattice

The lattice depth parameter $V_0/4$, for a range of values, can be well calibrated experimentally by pulsing on the lattice. Here, the word pulsing indicates that the lattice is turned on fully non-adiabatically, if not instantaneously, such that the original bare momentum state is projected onto the lattice eigenbasis, as shown in Figure 8a. If the atoms start out stationary in the trap, the bare state in the

momentum basis is simply

$$|\Psi_0\rangle = \begin{pmatrix} \vdots \\ 0 \\ 0 \\ 1 \\ 0 \\ 0 \\ \vdots \end{pmatrix}, \quad (1.41)$$

as depicted in Figure 8b.

Since the lattice eigenbasis is distinct from the bare one, instantaneously turning on the lattice will necessarily excite the atoms into a superposition of lattice eigenstates, each evolving with a different phase according to the eigenenergy while the lattice is on, as shown in Figure 8c. Then, when the lattice is snapped back off, the wavefunction is projected back into the bare basis, and the varying phase accumulation results in a beating of the different momentum orders, see Figure 8d. This can be calculated simply by using the time evolution operator

$$|\Psi(t)\rangle = e^{-iH_L t/\hbar} |\Psi_0\rangle. \quad (1.42)$$

By pulsing on the lattice for variable amounts of time t , we can obtain fractional populations in the different momentum states. Time-of-flight imaging captures the momentum distribution of the cloud, and the different entries of $\Psi(t)$ in the momentum basis will thus appear as different clouds on the absorption image, as shown in Figure 7a. The fractional population in these clouds corresponds to a measurement of $|a_j|^2$. Typically for our values of the lattice depth $V_0 < 10E_L$, it is sufficient to simply count three central momentum orders, $k = q, q \pm 2k_L$. Then, we can fit Eq. 1.42 to the data with fitting parameter V_0 , thus deducing the lattice depth. Some

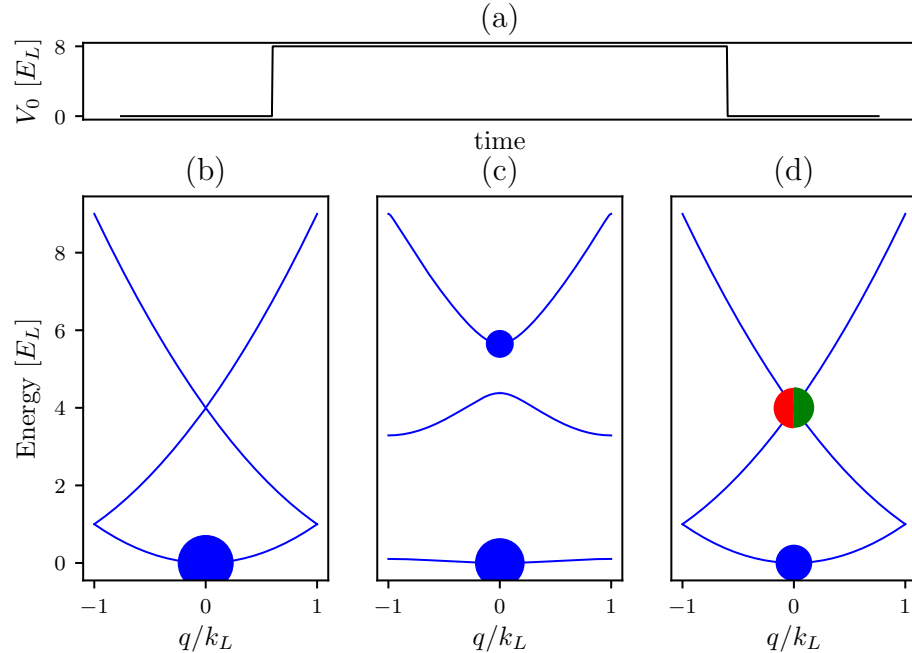


Figure 6: Lattice pulsing. (a) Lattice depth as a function of time during a pulsing experiment. The lattice is turned on instantaneously at $t = 0$ and held on for a variable amount of time until being turned off instantaneously at a final time $t = t_f$. (b) Atomic population before $t = 0$. The dispersion relation is that of a free particle, and all of the atoms start out at $q = 0$ in the lowest energy level. Here, the area of the dots is proportional to the fractional population in the energy state. (c) Atomic population after the lattice is turned on for a lattice depth of $V_0 = 8.0 E_L$. The energy spectrum now shows the lattice band structure, and some atomic population is projected onto the excited bands. (d) Atomic population after the lattice is snapped off at $t_f = 150 \mu\text{s}$. The wavefunction is projected back onto the bare states, with some fraction (blue circle) in the lowest band at $k = 0$ and some fraction in the excited band, with equal population being projected onto the $k = 2k_L$ (green) and $k = -2k_L$ (red).

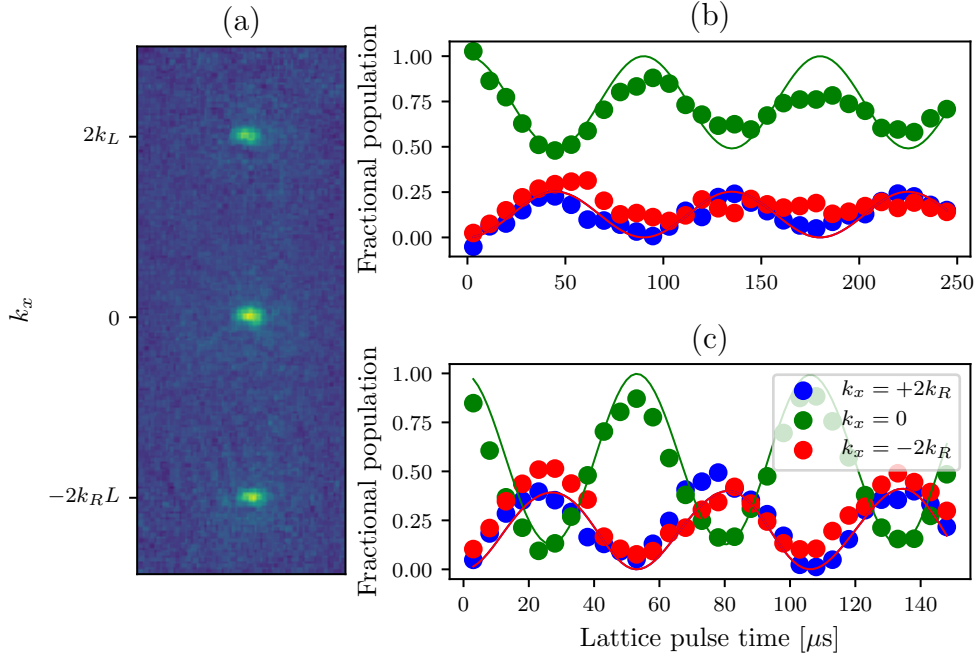


Figure 7: Lattice pulsing for calibration. (a) An example time-of-flight image from a pulsing experiment. The three different clouds are different momentum orders. (b) Fractional populations in the different momentum orders as a function of pulsing time at a low lattice power. Data is indicated by dots and best fit theory is represented by lines. The lattice depth from fit is $V_0 = 5.57 \pm 0.07 E_L$. (c) Fractional populations in the different momentum orders as a function of pulsing time at a higher lattice power. Data is indicated by dots and best fit theory is represented by lines. The lattice depth from fit is $V_0 = 12.69 \pm 0.07 E_L$.

examples of these pulsing experiments are presented in figure 7b,c.

In contrast to pulsing, adiabatic loading turns the lattice on slowly, such that the atomic wavefunction starting in the bare ground state can continuously adjust to remain in the ground state of the current Hamiltonian, without projecting onto any of the higher bands. This process is illustrated in Figure 8. The adiabatic timescale depends on the spacing between the ground and next excited band (or if starting in a different eigenstate, the nearest eigenstate). If the energy difference between the ground and first excited state is ΔE , the timescale on which the lattice is turned on must fullfill $t \gg \hbar/\Delta E$.

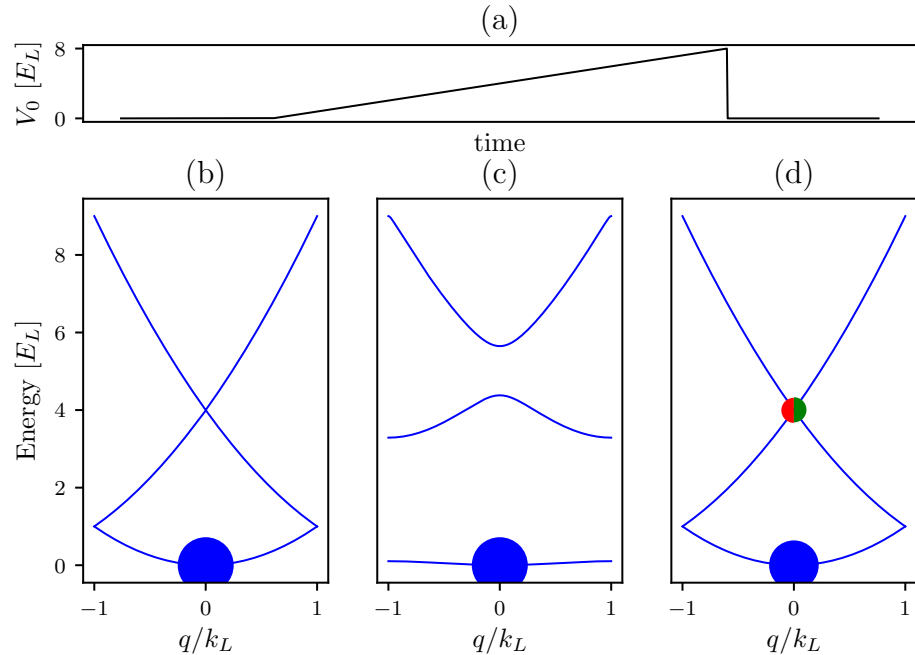


Figure 8: Adiabatic lattice loading. (a) Lattice depth as a function of time during adiabatic turn-on. The lattice is ramped on starting at $t = 0$, slowly increasing to a final lattice depth and turned off instantaneously at a final time $t = t_f$. (b) Atomic population before $t = 0$. All atoms are at $k = 0$ in the lowest bare band. (c) Atomic population after the lattice is turned on adiabatically to a lattice depth of $V_0 = 8.0 E_L$. All atoms remain in the lowest band, but the band is no longer bare. (d) Atomic population after the lattice is snapped off. The wavefunction is projected back onto the bare states, with some fraction (blue circle) in the lowest band at $k = 0$ and some fraction in the excited band, with equal population being projected onto the $k = 2k_L$ (green) and $k = -2k_L$ (red). Since the lowest lattice band is a superposition of bare bands, some atoms are excited to the higher bare bands.

1.6 Raman and rf coupling

In this section, we will introduce Raman and rf coupling between the hyperfine sublevels of the ground state of ^{87}Rb . While we will focus on the $F = 1$ and $F = 2$ manifolds of this ground state due to their relevance to the experiments described in Chapters ??, the discussion can be easily extended to any value of F .

1.6.1 Rf coupling Hamiltonian

For the $F = 1$ manifold, there are three available spin states $m_F = 0, \pm 1$. There are many ways of introducing coupling terms between the different hyperfine states. Here, we will explain two methods: rf coupling and Raman coupling. Rf coupling is a radio-frequency oscillating magnetic field, in our case produced by a pair of circular coils in series side by side above the atoms (see [10]). Assuming the rf oscillating field is polarized along the \mathbf{e}_x , with the bias field along \mathbf{e}_z , the coupling Hamiltonian is given by $H_{rf} = \mu_B g_F \vec{\mathbf{F}} \cdot \vec{B} = \mu_B g_F \mathbf{F}_x B_x \cos(\omega t)$, where $2\pi\omega$ is the rf frequency. The schematic of this setup is shown in Figure 9. The eigenstates of the bare Hamiltonian H_0 are the constituent m_F states. The eigenstates of the coupled Hamiltonian $H_0 + H_{rf}(t)$ can be expressed as a linear superposition of the bare eigenstates $\Psi(\vec{x}, t) = \sum_{m_F} c_{m_F}(t) \phi_{m_F}(\vec{x}) e^{-i\omega_{m_F} t}$. The Hamiltonian in this basis can then be written as [8]

$$H_{\text{rf}} = H_{\text{KE}} + \hbar \begin{pmatrix} 0 & \Omega \cos(\omega t) e^{i\omega_z t} & 0 \\ \Omega \cos(\omega t) e^{-i\omega_z t} & 0 & \Omega \cos(\omega t) e^{i\omega_z t} \\ 0 & \Omega \cos(\omega t) e^{-i\omega_z t} & 0 \end{pmatrix}, \quad (1.43)$$

where Ω is the Rabi frequency, proportional to B_x . We can then transfer into the rotating frame $c'_{m_F} = e^{-im_F\delta t} c_{m_F}$, where $\delta = \omega_z - \omega$. Then we apply the rotating wave approximation, that the fast oscillating terms average to zero over time scales

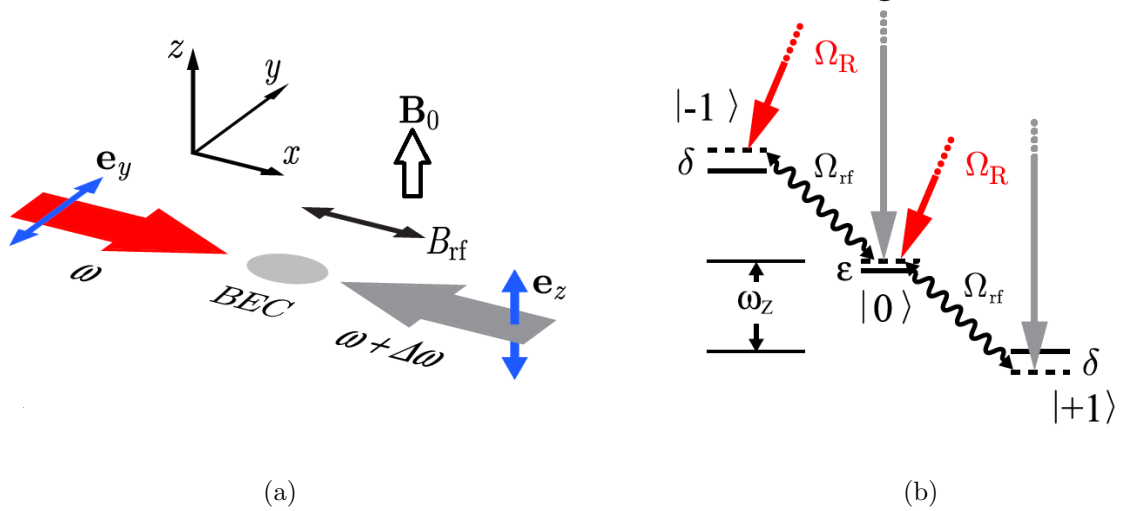


Figure 9: Raman and rf coupling schematic. (a) Beam geometry of the Raman beams and rf relative to the external field. The Raman beams have a frequency difference $\Delta\omega$, and are linearly polarized in perpendicular directions. (b) Level structure of both Raman and Rf coupling for hyperfine states of the $F = 1$ manifold. The hyperfine splitting separates the levels by an energy $\hbar\omega_z$. The quadratic Zeeman shift ϵ lowers the energy of the $m_F = 0$ state, and the detuning δ of either the Raman or the rf fields shifts the energies of the $m_F = \pm 1$ states. Raman transitions are two-photon, exciting up to a virtual state and coming back down to an adjacent hyperfine state, with an accompanying momentum transfer. Rf couples adjacent hyperfine states directly. Figure taken from ref. [11]

of interest $e^{2i\omega t} \approx 0$, and obtain

$$H_{\text{rf}} = H_{\text{KE}} + \hbar \begin{pmatrix} \delta & \Omega/2 & 0 \\ \Omega/2 & -\epsilon & \Omega/2 \\ 0 & \Omega/2 & -\delta \end{pmatrix}, \quad (1.44)$$

or for any value of F

$$H_{\text{rf}} = H_{\text{KE}} + \hbar\delta F_z + \hbar\epsilon F_z^2 + \Omega F_x/2. \quad (1.45)$$

The band structure of this Hamiltonian can be seen in Figure 10, where we have diagonalized Eq. 1.44 for a range of momenta k_x (we have isolated k_x for comparison with Raman coupling, as will be seen in the next section). The parabolas are simply

the free particle dispersion relations along one dimension, with three bands arising from the three available spin states. It is convenient to define the magnetization of an eigenstate $m = \sum_{m_F} m_F * p_{m_F}$, where p_{m_F} is the fractional population in the m_F state. We have indicated the magnetization of the eigentate by coloring the eigenenergies, with $m = -1$ in red, $m = 0$ in green, and $m = +1$ in blue. In Figure 10a, both the detuning and the coupling strength are zero. Therefore, there are simply three free particle dispersions, each exactly correlated with a particular spin state, the $m_F = \pm 1$ are degenerate and the $m_F = 0$ state is slightly offset by the quadratic shift $\hbar\epsilon$. In Figure 10c, the coupling strength is again zero, but the detuning has been turned on, lifting the degeneracy between the $m_F = \pm 1$ states. Figure 10b,d shows the same conditions as a,c, respectively, but with the coupling strength turned on. In Figure 10b, where the detuning is zero and the quadratic shift is negligible compared to the coupling strength, all states average to a magnetization of zero—the $m_F = \pm 1$ states are symmetrically populated. In Figure 10d, this symmetry is broken by the presence of a detuning.

1.6.2 Raman coupling Hamiltonian

The counter-propagating Raman beams, as seen in Figure 9, couple the same states as the rf. They do so via the vector light shift created by the pair of beams. The electric field due to the right going beam (red in Figure 9a) is $\mathbf{E} = E_0 \exp(i k_R x - i\omega t) \mathbf{e}_y$, where E_0 is the amplitude of the electric field and $\hbar k_R = h/\lambda_R = \hbar\omega/c$. The electric field from the left going beam (gray in Figure 9b) is $\mathbf{E} = E_0 \exp(-ik_R x - i(\omega + \Delta\omega)t) \mathbf{e}_z$. This combines to give an effective field from the vector light shift [12] $B_{\text{eff}} \propto \mathbf{E} \times \mathbf{E}^* \propto -E_0^2 \cos(2k_R x + \Delta\omega t) \mathbf{e}_x$. Going through the same procedure as for the rf coupling case, including the transfer into the rotating frame and the rotating wave approximation, we obtain the same Hamiltonian in the basis of bare spin states $| -1 \rangle, | 0 \rangle, | 1 \rangle$ but with an extra phase factor:

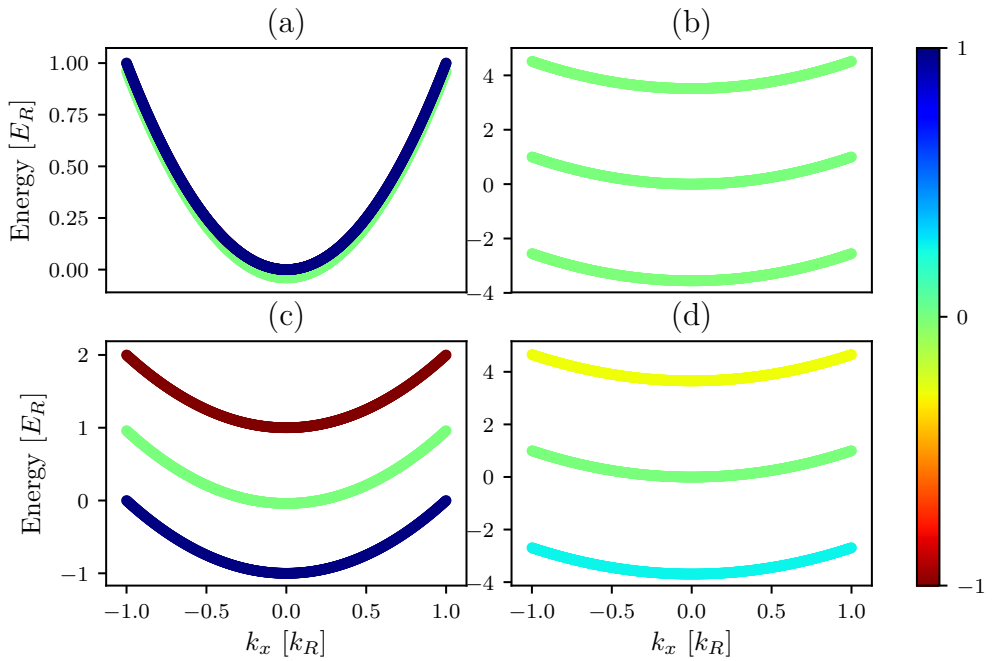


Figure 10: Band structure of the rf Hamiltonian, Eq. 1.44, in momentum space. For all plots, the quadratic Zeeman shift $\hbar\epsilon = 0.04E_R$, and the color represents magnetization, labeled by the colorbar. (a) $\hbar\Omega = 0$, $\hbar\delta = 0$. No coupling or detuning is present, so the only separation between the bands is due to the quadratic shift $\hbar\epsilon$. (b) $\hbar\Omega = 5.0E_R$, $\hbar\delta = 0$. (c) $\hbar\Omega = 0$, $\hbar\delta = 1.0E_R$. Even though the coupling strength is zero, the bands are separated by the detuning. (d) $\hbar\Omega = 5.0E_R$, $\hbar\delta = 1.0E_R$.

$$H_{\text{Raman}} = H_{\text{KE}} + \hbar \begin{pmatrix} \delta & \Omega/2e^{-i2k_Rx} & 0 \\ \Omega/2e^{i2k_Rx} & -\epsilon & \Omega/2e^{-i2k_Rx} \\ 0 & \Omega/2e^{i2k_Rx} & -\delta \end{pmatrix}, \quad (1.46)$$

where $\delta = \omega_z - \Delta\omega$.

This phase difference between the rf and Raman Hamiltonian has an intuitive physical explanation. In order to undergo a Raman transition, an atom first absorbs a photon from one beam, getting a momentum kick equal to the recoil momentum $\hbar k_R$. Then, to decay back down to an adjacent spin state, the undergoes stimulated emission into the field of the other (counter-propagating) beam, acquiring another recoil momentum kick in the same direction for a total of $2\hbar k_R \mathbf{e}_x$. Therefore, the Raman coupling Hamiltonian for $F = 1$, after transforming into the rotating frame and performing the rotating wave approximation, can be written in the same way as the rf Hamiltonian in Eq. 1.44 with the addition of a momentum kick—in real space, an acquired phase—of e^{i2k_Rx} .

We can again make a basis transformation to get rid of this phase. Let us define $| -1' \rangle = \exp(-2ik_Rx)| -1 \rangle = | k_x - 2k_R, -1 \rangle$, $| 0' \rangle = | 0 \rangle = | k_x, 0 \rangle$, $| 1' \rangle = \exp(2ik_Rx)| 1 \rangle = | k_x + 2k_R, 1 \rangle$, where for third definition we went into the momentum basis and labelled the states by a combination of their momentum and spin state. Then, including the kinetic energy term along \mathbf{e}_x explicitly, we obtain the Hamiltonian in the new basis as:

$$H_{\text{Raman}} = H_{\text{KE}}^{(y,z)} + \begin{pmatrix} \frac{\hbar^2(k_x-2k_R)^2}{2m} + \hbar\delta & \hbar\Omega/2 & 0 \\ \hbar\Omega/2 & \frac{\hbar^2k_x^2}{2m} - \hbar\epsilon & \hbar\Omega/2 \\ 0 & \hbar\Omega/2 & \frac{\hbar^2(k_x+2k_R)^2}{2m} - \hbar\delta \end{pmatrix}. \quad (1.47)$$

It is convenient to define the Raman recoil energy as $E_R = \frac{\hbar^2 k_R^2}{2m}$. The band structure of this Hamiltonian is shown in Figure 11, for several representative pa-

rameter values, with the magnetization labelled by the color. Figure 11a shows the band structure in the limit of zero coupling and zero detuning, but where we have already gone into the basis $|k_x - 2k_R, -1\rangle, |k_x, 0\rangle, |k_x + 2k_R, 1\rangle$; therefore, the free particle parabola corresponding to the $m_F = 1$ spin states is shifted to center on $k_x = -2k_R$ and the $m_F = -1$ parabola is shifted to center on $k_x = 2k_R$. As the coupling is turned on to $\hbar\Omega = 1E_R$ in Figure 11b, the points where the parabolas cross become 'avoided crossings', separating into three bands where magnetization (and the underlying spin distribution) depends on the momentum k_x . As the coupling strength is turned up even further to $\hbar\Omega = 5E_R$ in Figure 11c, the lowest band goes from having three minima, one corresponding to each original spin state, to only one minimum. This transition happens at $\hbar\Omega = 4E_R$ [10]. In Figure 11d, we show the band structure again in the limit of zero coupling, but this time with a detuning of $\hbar\delta = 1.0E_R$. Note that the detuning tips the parabolas with respect to each other. Figure 11e shows the detuned system with coupling strength turned up to $\hbar\Omega = 1E_R$, still in the three minima regime but with avoided crossings creating three momentum and spin coupled bands. In Figure 11f, the detuned system is turned up to a coupling strength of $\hbar\Omega = 5E_R$, creating a single minimum, this time offset from $k_x = 0$.

We can write the general F version of the Raman coupled Hamiltonian in the basis $|k_x + m_F * 2k_R, m_F\rangle$, where $-F \leq m_F \leq F$, as:

$$H_{\text{Raman}} = H_{\text{KE}}^{(y,z)} + \hbar^2(k_x\mathcal{I} + 2k_R F_z)^2/2m + \hbar\delta F_z + \hbar\epsilon F_z^2 + \Omega F_x/2. \quad (1.48)$$

1.6.3 Calibration of Raman and Rf dressed states

To calibrate the rf and Raman coupling strengths, we take a similar approach to the 1-D lattice calibration: start in a pure spin state, for example $m_F = 0$, and turn the coupling on non-adiabatically to induce Rabi oscillations between the

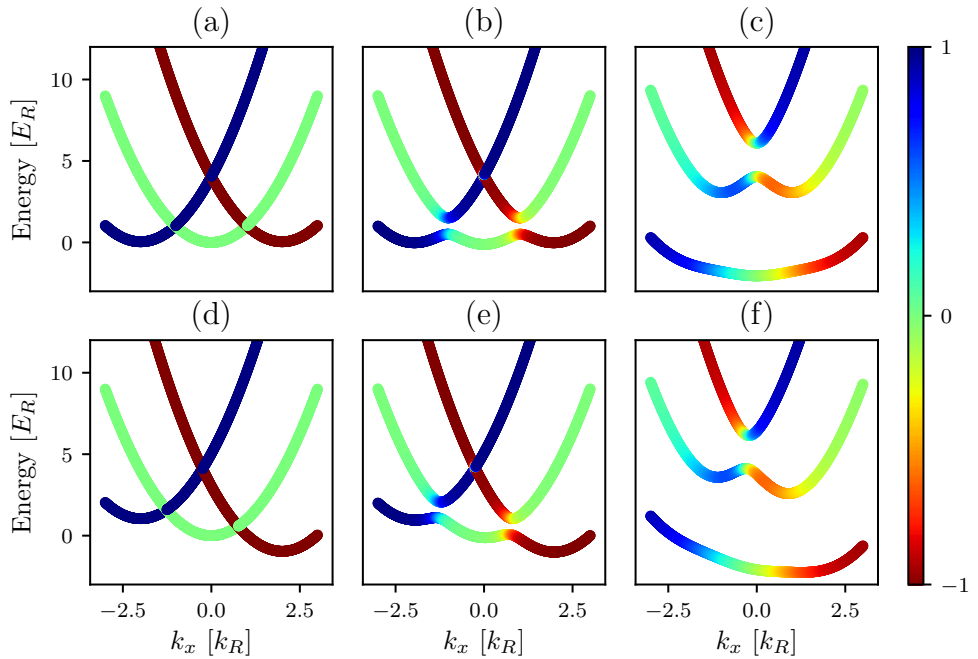


Figure 11: Band structure of the Raman Hamiltonian, Eq. 1.47, in momentum space. For all plots, the quadratic Zeeman shift $\hbar\epsilon = 0.04E_R$, and the color represents magnetization, labeled by the colorbar. (a) $\hbar\Omega = 0$, $\hbar\delta = 0$. (b) $\hbar\Omega = 1.0E_R$, $\hbar\delta = 0$. (c) $\hbar\Omega = 5.0E_R$, $\hbar\delta = 0.0$. (d) $\hbar\Omega = 0.0$, $\hbar\delta = 1.0E_R$. (e) $\hbar\Omega = 1.0E_R$, $\hbar\delta = 1.0E_R$. (f) $\hbar\Omega = 5.0E_R$, $\hbar\delta = 1.0E_R$.

coupled states. Then, during time-of-flight, apply a Stern-Gerlach gradient pulse to separate the spin components and observe the fractional populations in different spin states as a function of Rabi oscillation time.

Figure 12a,b shows example images obtained in time-of-flight when pulsing on an rf coupling field for atoms in the $F = 1$ and $F = 2$ manifold, respectively. The Stern-Gerlach gradient pulse separates the spin components along the horizontal axis in the images. The fractional population in each state can then be obtained by summing up the optical depth in each cloud and dividing by the total optical depth. Similarly, Figure 13a shows an example time-of-flight image obtained when pulsing on a Raman coupling field on an $F = 1$ cloud initially in the $m_F = 0$ spin state. Here, the spin states are separated along the horizontal axis by the same Sternch-Gerlach pulse. In addition, the recoil momentum obtained when undergoing a Raman transition separates the different spin states along the vertical axis—parallel to the Raman beams along \mathbf{e}_x . The direction of the Stern-Gerlach gradient was chosen purposefully to be perpendicular to the Raman direction \mathbf{e}_x for easy separation of the two effects.

These population oscillations can then be fit for coupling strength $\hbar\Omega$ and detuning $\hbar\delta$. Note that the quadratic Zeeman shift $\hbar\epsilon$ is set by the strength of the bias field B_0 and therefore often well known - we do not fit for this. The theoretic predictions are obtained by applying the time evolution operator $U = \exp(-iH_{\text{Raman/rf}}t/\hbar)$ to an initial state Ψ in the appropriate basis. Figure 12c shows an example time series of rf pulsing in the $F = 1$ maifold, starting in the $m_F = 0$ state. The lines of best fit are overlayed on experimental data, extracting fit parameters $\hbar\Omega = 0.863 \pm 0.004E_R$ and $\hbar\delta = -0.198 \pm 0.007E_R$. Figure 12d shows an example time series of rf pulsing in the $F = 2$ maifold, starting in the $m_F = -2$ state. Here, the extracted fit parameters were $\hbar\Omega = 1.000 \pm 0.002E_R$ and $\hbar\delta = -0.061 \pm 0.001E_R$.

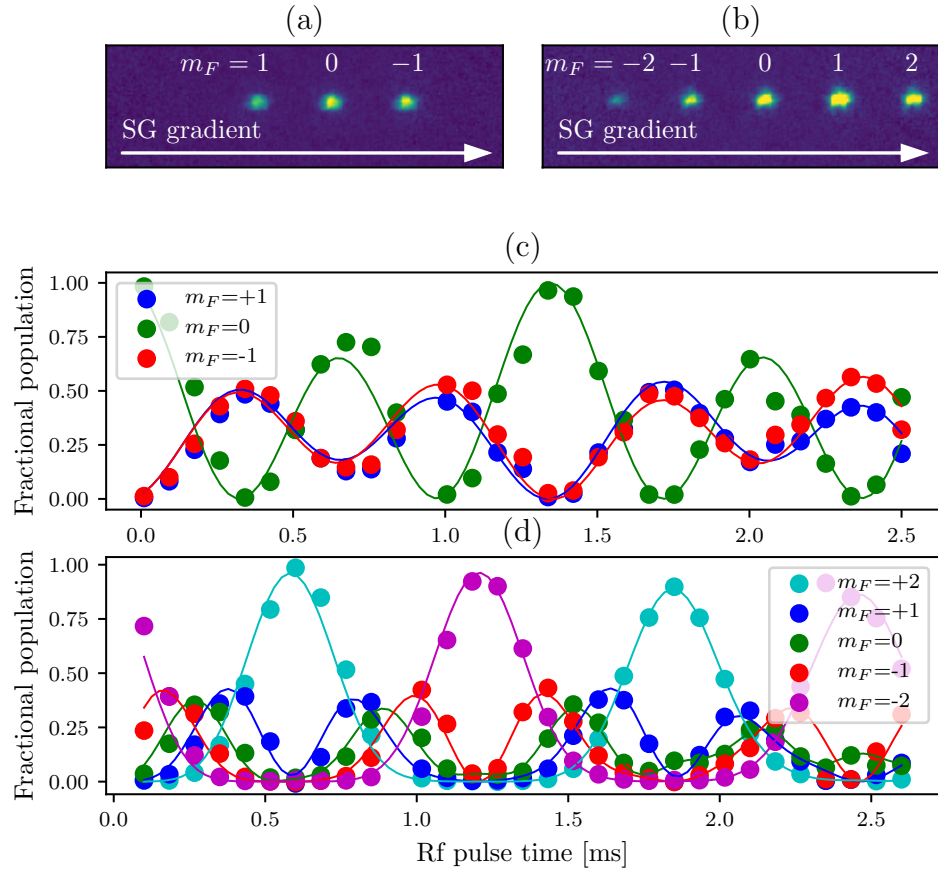


Figure 12: Pulsing on rf coupling. (a) Example time-of-flight image during an rf pulsing experiment in the $F = 1$ manifold. Spin states are separated via a Stern-Gerlach pulse along the horizontal direction. (b) Example time-of-flight image during an rf pulsing experiment in the $F = 2$ manifold. Here, 5 spin components are present. (c) Pulsing experiment in the $F = 1$ manifold. Dots represent fractional populations in different spin states measured from time-of-flight images, and lines represent best fit theory curves. Fitted parameters are $\hbar\Omega = 0.863 \pm 0.004E_R$, $\hbar\delta = -0.198 \pm 0.007E_R$. (d) Pulsing experiment in the $F = 2$ manifold. Dots represent fractional populations in different spin states measured from time-of-flight images, and lines represent best fit theory curves. Fitted parameters are $\hbar\Omega = 1.000 \pm 0.002E_R$, $\hbar\delta = -0.061 \pm 0.001E_R$. $\hbar\epsilon = 0.038E_R$ for all panels.

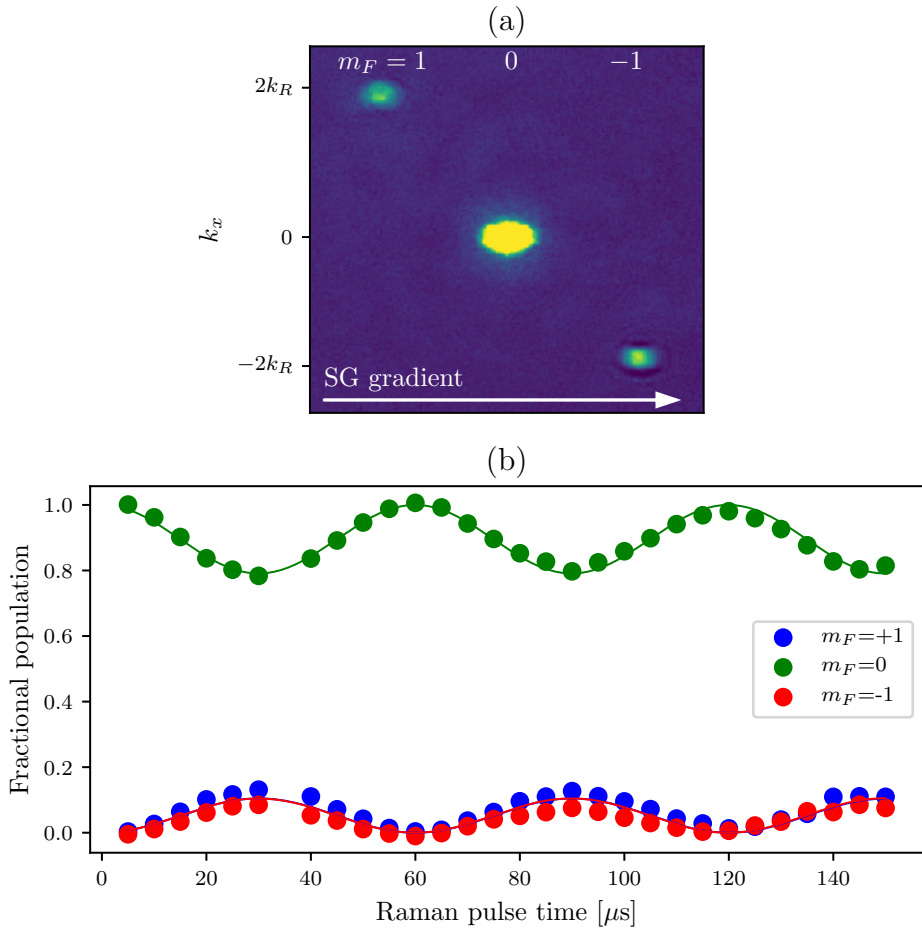


Figure 13: Pulsing on Raman coupling. (a) Example time-of-flight image during a Raman pulsing experiment in the $F = 1$ manifold. A Stern-Gerlach pulse during time-of-flight separates different spin components along the horizontal direction, and different momentum orders fly apart along the vertical direction. (b) Fractional population in different spin states during a Raman pulsing experiment as a function of time. Dots represent data and lines represent a best fit from theory. The fitted parameters are $\hbar\Omega = 1.47 \pm 0.01E_R$, $\hbar\delta = 0.004 \pm 0.024E_R$. The quadratic Zeeman shift was $\hbar\epsilon = 0.038E_R$.

Figure 13b shows an example time series of Raman pulsing in the $F = 1$ manifold, starting in the $m_F = 0$ state, with fitted parameters $\hbar\Omega = 1.47 \pm 0.01E_R$ and $\hbar\delta = 0.004 \pm 0.024E_R$. Note that although the coupling strength is almost double the rf coupling strength in Figure 12c, the contrast (peak to peak oscillation of the fractional population in, say, the $mF = 0$ state) is much lower in the Raman data than in the rf. This is a direct consequence of the recoil momentum transfer, and can be understood by looking at the band structure. For rf, the coupled bands at initial momentum $k_x = 0$ are separated by the coupling strength, see Figure ??b. For Raman, even at zero coupling strength, due to the shifting of the parabolas by $2k_R$, and $k_x = 0$ the higher bands are $\hbar^2(2k_R)^2/2m = 4E_R$ separated from the lower bands. Therefore, the energy difference is larger and the fraction in the excited band will be lower, leading to lower contrast.

Chapter 2: Ultracold Gases and the RbK apparatus

2.1 Bose-Einstein condensation

2.1.1 Phase transition of a non-interacting Bose gas

Bose gases are characterized by the Bose-Einstein distribution giving the number of atoms $n(E_j)$ occupying each energy eigenstate E_j as

$$n(E_j) = \frac{1}{e^{(E_j - \mu)/k_B T} - 1}, \quad (2.1)$$

where k_B is the Boltzmann constant, T is the temperature in Kelvin, μ is the chemical potential. Assuming the total atom number N is fixed, the chemical potential $\mu(T, N)$ ensures that the total occupation of all $\sum_j n(E_j) = N$.

The Bose distribution leads to Bose-Einstein condensation, the collapse of a macroscopic fraction of the atoms into the ground state. This comes as a direct consequence of the Bose distribution's characteristic -1 in the denominator. Consider the occupation number $n(E_j)$ —it must remain positive, as a negative occupation number is unphysical. That means that the quantity $e^{(E_j - \mu)/k_B T}$ must remain greater than 1, or $(E_j - \mu)/k_B T < 0$ for all E_j . Therefore, $\mu \leq E_0$, where E_0 is the ground state energy.

Then, for a given temperature T , there is a maximum occupation number for each excited state given by $n(E_j) = \frac{1}{e^{E_j/k_B T} - 1}$. The only energy state whose occupation number is unbounded is the ground state, as $n(E_0)$ tends toward infinity as μ

tends towards 0. Therefore, as the temperature decreases, the maximum occupation of each excited state decreases until they can no longer support all of the atoms. The remaining atoms then have no choice but to collapse into the lowest energy level and Bose condense.

We will show this quantitatively for the case of a 3-D harmonically trapped gas of atoms, relevant to the experiments described in this thesis. It is convenient to define the fugacity $\zeta = e^{\mu/k_B T}$, and re-write the Bose-Einstein distribution as eigenstate E_j as

$$n(E_j) = \frac{\zeta}{e^{E_j/k_B T} - \zeta}. \quad (2.2)$$

The harmonic oscillator potential can be written as

$$V(r) = \frac{1}{2}m(\omega_x^2x^2 + \omega_y^2y^2 + \omega_z^2z^2), \quad (2.3)$$

where ω_x , ω_y and ω_z are the angular trapping frequencies along \mathbf{e}_x , \mathbf{e}_y , and \mathbf{e}_z . The eigenenergies with this potential are

$$E(j_x, j_y, j_z) = \left(\frac{1}{2} + j_x\right)\hbar\omega_x + \left(\frac{1}{2} + j_y\right)\hbar\omega_y + \left(\frac{1}{2} + j_z\right)\hbar\omega_z. \quad (2.4)$$

In order to find μ , we must find $\sum_{j_x, j_y, j_z} n(E(j_x, j_y, j_z))$ and set it equal to N . This task is greatly simplified by going to the continuum limit and finding the density of states. To do this, we neglect the zero-point energy (setting $E_0 = 0$, the effects of the zero-point energy are discussed in [13] section 2.5) and assume there is on average one state per volume element $\hbar^3\omega_x\omega_y\omega_z$. Then, the total number of states with energy less than or equal to some value ϵ is given by the volume of a prism made between points $(x, y, z) = (0, 0, 0), (\epsilon, 0, 0), (0, \epsilon, 0)$ and $(0, 0, \epsilon)$ in units of the volume element:

$$G(\epsilon) = \frac{\epsilon^3}{6\hbar^3\omega_x\omega_y\omega_z}. \quad (2.5)$$

The density of states is given by

$$g(\epsilon) = \frac{d}{d\epsilon}G(\epsilon) = \frac{\epsilon^2}{3\hbar^3\omega_x\omega_y\omega_z}. \quad (2.6)$$

Note that the occupation of the ground state is not included in this continuum picture. We can therefore use it only to calculate the total number of atoms in all of the excited states:

$$N_{\text{ex}} = \int_0^\infty d\epsilon g(\epsilon)n(\epsilon) = \int_0^\infty d\epsilon \frac{\epsilon^2}{3\hbar\omega_x\omega_y\omega_z} \frac{\zeta}{e^{\epsilon/k_B T} - \zeta} = \frac{(k_B T)^3}{\hbar^3\omega_x\omega_y\omega_z} \text{Li}_3(\zeta), \quad (2.7)$$

where $\text{Li}_3(\zeta)$ is the polylogarithm function¹. We define the mean trapping frequency $\bar{\omega} = (\omega_x\omega_y\omega_z)^{1/3}$ and the harmonic oscillator energy as $\hbar\bar{\omega}$, with the thermal energy in harmonic oscillator units $\tau = k_B T/\hbar\bar{\omega}$, giving

$$N_{\text{ex}} = \tau^3 \text{Li}_3(\zeta). \quad (2.8)$$

Finding the occupation number of the ground state from the Bose-Einstein distribution

$$N_0 = \frac{\zeta}{1 - \zeta}, \quad (2.9)$$

we can then find the chemical potential, or equivalently the fugacity ζ , to satisfy

$$N = N_0 + N_{\text{ex}}. \quad (2.10)$$

This is a transcendental equation that can only be solved numerically. We present an example of the solution in Figure 1. Here, we have calculated the fractional population in different harmonic oscillator energy levels for three different temperatures, using trapping frequencies are $\omega_x = \omega_y = \omega_z = 2\pi 50$ Hz, and atom number $N = 10^6$.

¹This calculation was done with Wolfram Alpha, not Russian algebra skills

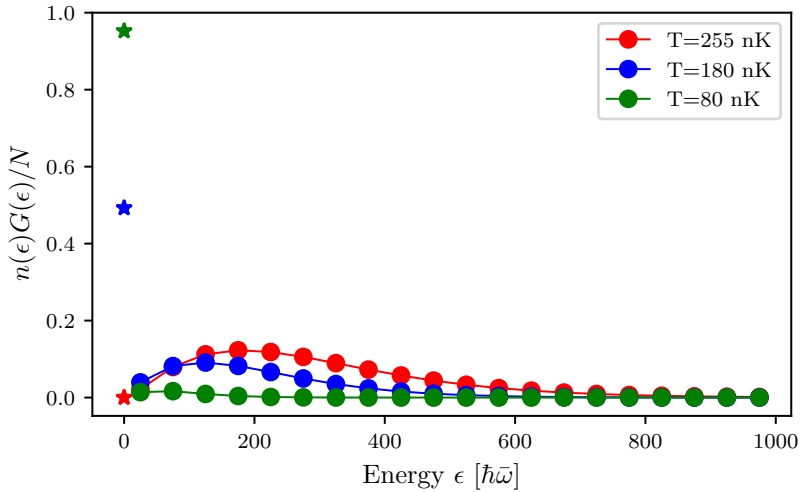


Figure 1: Occupation of energy states of a 3-D harmonic oscillator. The trapping frequencies are $\omega_x = \omega_y = \omega_z = 2\pi 50$ Hz, and the atom number is $N = 10^6$. Dots represent the total fractional population in 50 adjacent energy levels, including degeneracies. The stars represent the fractional population in just the ground state.

For energies above the ground state (dots in the figure), we binned 50 energy levels together, such that each dot represents the total fractional population in 50 adjacent levels. This was obtained by integrating eqn. 2.7 from $\epsilon - 25\hbar\bar{\omega}$ to $\epsilon + 25\hbar\bar{\omega}$. The stars represent the fractional population in just the ground state, calculated from eqn. 2.9. Note that at temperature $T = 255$ nK (red), the ground state population is consistent with a continuous extrapolation from the excited state populations and is almost zero. At lower temperatures, $T = 180$ nK (blue) the ground state population is in excess of any reasonable extrapolation from the excited state fractions, and at $T = 80$ nK (green) almost all the atoms are in the ground state.

The onset of Bose-Einstein condensation occurs at a critical temperature T_c . This temperature is defined as the temperature at which the occupation number of excited states is equal to the atom number, ie when the atoms have occupied all available excited states and any remaining atoms will have to pile into the ground state. Since the maximal occupation of the excited states will occur at $\mu = 0$,

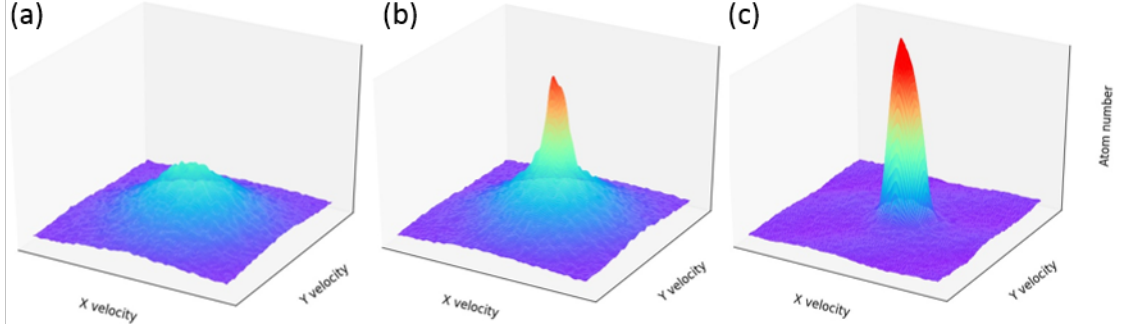


Figure 2: Time-of-flight images of atoms. (a) Above the critical temperature - the atoms are thermally distributed. (b) Below the critical temperature - about half of the atoms are condensed in the central peak. (c) Far below the critical temperature - almost all atoms are condensed in the central peak.

the occupation of the excited state is bounded from above by $N_{\text{ex}}(\mu = 0)$, and the critical temperature is defined by

$$N = N_{\text{ex}}(\mu = 0, T = T_c) = \frac{(k_B T_c)^3}{\hbar^3 \omega_x \omega_y \omega_z} Li_3(\zeta = 1). \quad (2.11)$$

Using $Li_3(1) \approx 1.202$, we obtain for a given atom number and trapping frequencies

$$T_c = \frac{1.202 N}{k_B^3} \hbar^3 \omega_x \omega_y \omega_z. \quad (2.12)$$

For the parameters in Figure 1, $T_c = 225$ nK.

For temperatures below the critical temperature, the condensation fraction f_c —the fraction of atoms in the ground state—is directly related to the ratio of the temperature to the critical temperature:

$$f_c = 1 - \frac{N}{N_{\text{ex}}} = 1 - \frac{(k_B T)^3}{\hbar^3 \omega_x \omega_y \omega_z} Li_3(\zeta = 1) = 1 - \left(\frac{T}{T_c} \right)^3, \quad (2.13)$$

where in the last step we have plugged in the definition of the critical temperature eqn. 2.12.

Figure 2 shows the progression towards condensation as the temperature of a

cloud of ^{87}Rb is decreased below T_c . The images are obtained via a time-of-flight measurement (see section 1.4.1), where the atoms are allowed to expand freely, mapping the initial momentum to final position, imaged via absorption imaging (see section 1.4). The x and y axes represent momentum along x and y , while the z axis represents the number of atoms. The z axis momentum is integrated over. Figure 2a shows a cloud above the condensation temperature - the momentum distribution is gaussian, given by the Maxwell-Boltzmann distribution. In fig. 2b, the temperature has been decreased below T_c , and about half the atoms have collapsed into the ground state, producing a large peak in atom number around zero momentum. In fig. 2c, the temperature has been decreased even further and almost all the atoms populate the central peak - the distribution is no longer gaussian but a sharp peak around zero momentum.

2.1.2 Interacting Bose gas

In the previous section, we assumed there was no interaction between the atoms other than that enforced by statistics. In this section, we will relax this assumption somewhat and describe the condensed atomic state through its characteristic Gross-Pitaevskii equation.

Since condensation occurs at very low temperatures, and thus very low kinetic energies, we can assume that any scattering processes between the atoms are s -wave and can be described simply by a scattering length a . For ^{87}Rb , relevant to experiments described in this thesis, the scattering length between two atoms in the $F = 2$ hyperfine state is $a = 95.44(7)a_0$ [14], where $a_0 = 5.29 \times 10^{-11}$ m is the Bohr radius. The short-range interaction between two particles can be approximated as a contact interaction with an effective strength U_0 as (see [13] section 5.2.1):

$$U(r_1, r_2) = U_0\delta(r_1 - r_2) = \frac{4\pi\hbar^2 a}{m}\delta(r_1 - r_2), \quad (2.14)$$

where m is the atomic mass and δ is the Dirac delta function. The full Hamiltonian of the many-body system is then

$$H = \sum_i \frac{p_i^2}{2m} + V(r_i) + U_0 \sum_{i < j} \delta r_i - r_j, \quad (2.15)$$

where i labels the particles, p_i is the momentum, r_i is the position, and V is the external potential.

We make the mean field approximation by assuming that no interactions between two atoms take them out of the ground state, and hence all atoms can be assumed to be in the same single particle wavefunction, making the overall wavefunction

$$\Psi(r_1, r_2, \dots, r_N) = \prod_i \phi(r_i), \quad (2.16)$$

where ϕ is the single particle wavefunction. It is convenient to define the wavefunction of the condensed state, $\psi(r) = \sqrt{N}\phi(r)$, making the normalization $N = \int dr |\psi(r)|^2$.

The energy of this wavefunction under the Hamiltonian above is given by

$$E = \int dr \left[\frac{\hbar^2}{2m} |\nabla \psi(r)|^2 + V(r) |\psi(r)|^2 + \frac{1}{2} U_0 |\psi(r)|^4 \right] \quad (2.17)$$

Given N particles, there are $N(N - 1)/2$ unique pairs of particles that can have a pairwise interaction, approximately equal to $N^2/2$ for large N . The N^2 is absorbed into the definition of ψ , but the factor of $1/2$ remains on the final interaction term. The task of finding the condensed eigenstate reduces to minimizing this energy under the normalization constraint $N = \int dr |\psi(r)|^2$. This can be done by using the method of Lagrange multipliers to minimize $E - \mu N$. Then, we can minimize this quantity by finding the point where the derivative with respect to ψ and ψ^* is zero.

Taking the derivative with respect to ψ^* we obtain

$$-\frac{\hbar^2}{2m}\nabla^2\psi(r) + V(r)\psi(r) + U_0|\psi(r)|^2\psi(r) = \mu\psi(r), \quad (2.18)$$

which is the Gross-Pitaevskii equation. This is a non-linear equation that generally needs to be solved numerically.

There is another approximation that can be made in cases where the atomic density is high enough that the interaction energy is significantly larger than the kinetic energy. Then, the kinetic term in the Hamiltonian can be neglected. This is called the Thomas-Fermi approximation. Then, the wavefunction is given simply by

$$|\psi(r)|^2 = \frac{\mu - V(r)}{U_0}. \quad (2.19)$$

In this approximation, the probability density simply takes the form of the inverse of the potential. In the case of a harmonically trapped BEC, it is shaped like an inverted parabola. The Thomas-Fermi radius, ie the extent of the particle wavefunction, is the point where the probability density goes to zero: $\mu - V(r_0) = 0$. For a harmonic trap, along any direction, this is given by $r_0^2 = 2\mu/m\omega^2$.

Figure 3a shows an absorption image of a small fraction of a BEC in situ (see section 1.4.1), meaning as they are in the trap - without expanding in time-of-flight. Therefore, the x and y axis represent position, while color represents the atom number. Figure 3b shows the atom number integrated over the y-axis in blue. The red dashed lines represent a best fit line to a Thomas-Fermi distribution, here an inverse parabola. The black dashed lines represent a best fit of a Gaussian to the atomic distribution. The Thomas-Fermi distribution matches the atomic distribution more closely in the center where the density is high, but the Gaussian distribution does a better job at the tails of the distribution. This is due to the presence of some thermal atoms, which remain Maxwell-Boltzmann distributed.

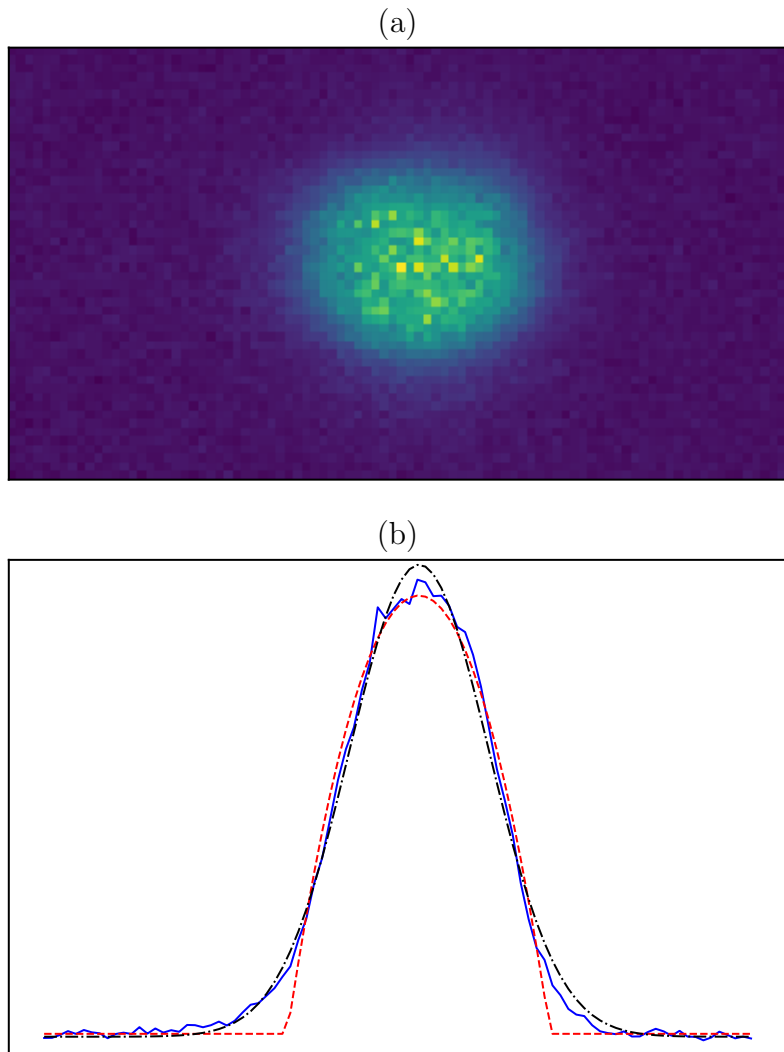


Figure 3: In situ measurement of a fraction of bose condensed atoms. (a) Absorption image taken of $\approx 1\%$ of the cloud. The x and y axes represent x and y position, while color represents the atom number. (b) The blue line represents atom number as a function of position along the x axis, integrated over the y axis. The black dashed line represents the best fit of a Gaussian function to the atomic distribution. The dashed red line represents the best fit of a Thomas-Fermi profile to the atomic distribution.

2.2 Degenerate Fermi Gas

2.2.1 Fermi statistics and the onset of degeneracy

The occupation of different energy levels by Fermions is given by the Fermi-Dirac distribution:

$$n(\epsilon) = \frac{1}{e^{(\epsilon-\mu)/k_B T} + 1}. \quad (2.20)$$

The difference from the Bose-Einstein distribution is simply the sign of the 1 in the denominator. This has important implications, however. First, since e^x varies between 0 and inf, the occupation $n(\epsilon)$ varies between 1 and 0 - a consequence of the Pauli exclusion principle. Second, as the temperature T tends towards 0, there become two distinct cases: $\epsilon - \mu > 0$ and $\epsilon - \mu < 0$. If $\epsilon - \mu > 0$, $e^{(\epsilon-\mu)/k_B T}$ tends towards inf, and $n(\epsilon)$ tends towards 0. If $\epsilon - \mu < 0$, $e^{(\epsilon-\mu)/k_B T}$ tends towards 0, and $n(\epsilon)$ tends towards 1. Therefore, at $T = 0$, the energy states below the chemical potential μ are maximally occupied (with probability 1) and the energy states above the chemical potential are unoccupied.

We can use this to determine the chemical potential at $T = 0$ by constraining the total atom number:

$$N = \sum_j n(E_j) = \sum_{\epsilon_j < \mu} 1. \quad (2.21)$$

Again, we take the common example of the 3-D harmonic trap. Then the task reduces to simply finding the number of energy levels at or below a certain energy μ . This is given by eqn. 2.5. From this, we find the chemical potential at zero energy, which is known as the Fermi energy E_F , as

$$E_F = (6N)^{1/3} \hbar \bar{\omega}, \quad (2.22)$$

where $\bar{\omega} = (\omega_x \omega_y \omega_z)^{1/3}$ is the geometric mean of the three trapping frequencies.

From the Fermi energy, we can define the associated Fermi temperature T_F as

$$T_F = \frac{(6N)^{1/3} \hbar \bar{\omega}}{k_B}, \quad (2.23)$$

and the Fermi momentum $\hbar k_F$ as

$$\hbar k_F = \sqrt{2mE_F}, \quad (2.24)$$

where m is the mass of the Fermion.

For higher temperatures, we can solve for the chemical potential, or the fugacity ζ , by integrating the Fermi-Dirac distribution weighted by the density of states (eqn. 2.6) to obtain

$$N = \int_0^\infty \frac{\epsilon^2}{2\hbar^3 \bar{\omega}^3} \frac{\zeta}{e^{\epsilon/k_B T} + \zeta} = -\frac{(k_B T)^3}{\hbar^3 \bar{\omega}^3} Li_3(-\zeta), \quad (2.25)$$

where Li_3 is again the polylogarithm function. Again, this is a transcendental equation that can be solved numerically. However, in contrast to the BEC case, we do not have to consider the ground state occupation separately, as it is bounded by 1 like every other state.

We show an example of the occupation distribution for different temperatures in Figure 4. Here, we have used the same parameter values as for the BEC case: $N = 10^6$ and $\omega_x = \omega_y = \omega_z = 2\pi 50$ Hz. The Fermi temperature for these parameters is $T_F = 436$ nK. For illustrative purposes, we plot $n(\epsilon)$, unweighted by the density of states $g(\epsilon)$. At zero temperature (red line in the figure), only states below the Fermi energy are occupied. At higher temperatures, the distribution is smoothed out (green and orange lines) until at the Fermi temperature there is almost no significance to the Fermi energy.

In contrast with Bose-Einstein condensation, the transition to a Degenerate

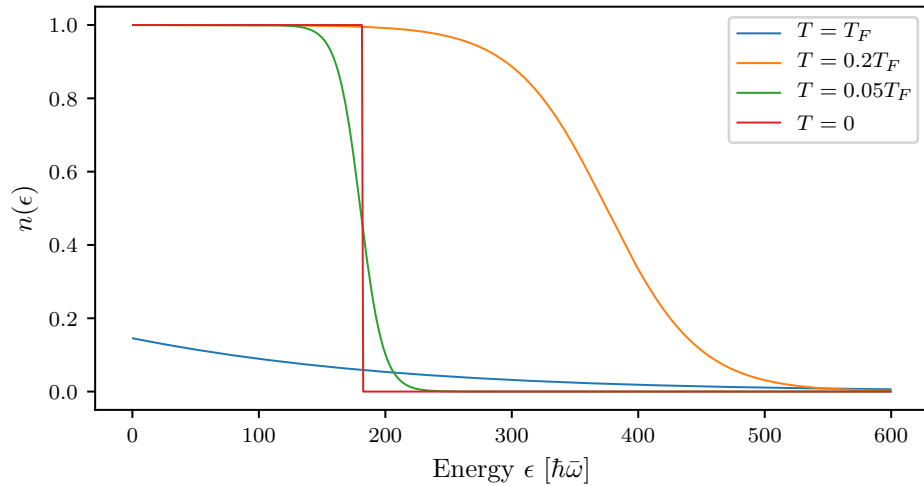


Figure 4: Occupation number as a function of energy for a Fermi gas of $N = 10^6$ atoms in a 3-D harmonic oscillator with frequencies $\omega_x = \omega_y = \omega_z = 2\pi 50$ Hz. The Fermi temperature for these parameters is $T_F = 436$ nK.

Fermi Gas (DFG) is not a phase transition, and there is no absolute measure of the onset of degeneracy. Instead, a Fermi gas can be considered degenerate when the occupation function $n(\epsilon)$ differs significantly from that of a thermal gas. This occurs when the temperature is of order $0.2T_F$.

2.2.2 Interactions and Feshbach resonances

Although the magnitude of the contact interaction U_0 for DFGs is not intrinsically different from that of BECs. There are, however, two key differences. First, the Pauli exclusion principle forbids s -wave interactions between atoms of the same spin. Higher partial wave interactions are 'frozen out' at low temperatures, when the impact parameter of the collision becomes larger than the effective cross section of interactions (see [15], sec. 2.1.2). Therefore, in order to observe interactions, and indeed to cool the gas to degeneracy, another species needs to be present so that intraspecies s -wave interactions can occur. This can be a different atomic species or a different spin state of the same atom.

Second, the densities of standard DFGs ($\approx 10^{12}$ atoms/cm 3) are much lower than that of BECs ($\approx 10^{14}$ atoms/cm 3). Since the likelihood of two-body collisions is proportional to the atomic density ρ^2 , this leads to a much smaller effect of interactions in DFGs.

A widely used technique for enhancing interaction effects in DFGs is Feshbach resonances. A Feshbach resonance occurs between two species (either atomic species or spin species of the same atom) when the open channel, ie the two particles independently in their external potential, energetically approaches a closed channel, ie a bound molecular state of the two species, shown schematically in Figure 5a.

Generally, the atoms in an open channel are energetically sensitive to a background magnetic field B via the hyperfine interaction $H_B = \mu \cdot B$, where μ is the magnetic dipole moment. Tuning the magnetic field should therefore tune the energy of the open channel. The molecular bound state may also have an overall magnetic moment, but it is generally not identical to that of the two atoms in the open channel, and therefore varies differently with the background field. Figure 5b shows an example where the bound state has zero magnetic moment. Here, the energy of both the closed and open channel as a function of background magnetic field B is plotted in the vicinity of a Feshbach resonance. The resonance occurs at a field B_0 where the energies of the two channels coincide.

Assuming there is at least infinitesimal coupling between the closed and open channels, as the energies of the two channels approach each other the perturbative correction term to the energy grows and the interaction between the atoms is effected. This is most easily seen in the s -wave case through changes the scattering length a . In the case where there are no inelastic two-body channels, such as for the ${}^{40}\text{K}$ resonance discussed in this thesis, the interatomic scattering length as a

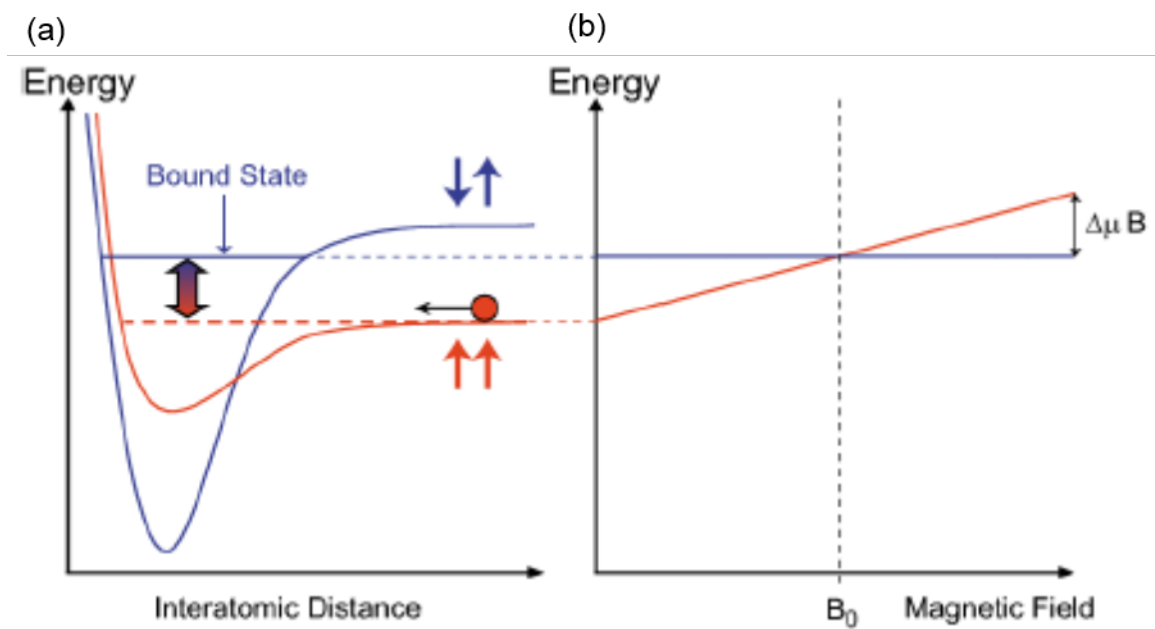


Figure 5: Schematic of a Feshbach resonance. (a) Pictoral representation of energy as a function of interatomic distance for an open channel (red) and closed channel (blue). (b) Energy as a function of background magnetic field B for the closed (blue) and open (red) channels. The energies coincide at the Feshbach resonance point B_0 . Energy of Figure taken from [15].

function of background field is given by [16]

$$a(B) = a_{\text{bg}} \left(1 - \frac{\Delta}{B - B_0} \right), \quad (2.26)$$

where a_{bg} is the background scattering length, Δ is the width of the resonance, and B_0 is the field value at which the resonance occurs. The scattering length diverges at the resonance.

The tunability of interactions provided by Feshbach resonances has allowed for creation of molecular Bose-Einstein condensates from Fermi gases [17–19] as well as observation of the phase transition from the Bardeen-Cooper-Schrieffer (BCS) superconducting regime to the BEC regime at sufficiently low temperatures [20–23].

2.3 RbK apparatus

The rubidium-potassium (RbK) apparatus at NIST Gaithersburg has been previously detailed in [10, 24, 25]. In this thesis, we will give a brief overview of the apparatus and how it is used to produce BECs of ^{87}Rb and DFGs of ^{40}K , and only give detailed documentation for those parts of the apparatus that differ from previous works.

A photograph of the main experiment is shown in Figure 6. This is mounted on an optical table, with the science chamber elevated above the surface of the table. The atoms start at the ovens (off to the right, not in the photograph) and travel down the Zeeman slower until they are trapped in the science chamber. The optical dipole trap laser, as well as the 1-D optical lattice laser, are located on the optical table and coupled into optical fibers, which are output on the main floor of breadboard before being sent towards the atoms. All other lasers are located on other optical table and brought over to the experiment table via optical fibers.

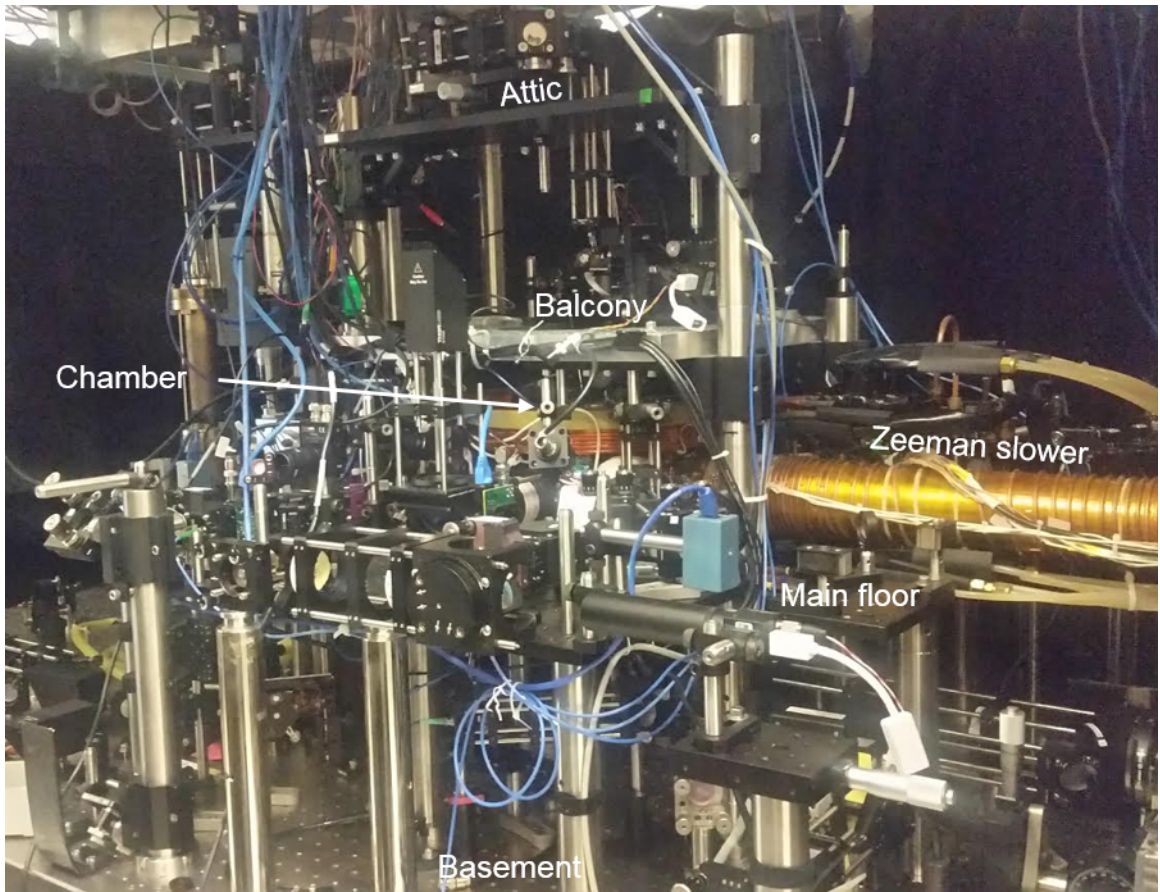


Figure 6: Photograph of RbK apparatus at NIST Gaithersburg. The main science chamber is at the center, hidden behind optics and coils. The Zeeman slower connects the atomic ovens (not shown) to the chamber. There are several levels of breadboards on which optics are mounted, labelled here as basement (surface of optical table), main floor, balcony and attic.

2.3.1 Laser beams

Figure 7 details the beam paths of the light going through the atoms. Figure 7a shows a side view of the apparatus. The up and down going MOTcooling beams are shown in red, reaching the atoms when the flipper mirrors M_{top} and M_{bottom} are flipped in. The down going probe beam, used for imaging along the $x - y$ axis both in situ and in time-of-flight, is shown in solid blue. The probe beam is split via a polarizing beam splitter cube to allow for both in situ and time-of-flight imaging of the same cloud, shown in the inset in fig. 7b and described in greater detail in sec. 2.3.4. The dashed blue line represents the upward going probe beam introduced for alignment purposes, described in greater detail in sec. 2.3.4. The kinematic base mirror (green in the figure) is removable, and only inserted when the alignment beam is in use.

Figure 7b show's a bird's eye view of the apparatus, with optics on the main floor breadboard. The slower cooling (solid dark blue) and slower repump (dashed dark blue) are coming in from the left to slow the atoms as they are moving through the Zeeman slower. The remaining four MOT cooling beams, coming from four opposing directions, are shown in red. They reach the atoms when their flipper mirrors, $M1 - 4$, are flipped in. All six flipper mirrors are computer controlled by the same digital channel, so they can be flipped in and out together. Only the beams going in through mirrors $M1$ and $M2$ are accompanied by MOT repump light, dashed red lines. The repump light for ^{87}Rb (both MOT and slower) comes from a Toptica DL-100 laser. The cooling light (MOT, slower) as well as imaging beams, come from a Toptica TA-100 tapered amplifier system. Both laser are frequency referenced against a master laser, a toptica DL-pro, which is frequency stabilized to a ^{87}Rb atomic transition via saturation spectroscopy (see section 2.3.4).

The optical dipole trap beams (solid green) come from the same 1064 nm laser

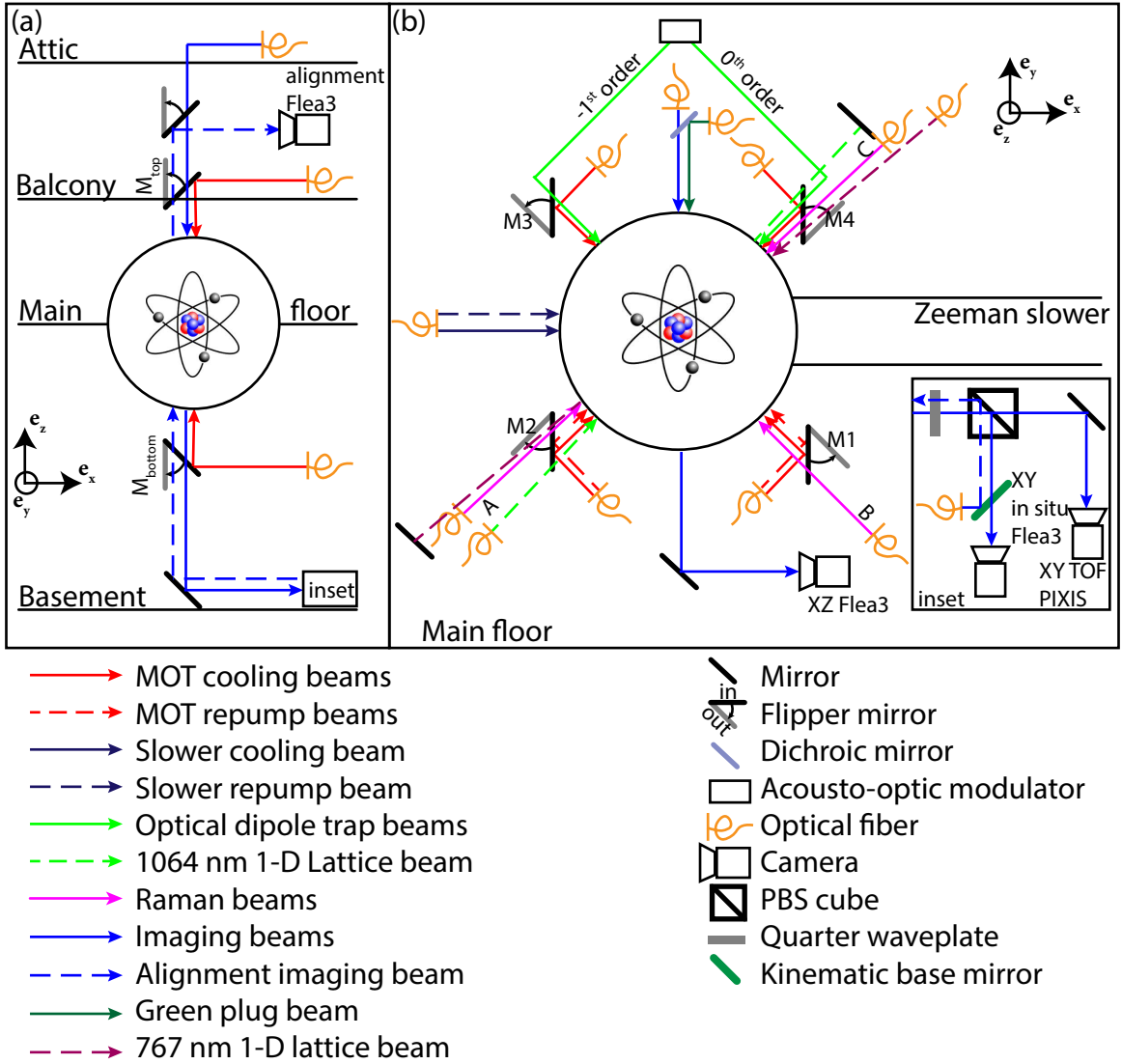


Figure 7: Schematic of RbK apparatus. (a) Side view of apparatus. Only beams propagating along the e_z direction through the atoms are pictured. (b) Top view of apparatus. Only beams propagating along the $x-y$ plane are shown. Schematic is not to scale and the angles are approximate.

(IPG YDL-30-LP), and are split via an acousto-optic modulator into two orders, which enter from opposite directions and intersect each other at approximately a 90 degree angle, providing confinement along all three axes. There is a 1-D optical lattice beam (dashed green), also 1064 nm (IPG YAR-10K-1064-LP-SF, seeded by a pick off from an NPPhotonics seed laser), sent in past the $M2$ mirror and retroreflected on the opposite end of the chamber to form a standing wave pattern. This was also used for experiments in Chapters ???. There is also another imaging beam, imaging the atoms along the x - z plane, going to a Flea3 camera.

There are three available Raman beams (solid magenta): Raman A, entering past the flipped-out $M2$ mirror, Raman B, at 90 degrees to Raman A entering past the $M1$ mirror, and Raman C, counter-propagating with Raman A and entering past the $M4$ mirror. The Raman beams are derived from a tunable Coherent MBR-110 Ti:Sapphire laser seeded by a Coherent Verdi V-10 laser. For experiments described in Chapters ???, we used the Raman A and C beams.

When ^{40}K atoms are in use, the slower cooling, slower repump, MOT cooling, MOT repump and imaging beams are all a combination of frequencies for both ^{87}Rb and ^{40}K , fiber coupled before they were sent to the main experiment table. Both the ^{40}K cooling and repump lasers are Toptica TA-pro systems, with the repump laser frequency stabilized to the ^{40}K atomic transition. In addition, a green plug beam (solid dark green in 7b) is used (see section 2.3.5), derived from a Coherent Verdi V-5 laser. For ^{40}K experiments detailed in Chapter ??, we used a near resonant retroreflected optical lattice beam, shown in dashed dark magenta entering past the $M4$ flipper mirror, coming out past the $M2$ mirror before getting retro-reflected.

2.3.2 Magnetic coils

Figure 8 is a schematic depiction of all the coils used to produce magnetic fields on the RbK apparatus. The quad coils (orange in the figure) are a large pair

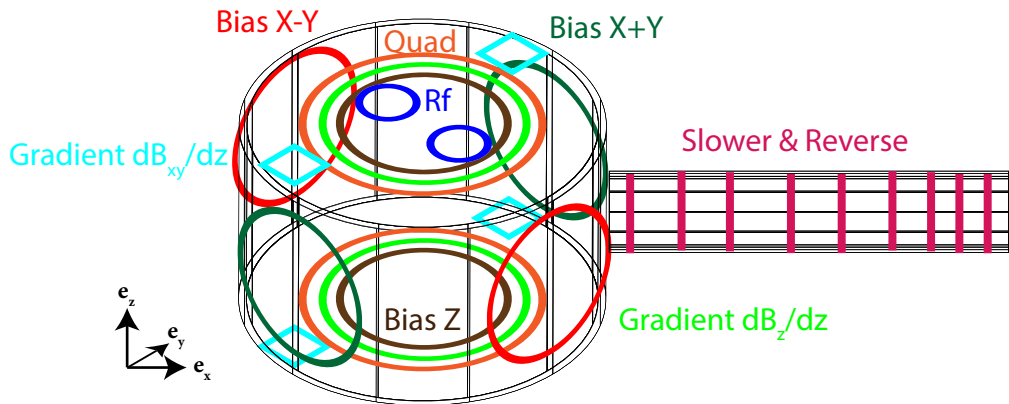


Figure 8: Schematic of magnetic coils on the RbK apparatus. The black wire frame represents the main experiment chamber, with the Zeeman slower off to the right. The Zeeman slower and reverse coils are wound around the Zeeman slower in varying spatial frequency (magenta). The quad (orange), gradient cancellation dB_z/dz (bright green) and biasZ (brown) are all pairs of identical coils on the top and bottom of the apparatus. Bias X-Y coils (red) are a pair of identical coils around the axes of the M_1 and M_3 mirrors, and the bias X+Y (dark green) are a pair of identical coils around the axes of the M_2 and M_4 mirrors. The rf coils (blue) are a pair of circular coils on top of the experimental chamber, spaced enough to allow the top MOT beam through. The gradient cancellation coils dB_{x+y}/dz (cyan) are four square coils on top and bottom of the experiment along the X+Y axis.

of coils used to produce a quadropole field for the MOT. The top and bottom coils are connected through four IGBT switches, forming an h-bridge. This allows switching between two configurations: anti-Helmholtz and Helmholtz. In anti-Helmholtz configuration, the top and bottom coils conduct current in opposite directions, producing a quadrupole field gradient at the center. This is the configuration used for the MOT, as well as for producing a Stern-Gerlach gradient for spin resolved imaging. In Helmholtz configuration, the two coils conduct current in the same direction, producing a strong bias field along the e_z direction. This was used to get close to the Feschbach resonance in the experiment detailed in Chapter ??.

There are three pairs of bias coils, used to cancel constant background fields or provide field offsets along the three axes. All three are in Helmholtz configuration. The biasZ coils (brown) are on top and bottom of the experiment and provide a constant B_z field at the center. The biasX+Y coils (dark green) are vertical on two opposite sides of the apparatus along the $e_x + e_y$ directions, and the biasX-Y (red) are on the other two opposing sides along the $e_x - e_y$ directions. There are also two sets of gradient cancellation coils available, although they are not subject to feedback loops or computer control. The first is another pair of coils on top and bottom of the apparatus (bright green), connected in anti-Helmholtz configuration to produce a small gradient dB_z/dz . The second is four square coils mounted above and below each biasX+Y coil (cyan). Both pairs of coils (a pair here is two of the square coils one above the other) are wound in Helmholtz configuration, and the two pairs are in series, providing a small gradient dB_{x+y}/dz at the atoms.

2.3.3 Procedure for making a BEC

In the first step of the BEC making procedure, the atoms starting at the oven are cooled via a Zeeman slower and captured in a Magneto-Optical trap in the siccience chamber. During this step, the Zeeman slower is on, with both the coils and the

slower cooling and repump lights on. These beams (dark blue in Figure 7b) are 7.6 MHz red detuned from the $|F = 2, m_F = 2\rangle$ to $|F = 3, m_F = 3\rangle$ transition of ^{87}Rb (133 MHz beat note offset from master laser). At the same time, the flipper mirrors $M1 - 4, M_{bottom}, M_{top}$ are flipped in and the MOT cooling and repump beams (red in Figure 7) are on. The quad coils are on in anti-Helmholtz configuration with 25 A of current running through them, producing a field gradient of $\frac{dB_z}{dz} \approx 13$ Gauss/cm. This step can be set to take anywhere from ≈ 0.7 s to ≈ 5 s depending on how many atoms are needed.

Next is the optical molasses step, during which sub-Doppler cooling of the atoms occurs. For this step, the Zeeman coils and slower lights are turned off. The quad coil current is also switched off, leaving just the MOT cooling light and only leakage MOT repump light. The MOT cooling light is set to -20.6 MHz below the $|F = 2, m_F = 2\rangle$ to $|F = 3, m_F = 3\rangle$ transition (120 MHz beat-note command). It is then linearly ramped in 19 ms down to a detuning of -90.2 MHz (50 MHz beat-note command). Since the repump light is all but off in this step, the atoms are also depumped into the $F = 1$ manifold. Then, the atoms are optically pumped into the $|F = 1, m_F = -1\rangle$ state to make them trappable by the quadrupole field. This is done by turning on the slower repump beam (dashed dark blue in fig. 7b) 1 ms. Then, the XZ imaging beam (blue in fig. 7b) is briefly turned on to get rid of any remaining $F = 2$ atoms.

Next, we compress the atoms and perform forced Rf evaporation. To compress, the quad coils are first turned on to 130 A. After holding for 20 ms, we sweep the current linearly to 250 A in 200 ms. The forced rf evaporation is then performed by turning on the rf coupling field and sweeping the frequency from 20 MHz to 4 MHz in 4 s to couple the highest energy atoms from $|F = 1, m_F = -1\rangle$ to $|F = 1, m_F = 0\rangle$ and allow them to escape the trap. The slow ramp is designed to allow the system to rethermalize through collisions as the hottest atoms are ejected. During rf evap-

oration, the crossed optical dipole trap (ODT) is on at an initial command power of 2.0 and initial split (command to AOM controlling the power split between the two crossing beams, shown in fig. 7b) of 0.01. This allows any atoms that are cold enough to see the optical trap to be captured by it.

Then, the atoms are decompressed and loaded into the ODT. The quad current is ramped down to 60 A exponentially with a time constant of $\tau = 1.5$ s in 3 s. This is the quad current at which the atoms are only barely suspended against gravity by the quadrupole trap. At the same time, the biasZ current is ramped down from 10 A to 8 A, lowering the center of the quadrupole trap to the ODT. Then, the atoms are evaporated in the ODT. This is done over the course of 5 s, ramping down the depth of the ODT and allowing the hottest atoms to escape. During this step, the ODT power is ramped exponentially from the initial command of 2.0 to a final command of 0.4, while the split command is ramped up linearly from 0.01 to 0.65, effectively turning on the crossing -1^{st} order beam. It is during this evaporation step that the atoms are cooled below the critical temperature and condensed.

Finally, the quad current is ramped exponentially to 0 A in 5 s, leaving the atoms optically trapped. Then any desired experiment can be performed on the BEC. For daily checks of the BEC, no experiments are performed and the atoms are released from the trap and allowed to expand in time-of-flight for 16.2 ms before being absorption imaged in the XY plane by the PIXIS imaging camera, pictured in fig. 7b.

2.3.4 Changes to apparatus for Rubidium

In this section, we describe a few of the changes that were made to the apparatus since the writing of Lauren Aycock’s thesis [25]. This is not an exhaustive list, but rather the most notable changes to the main setup affecting BEC production or adding capabilities to the apparatus.

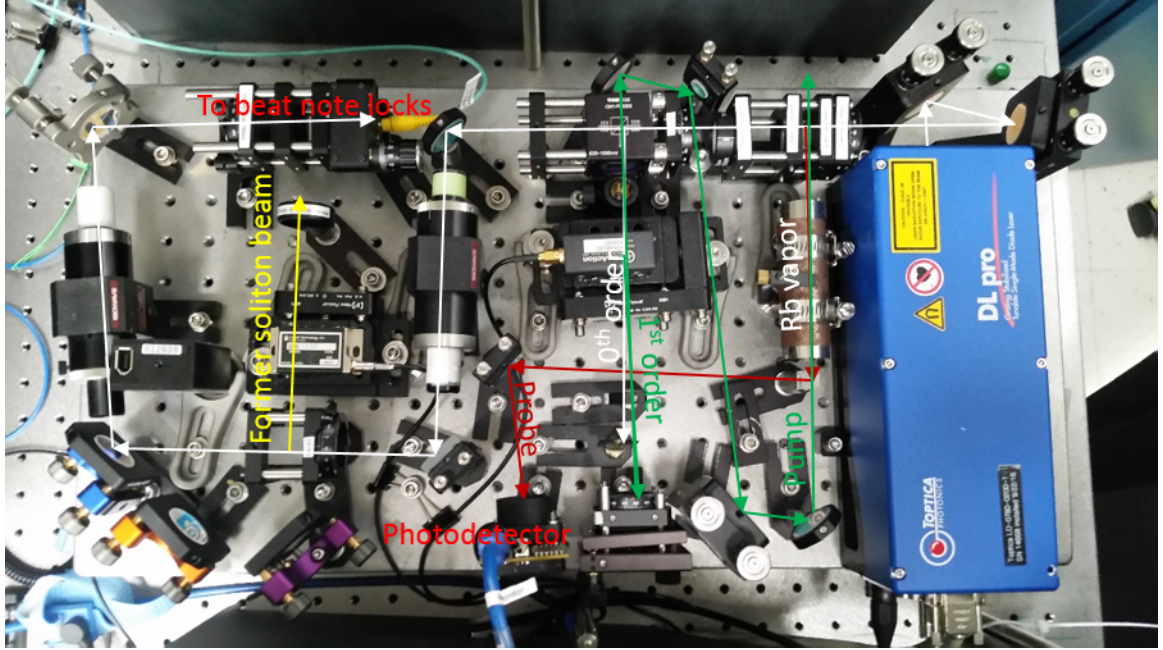


Figure 9: New master board layout.

2.3.4.1 Master laser setup

In 2014, the master laser board was replaced by a new version, with a new laser that was not dying. The laser was a Toptica DL-Pro, and it output approximately 80 mW, allowing for an extra beam arm that was used to imprint a phase shift on half the cloud to produce a soliton in the soliton project [ADD REFERENCE TO POINT IN THESIS HERE] [26].

The layout of the new master laser board is shown in Figure 9. The board contains saturated absorption spectroscopy to lock the laser frequency relative to the atomic resonance, an output port to send to the cooling and repump lasers for beat note locking and monitoring purposes, and an output port (partially dismantled in the figure) for any use if necessary. There are two mirrors directly in at the laser output, for easy re-alignment of the whole board if a diode is changed or other internal laser adjustments are made.

After hitting the two mirrors, the beam is used for saturated absorption spec-

troscopy, as describe in section 8.3 of [27]. It is first split into two branches by a polarizing beam splitter cube (PBS). The power split between the branches can be adjusted by a half wavplate (HWP) preceding the PBS. One branch is used as the probe beam in saturated absorption (red in the figure). This branch goes through the Rb vapor cell and is then sent to a photodetector. The photodetector reading is sent to a scope for monitoring and to a lock-in amplifier, used to derive the error signal for frequency locking. The rest of the beam (white) then hits another PBS cube (again preceded by a HWP to control the power split), splitting off the pump beam (green) for saturated absorption spectroscopy. This beam is sent to an acousto-optic modulator (AOM). This AOM's frequency is modulated by the lock-in amplifier [LOOK UP RELEVANT NUMBERS]. The 0th order out of the AOM is blocked by a razor blade. The 1st order is retro-reflected in a cat's eye configuration [28]. Note that after retro-reflection, the second pass through the AOM also produces a 0th and 1st order beam. This 0th order beam is not bocked, but continues along the 1st order (pump beam) path at a slightly different angle - care must be taken to avoid aligning this order to counterpropagate with the probe. The double-passed beam (1st order in both directions, so frequency shifted up twice) is then used as the pump and sent through the Rb vapor cell in the opposite direction of the probe beam.

The rest of the laser beam (white) then goes through an optical isolator, to avoid any subsequent reflections off of fiber tips or anything else from disturbing the saturated absorption frequency lock. Then, the beam hits another HWP followed by a PBS, splitting off the former soliton beam (yellow). In the figure, the soliton beam launch has been partially dismantled, but can be revived at any moment if needed. The beam was double-passed through an AOM in a cat's eye configuration before being sent into a fiber launch. The rest of the laser power (white) is sent into a fiber that is connected to a fiber splitter box, providing light for beat note locking

of the ^{87}Rb repump and cooling lasers as well as for monitoring the master laser on a wavemeter and Faby-Perot cavity.

2.3.4.2 Alignment imaging path

In 2016, there was a plan to carry out a project to create a 1D magnetic lattice whose topological character flips in the middle of the latices, predicted to support localized states at the boundary. For this, two Raman beams need to be overlapping, with one having a sharp phase change at the center of the beam, centered on the atoms. This required precise control of the beam phase as well as precise alignment of the beam to the atoms. For optimal resolution, the Raman beams were to be sent upwards through the XY imaging system. To aid in alignment, it was decided that an additional imaging path that could detect these Raman beams directly would be built. This alignment imaging path was implemented by Dr. Hsin-I Lu and is outlined in this section. All figures in this section were made by Hsin-I Lu.

The bottom part of the setup, with optics on the basement level of the experiment optical table, is diagrammed in Figure 10. One of the Raman beams, here called RamanC, first hit a spatial light modulator to imprint a phase jump. It is then combined with a second beam, here called RamanD, on a PBS. Both overlapped beams are sent backwards through the XY imaging system and up towards the atoms. The dichroic filter allowed the Raman beams ($\lambda \approx 790$ nm) to be reflected while the imaging light ($\lambda \approx 780.24$ nm) passed through to the imaging cameras. The beam for alignment imaging is also sent up to the atoms through the backwards XY imaging beam path. It entered the path via a mirror on a kinematic mount, which could be removed to allow imaging through the usual camera focused in situ in XY (see Figure 7).

To set up an alignment imaging system going upwards through the chamber,

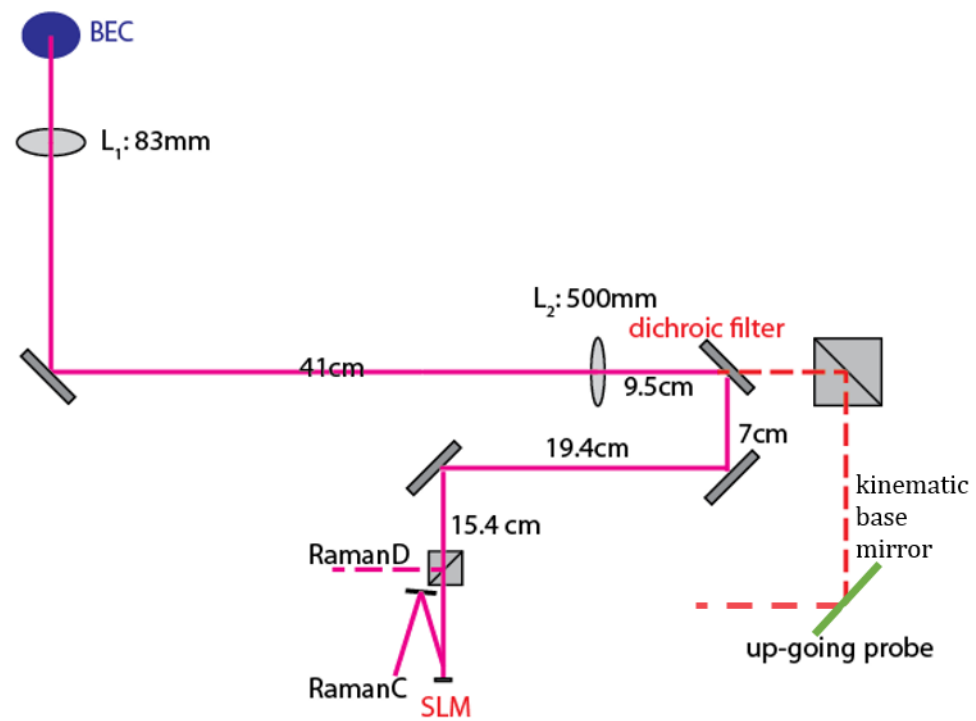


Figure 10: Schematic of the bottom half of the alignment imaging system, as well as the Raman beam set-up.

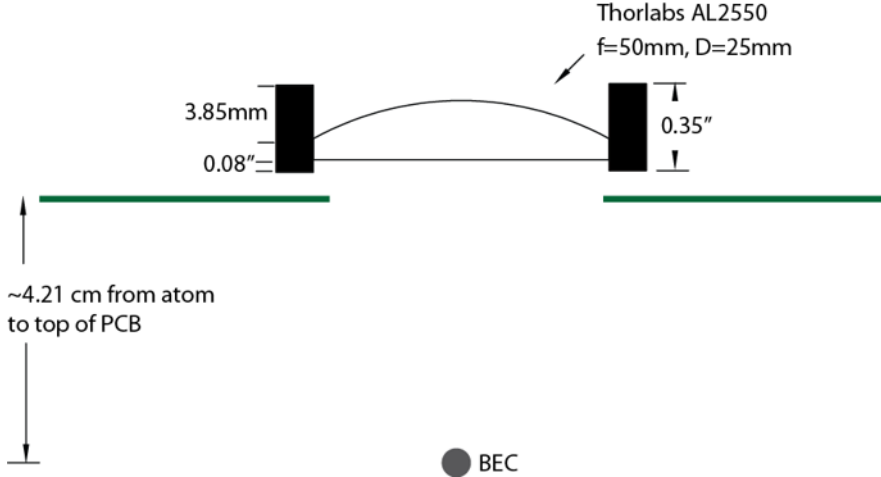


Figure 11: Schematic of the new imaging lens placed on the bucket window on top of the experimental chamber.

it was necessary to insert a new imaging lens above the chamber, as close to the atoms as possible to maximize the numerical aperture. A schematic of this lens is shown in Figure 11, it is a 25 mm diameter $f = 50$ mm aspheric lens, a Thorlabs AL2550. This lens was placed above the printed circuit board (PCB) that contains the top biasZ coil and rf coils. It was held in a custom made mount.

The top part of the imaging system is diagrammed in Figure 12. Here, the alignment probe beam is light blue. From the atoms, the alignment probe beam hits the new imaging lens (labelled L_1). Then, if the top MOT mirror is flipped out, it hits another additional flipper mirror (here M_2) before reaching a second lens and hitting an additional Flea3 camera, on the 'balcony' level of the experiment. Since the imaging lens on top of the chamber cannot be taken in and out, it was necessary to correct the down-going probe beam and down-going MOT beam, ensuring they retain their size at the atoms. For the down-going probe beam, this was done by installing a telescope to expand the beam by a factor of 4 (L_6 and L_5 in the figure) and then add a lens (L_4 in the figure) that forms a telescope with the imaging lens to reduce the beam back down by a factor of 4. The MOT beam was corrected by switching the focusing lens directly after the MOT fiber to an $f = 100$ mm lens (L_7),

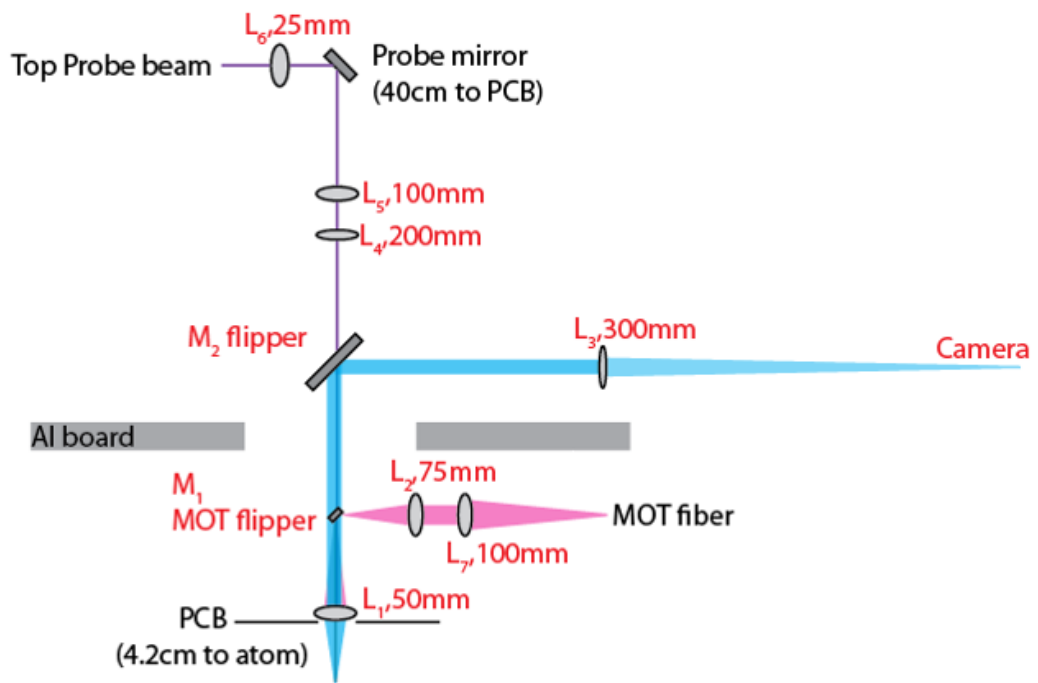


Figure 12: Schematic of the top half of the alignment imaging system, including correction optics for the MOT beam and probe beams to undo the effects of the new imaging lens.

effectively expanding the beam by a factor of $\approx 2/3$, and then adding an $f = 75$ mm lens (L_2) to form a telescope with the imaging lens, reducing the beam size by a factor of $2/3$. The adjusted beams were aligned and the experiment functioned properly. The alignment imaging system was also aligned with great effort.

2.3.4.3 FPGA quad servo

In 2014, the servo board that was used to stabilize the current in the quad coils had failed, and rather than replaced it with an identical one a new FPGA-based servo board design by Ryan Price was implemented. This design is described in detail in Appendix B of [29]. Here, we include a brief description of the design and implementation details for the quad servo at RbK.

The basic operation of the board is as follows. There are four SMA connections for input signals. These signals go to a 16 bit, 8 channel analog to digital converter ADAS3022BCPZ, then through a digital isolator Si8662BC-B-IS1, to the FPGA board. The outputs of the FPGA are sent through a similar digital isolator, Si8660BC-B-IS1 and into a 16 bit, 4 channel digital to analog converter AD5686R. Then, each of the four outputs is sent through a programmable gain amplifier AD8250ARMZ. The gain setting signal is derived from the FPGA board , by way of a serial shift register CD74HC4094. There are four SMA connections for outputs of each of the four amplifiers.

All of these devices are powered from a +/-18 supply voltage by way of three voltage regulators, LM2940C_KTT_3 for 5V regulation, LM2990_KTT_3 for -15V regulation, and LM2940CSX_KTT_3 for +15V regulation. The FPGA communication is set up through USB. There is a USB input port that connects to a USB chip FT232HL. The USB chip requires an EEPROM, in this case 93LC56BT is used. Clock timing for both the FPGA and the USB chip is provided by CTX292-LVCT. There is also a buffer SN2564BCT25244 available for amplifying digital FPGA out-

puts. The digital side of the board is also powered from a separate 5V supply by way of a 3.3V regulator LM1085_KTT_3.

The ADC specifies a 1 s conversion time per channel while the DAC settling time is 5 s to 15 bits for a 15 bit step, which suggests another 1 or 2 s of latency there. I'll be interested to see what the total loop latency comes out to. The total loop latency, as measured by sending a square wave command and reading out the error signal and taking the offset between the two is 8us.

For quad coil current stabilization, the board receives a computer command, in volts, through one of its input ports, and a Hall probe reading, in amps, through the other one. The Hall probe current sent to the servo is dropped across a stack of two 51 Ohm resistors for a total measured resistance of 25 Ohms. The difference between the two inputs, in volts, is interpreted as the error signal by the FPGA board. The control output of the board is then sent to the gate input of a MOSFET bank. The power supply powering the quad coils is connected to this MOSFET bank and then to the coils in series. Controlling the gate voltage of the MOSFETs controls the resistance the power supply sees and thus the current it outputs (it is run in voltage limited mode).

The optimal PID parameters, set via software and programmed in the FPGA board, have been found at a gain of -5 and integrator of 400 Hz. The resulting turn-on curve is shown in pink in Figure 13 a. For this curve, the computer command was hopped to 100 A and the resulting current as detected by the Hall probe was observed. The turn-on curve using the preceding servo board is shown in grey.

The board is also equipped with a digital TTL input (on the back of the board). When this digital input is high, the output control voltage is immediately railed to its lower bound. To be compatible with the MOSFETs used, the upper and lower bounds of the control output are set to 5 and 3 V respectively. The turn-off curve when this TTL switch is activated is shown in Figure 13 b. The timescale is

likely limited by eddie currents in the chamber.

We calibrated the resulting current (as measured by the Hall probe) for different voltage computer commands. This is shown in Figure 14.

Both the schematic for the servo board and the Box control program to talk to the FPGA are in the shared google drive under 'RbK/Lab Notebook/Electronics/FPGA Quad Servo (From Ryan)'. When connected, the box control program detects 'RbK Quad Servo' in its device list. In the past, several cycles of plugging and unplugging as well as turning on and off have been necessary for the connection to be successfully made.

2.3.4.4 ODT beam shaping

In 2015, two projects were being carried out on the apparatus at the same time: the soliton project [PUT REFERENCE TO PAPER IN APPENDIX HERE] [26] and the synthetic dimensions project detailed in chapter ???. The soliton project used an elongated BEC, requiring the dipole trap to be highly elongated along one direction, here $e_x + e_y$. For this, only the 0th order of the ODT was used and it was made very tight both along the horizontal and vertical directions: with 42 and 55 μm waists, respectively. The synthetic dimensions projects suffered from momentum changing collisions, and therefore needed the cloud to be as dilute as possible. For this, the 0th order ODT beam still needed to be tight in the vertical direction to suspend against gravity, but needed to be as wide as possible (while still retaining a detectable atom number) in the horizontal. Therefore, an extra cylindrical lens on a removable, rotatable mount was added in the beam path to switch between the two configurations.

The location of this new lens is detailed in Figure 15. Without this lens, the beam was sent through a telescope (the $f = 10$ and $f = 15$ cm lenses [DOESNT MAKE SENSE CHECK IF ONE IS DIVERGENT]) before reaching an $f = 25$ cm

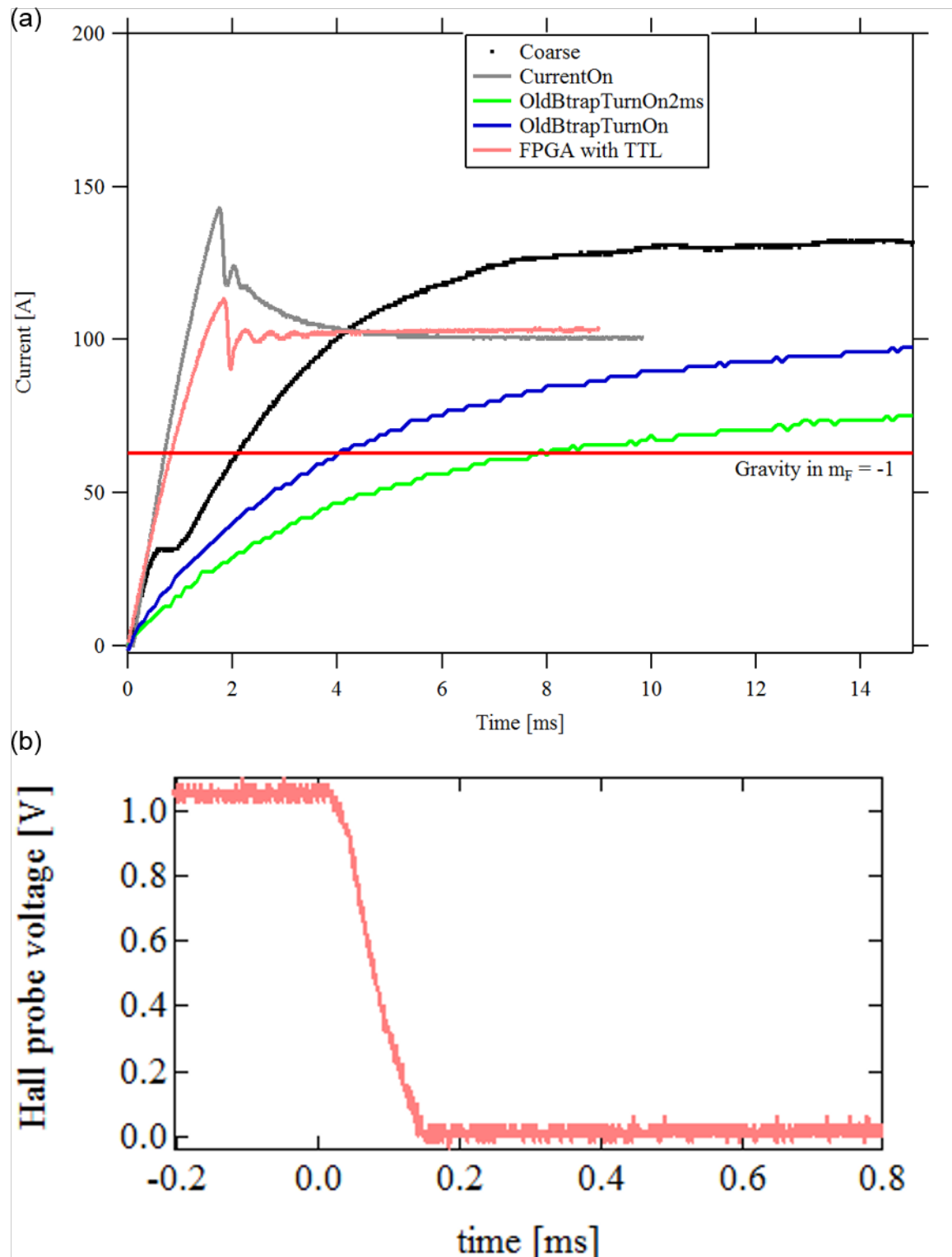


Figure 13: Turn on and off curves of the quad coils. (a) Turn-on, when computer command is jumped from 0 to 100 A . The FPGA-based servo response is in pink. The previous hardwired servo is in grey. The other curves are extraneous. (b). Turn-off with the FPGA-based servo when the TTL switch is engaged.

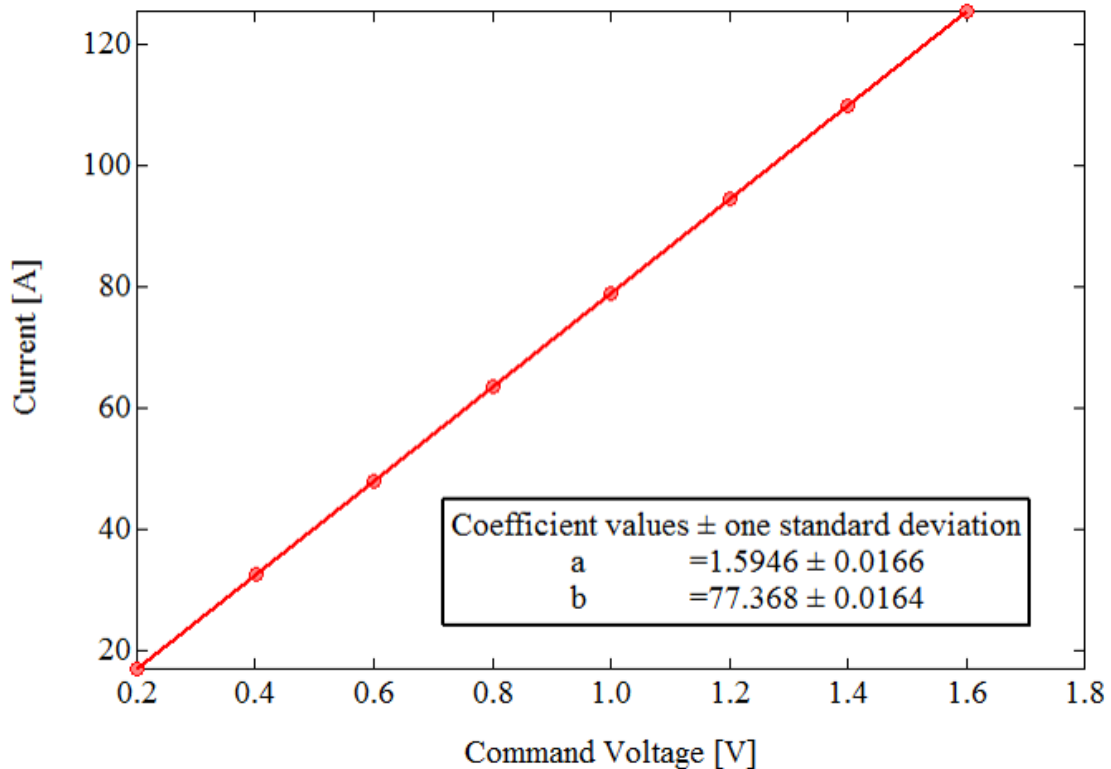


Figure 14: Output current as a function of computer command voltage for the FPGA-based servo implementation.

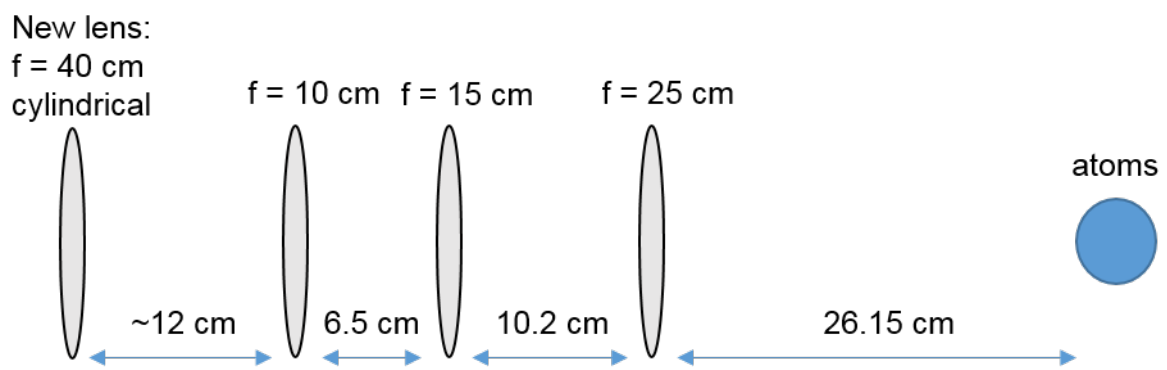


Figure 15: Schematic of beam shaping optics in the path of the 0th order ODT beam, after the split AOM. The new lens, on a removable mount, is cylindrical, shaping the beam along the horizontal axis only.

focusing lens, placed 25 cm away the center of the chamber to focus the beam at the atoms. The beam waist as a function of propagation distance along this beam path is shown in blue in Figure 16 a. This graph was made by Dr. Ian Spielman from a python calculation of gaussian beam optics. According to the calculation, the beam is focused down to a $45 \mu\text{m}$ waist at the atoms located at a displacement of 1400 mm.

The additional lens used was an $f = 40$ cm cylindrical lens, rotated in its rotating mount to focus the beam slightly in the horizontal direction. The effect of this lens on the horizontal beam waist along its path was calculated and plotted (again by Ian using his code) in Figure 16 b. This plot was made for a $f = 75$ cm lens instead of $f = 40$ cm, but the qualitative effect is the same. As seen in the figure, the waist of the beam is not significantly impacted by the addition of the lens, but the focus is shifted away from the atoms, resulting in a larger waist at the atoms. The horizontal beam waist at the atoms with the $f = 40$ cm lens as measured by a beam profiler camera was $115 \mu\text{m}$. This was the configuration used in the experiments described in Chapter 6.

2.3.5 Procedure for making a DFG

To make a degenerate Fermi gas of ^{40}K , we followed a similar cooling procedure as for making a BEC, with some key differences. First, as mentioned in sec. 2.2.2, due to the Pauli exclusion principle, spin polarized ^{40}K atoms cannot undergo *s*-wave collisions, and therefore below a certain temperature have no method to thermalize on their own and cannot be evaporatively cooled. To overcome this problem, we cooled a mixture of ^{87}Rb and ^{40}K , effectively using ^{87}Rb as a collision mechanism to allow the Fermions to thermalize. Second, ^{40}K is slightly below half the mass of ^{87}Rb . This leads to a larger magnitude of transverse velocity for ^{40}K atoms in the Zeeman slower, leading to a larger fraction of atoms missing the capture region of

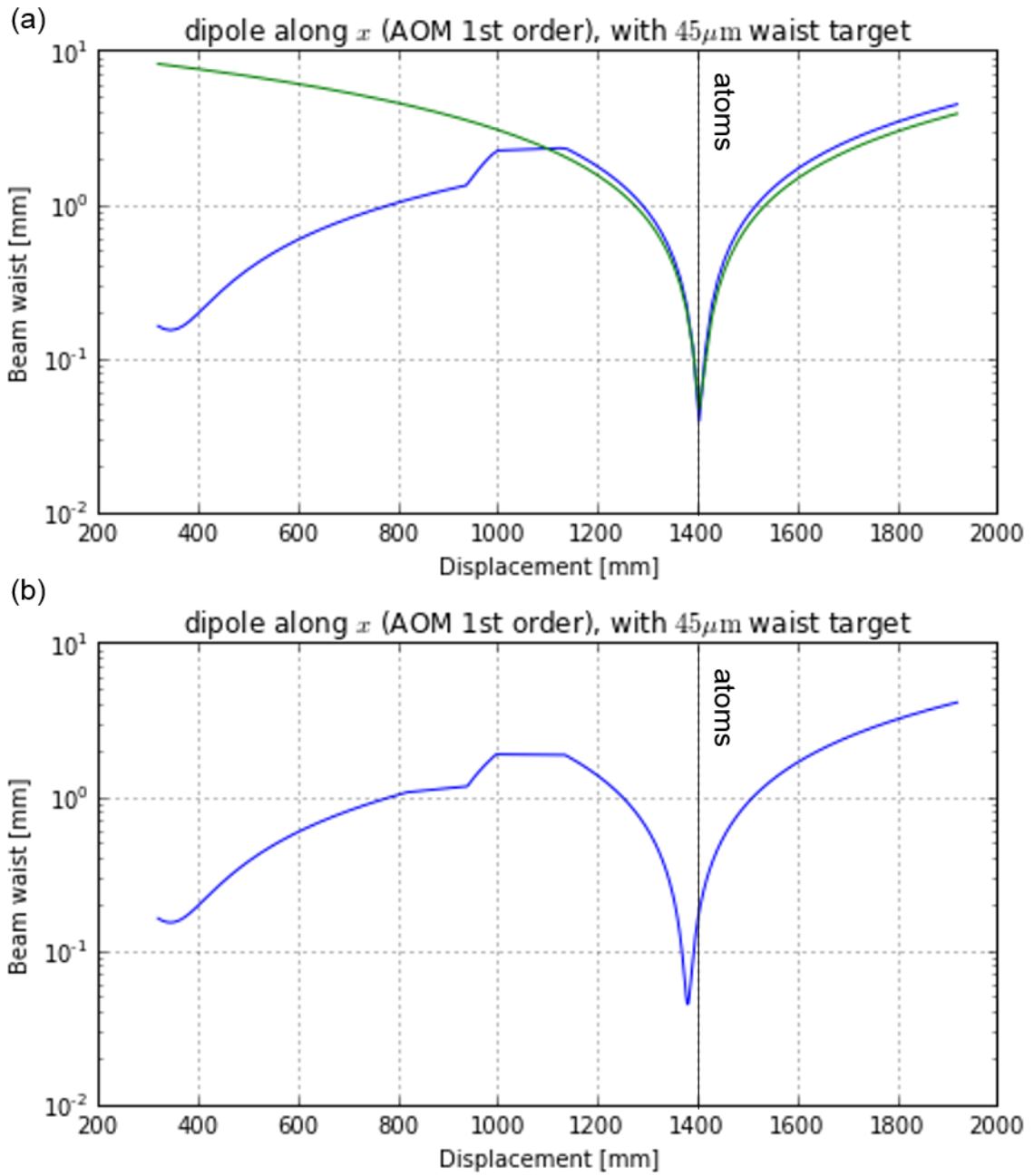


Figure 16: Beam waist as a function of propagation distance as calculated by Ian Spielman's code. Graphs also made by Ian Spielman. The atoms are at displacement = 140 cm. (a) Without additional lens. Blue line represents horizontal beam waist. (b) With an additional $f = 75$ cm lens 12 cm in before the next optic.

the MOT. To mitigate this issue, we utilized transverse cooling of ^{40}K before the Zeeman slower. This consisted of two pairs of counter-propagating beams along the $e_z + e_y$ and $e_z - e_y$ directions, performing Doppler cooling in the directions perpendicular to propagation (not shown in fig. 7b). The lower mass of ^{40}K also leads to a larger number of Majorana losses near the center of the MOT: spin flips that take the atoms out of the trappable states because they are moving too fast to adiabatically follow the changing magnetic field direction [30–32]. To mitigate this issue, for cooling ^{40}K the center of the quadrupole trap was plugged by a tightly focused green (repulsive) laser beam (dark green in fig. 7b).

First, ^{40}K atoms starting at the oven were cooled via a Zeeman slower and transverse cooling and captured in a MOT for 7 s. Then, both ^{40}K and ^{87}Rb atoms were slowed and MOT loaded for 1.5 s. The subsequent optical molasses step was only 2 ms long, with the ^{87}Rb MOT cooling light ramped linearly from -20.6 MHz below the $|F = 2, m_F = 2\rangle$ to $|F = 3, m_F = 3\rangle$ transition (120 MHz beat-note command) to -40.6 MHz away from resonance (100 MHz beat-note command). In this time, the ^{40}K cooling light was turned down in intensity but the detuning remained unaltered.

Next, ^{87}Rb was optically pumped into the $|F = 2, m_F = 2\rangle$ state using the slower cooling beam, while ^{40}K was optically pumped into the $|F = 9/2, m_F = 9/2\rangle$ state using a dedicated optical pumping beam in $250\mu\text{s}$. These are magnetically trappable states, and we subsequently turned on the quad coil current to 130 A to capture the atoms in the magnetic trap, along with the green plug beam at the center to prevent Majorana losses. Both species were compressed by a linear ramp of the quad current up to 160 A in 0.5 s. Then, forced rf evaporation was performed for 10 s, sweeping the rf frequency linearly from 18 MHz down to 2 MHz.

Then, the atoms were decompressed and loaded into the ODT, similarly to the BEC procedure. The ODT was turned on to an initial power of 2 and an initial

split command of 0.01. The quad current was ramped down to 25.5 A exponentially with a time constant of $\tau = 1.5$ s in 3 s. The evaporation in the ODT was split into two steps. During the first 3 s step, the split was ramped linearly to its final command power of 0.65, putting more power into the (less tightly focused) crossing beam. The green plug beam was ramped off during this step. During the second, 4 s step, the overall power of the ODT was exponentially ramped down to [CHECK THE INTERMEDIATE ODT COMMAND FOR K], while the quad coil current was ramped exponentially to 0.

We then used adiabatic rapid passage (ARP, see sec. 1.2.3) to transfer the ^{87}Rb atoms from $|F = 2, m_F = 2\rangle$ to $|F = 1, m_F = +1\rangle$ using a microwave coupling field and a 50 ms ramp in biasZ coil current. Then, we pulsed on the XZ imaging beam to eject any remaining $F = 1$ atoms. Then we performed one last evaporation step in the ODT, ramping the final power down to [CHECK THE FINAL ODT COMMAND FOR K]. The ^{87}Rb atoms were no longer suspended against gravity and fell out of the trap. We then were free to perform experiments with the degenerate ^{40}K cloud.

2.3.6 Current status of Potassium apparatus

At the time of writing, the ^{40}K part of the apparatus as described is no longer functional. The number of ^{40}K atoms collected in the MOT has started decaying significantly in January 2014, and by March was almost completely gone and could not be resurrected. The specific failure point of the setup was not clear. However, other groups have found that atomic sources are much more stable, and a higher fraction of the (expensive) ^{40}K sources can be utilized when the atoms were initially cooled with a 2-D MOT rather than a Zeeman slower [33–35]. Therefore, rather than continuing to attempt to revive the existing set-up, the decision was made to build a 2-D MOT for both ^{40}K and ^{87}Rb .

The design of our 2D MOT is closely based on the design in Thomas Uehlinger's diplome thesis [34]. The design was developed by Dalia Ornelas, and initially implemented by Marcell Gall before it was taken over by the rest of the RbK team. The schemtaic of the planned vacuum system (with attached optics) is pictured in Figure 17. On the left side of the schematic, there are optics directing the pushing beam into a miniconflat viewport. The viewport is part of a cross, with the ^{40}K and ^{87}Rb ovens attached to the two ends of the cross, with gate valves allowing one to close off one or both sources from the rest of the vacuum system. From there, the cross attaches to the main 2D MOT cell via a mini-conflat flange.

The cell is a custom machined stainless steel frame with rectangular anti-reflection (AR) coated windows on four sides and mini-conflat conectors on two ends, pictured in more detail in Figure 18. Two aluminum mounting crosses attach two either end of the cell. Four aluminum bars are connected between the crosses, and the main 2D MOT optics are mounted on those four bars. The opposite end of the cell (right in fig. 17) sandwiches a differential pumping tube in the mini-conflat connection and connects to another cross. The top of the cross connects to a small ion pump. The bottom connects to a rotatable feed-through mechanism with a 'flag', a square of metal, attached inside. The rotator rotates the flag in and out of the atomic beam path, providing a means of losing off the main chamber from the atomic beam and push beam light. The fourth end of the cross connects to another gate valve, separating the 2D MOT vacuum system from the main experiment chamber. The other end of this gave valve connects to a flange that is meant to connect directly to the main experiment chamber.

A picture of the stainless cell is shown in Figure 18. Attaching the glass windows to the stainless steel frame in a vacuum tight way proved to be quite difficult, and this picture was taken during one of the attempts to do so using epoxy. The clamps around the cell served to keep the windows in place as the epoxy

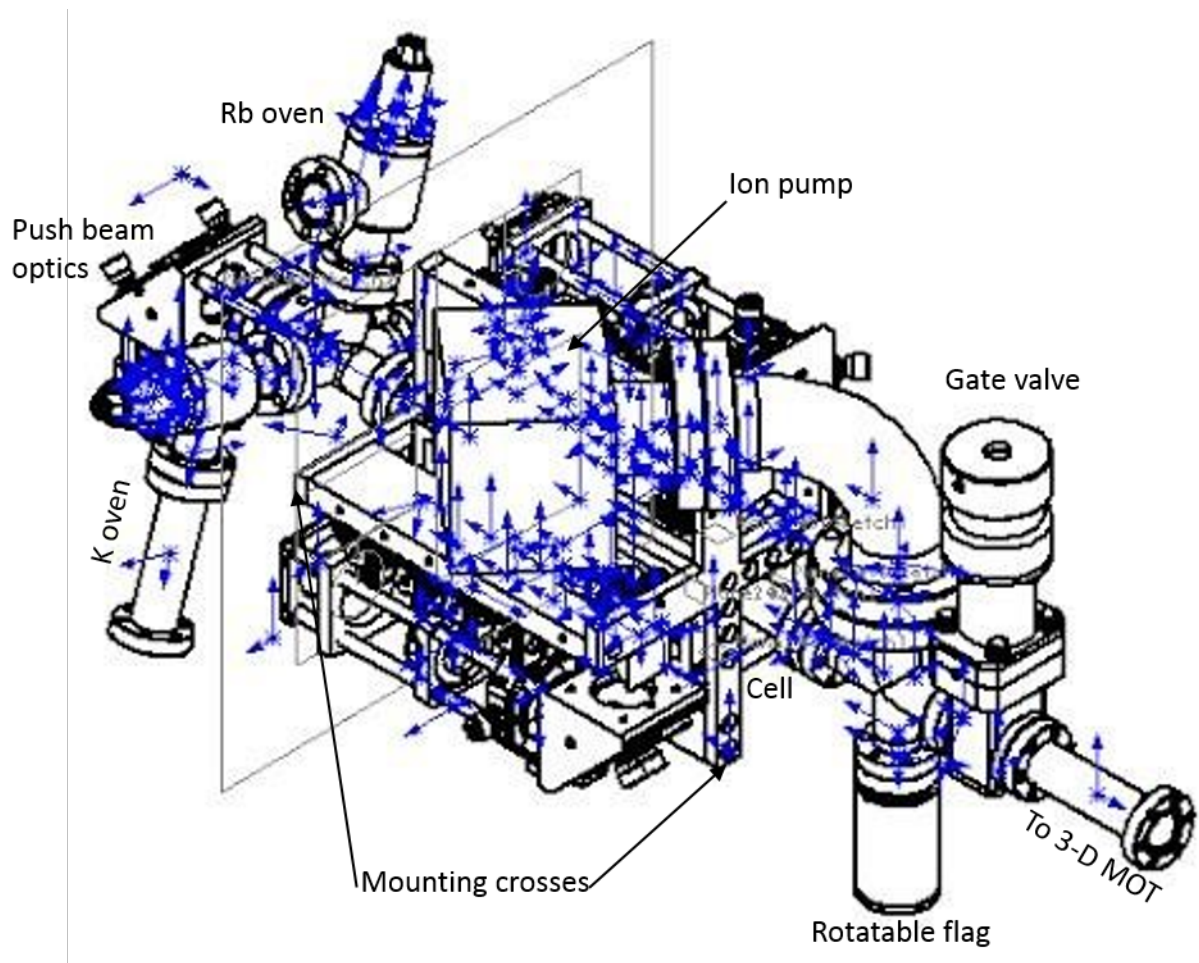


Figure 17: Schematic of the 2D MOT setup. The mini-conflat on the right is to be attached to the existing experiment chamber, directing the atomic beam into the 3D MOT.

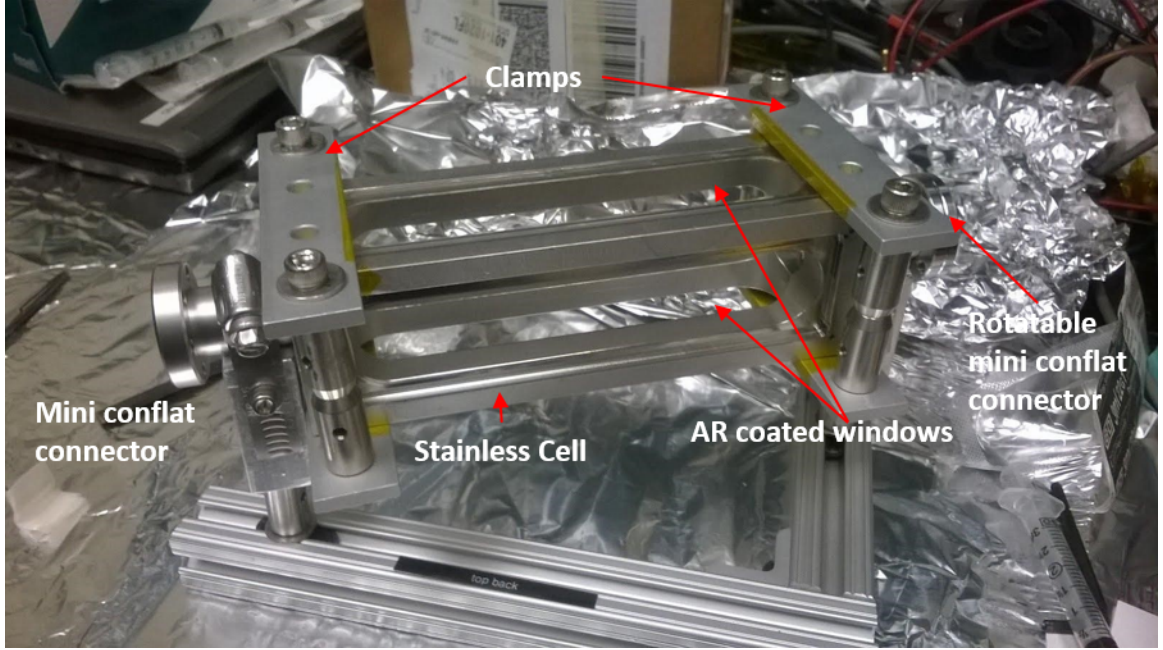


Figure 18: Picture of 2D MOT cell during an attempt to epoxy AR coated windows onto the stainless steel frame. The clamps serve to hold the windows in place while epoxy cures.

was curing. In the final design, the seal was made with indium, with gaskets custom machined to press the windows onto the cell. We roughly followed the indium sealing method presented in [36], with gaskets above and below the windows. We also employed pre-squashing, where a metal piece in the shape of the window was first pressed onto the indium wire to flatten it and minimize the amount of pressure that needed to be applied to the glass window.

The main 2D MOT optics direct the cooling and repump beams into the cell from two directions, and retro-reflect them on the other end, producing cooling along those two directions (hence the name 2D MOT). The optical set-up along one of those directions is presented schematically in Figure 19. The cell is elongated along the atomic beam direction, to maximize the time the atoms are cooled while travelling to the 3D MOT. Because of this, instead of a highly elliptical cooling beam, four MOT beams are launched in a row, almost overlapping, from each of the two directions. This is accomplished by splitting one beam into four with four sequential

beam-splitting cubes (BSs).

The 2D MOT cooling and repump light is first periscoped over from a fiber and lens assembly (designed to shape the beam to be roughly 1 inch in diameter). It then goes through a half-wave plate (HWP) before entering the first 70/30 beam splitter. 30% of the light is sent through a quarter-wave plate (QWP) tuned to provide circularly polarized light into the cell. On the other side of the cell, the beam hits another QWP before being retro-reflected back into the cell. Since the beam hits the QWP on the other side of the cell twice, the circular polarization is preserved. The remaining 70% of the light goes into the next 70/30 BS, sending 21% of the total beam power into the second arm going into the cell, to be retro-reflected in the same way. The remaining 49% hits a 50/50 BS, sending 25.5% of the total beam power into the third retro-reflected arm. The final cube is a polarizing beam-splitter (PBS), and the HWP before the cubes is tuned to ensure all of the light is sent into the cell on this last, fourth, arm.

The push beam enters from the oven direction and serves to provide some velocity to the atoms along the long direction of the cell to ensure they continue to travel to the 3D MOT, while still providing some cooling along the longitudinal direction. In order to provide this cooling, the push beam is also retr-reflected, with the help of a specially machined differential pumping tube (on the right in fig. 19). The differential pumping tube is machined to have a 45° angled polished end, reflecting all of the light except for the central part towards a retro-reflecting mirror outside the cell. Along the other 2D-MOT cooling direction (up and down in fig. 19), this whole set of optics is replicated, with the exception of the push beam retro-reflection.

The current 2D-MOT setup is pictured in Figure 20. The vacuum system has been assembled and successfully pumped down, with a octagonal test chamber in place of the main experimental chamber. This test chamber is intended to be used

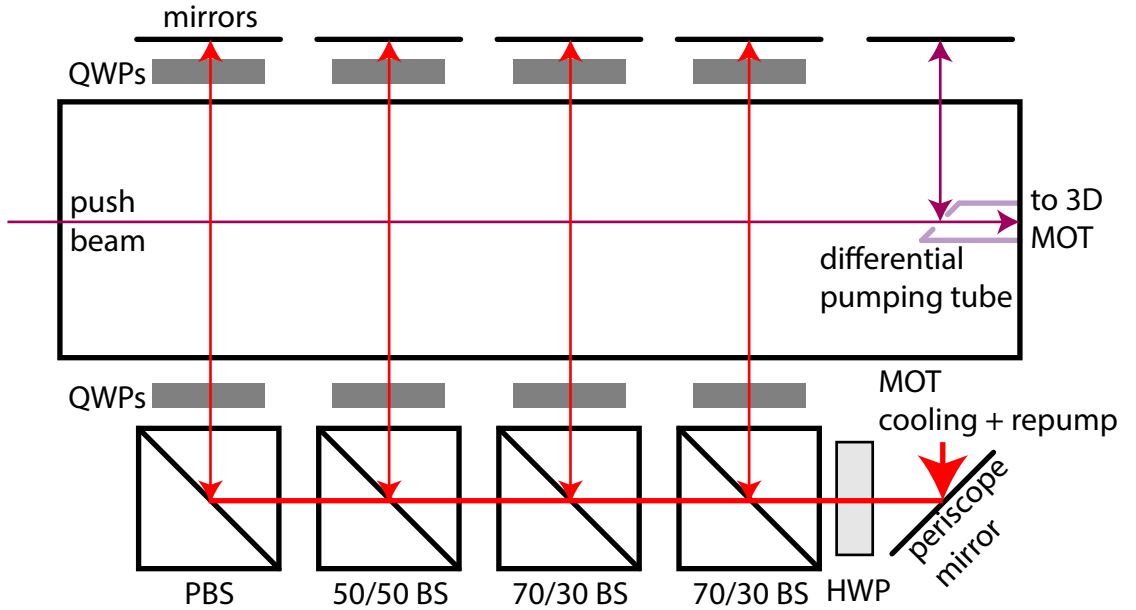


Figure 19: Schematic of 2D MOT optics along one direction. The main cooling and repump beam is split into four parallel arms by four beam splitter cubes. The push beam enters from the oven direction and is retro-reflected via a custom machined and polished differential pumping tube. These optics are mounted on crosses attached to the 2D MOT cell.

to send probe light through and detect fluorescence to characterize the atomic beam coming out of the 2D MOT. The optics have been assembled and the quarter-wave plates lightly epoxied onto the BS cubes and mirrors, although as can be seen in the picture some have regrettably fallen off. Quadropole coils have been wound around each of the four windows, onto 3D printed coil winding forms. BiasZ coils have also been wound to cancel out stray gradients along the atomic beam direction.

The two Toptica TA-pro systems that were used to provide all ^{40}K light in the past are still operational, and need to be re-purposed to provide both 2D MOT and 3D MOT cooling and repump light. A new Toptica TA-pro was also purchased, with the intent to implement gray molasses cooling on the ^{40}K D1 line as described in [37].

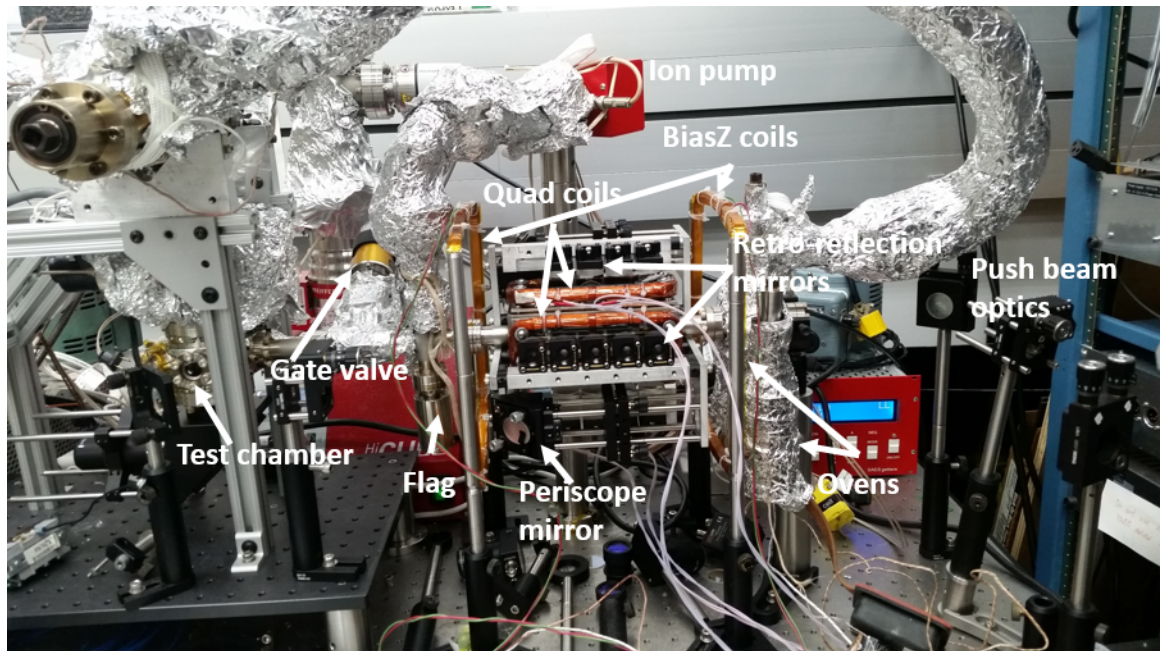


Figure 20: Picture of current 2D MOT apparatus. The vacuum system is in place, optics are (mostly) mounted and coils to generate the quadrupole trap and cancel gradients along the atomic beam direction have been wound.

Appendix 3: Absorption Imaging with Recoil Induced Detuning

In this Chapter, we describe the simulations we performed in order to interpret absorption images in a non-standard regime: at long imaging times, where the recoil induced detuning needed to be taken into account. This simulation was necessary to interpret data collected for our s-wave scattering experiment, described in Chapter ???. In this Chapter, we first describe the recoil-induced detuning effect and derive the equations to be solved. Then, we attempt to solve these equations perturbatively, and show that this treatment is insufficient in the regime of interest. We then perform two versions of the numerical simulations: one where the atoms are assumed to remain stationary relative to each other during imaging, and one where they are free to move. We show that although the atoms do move significantly during the imaging time, this does not have a strong effect on the final observed intensity. Finally, we use our simulated results to calibrate the saturation intensity in our camera units, and find the parameters for optimal signal-to-noise (SNR) ratio imaging. This work was previously reproted in [38].

3.1 Recoil-induced detuning

After absorbing a number of photons N , an atom will obtain a recoil velocity of Nv_r . Via the Doppler effect, this will result in a detuning $\delta = Nk_r v_r$. This detuning will increase as more atoms are absorbed, and therefore depend on time, making the absorbed intensity also time dependent. We can generalize Eq. 1.26 to

include a time dependence on the detuning term and therefore also the intensity:

$$\frac{d}{dz} \frac{I(z, t)}{I_{\text{sat}}} = -\rho(z)\sigma_0 \frac{I(z, t)/I_{\text{sat}}}{1 + 4\delta(z, t)^2/\Gamma^2 + I(z, t)/I_{\text{sat}}}. \quad (3.1)$$

The number of photons absorbed per atom will depend on the intensity lost, up until the current time, at that location. The detuning will therefore be proportional to the total number of photons lost up until time t at that location, proportional to the absorbed intensity divided by the single photon energy $\hbar\omega_L$, divided by the number of atoms that participated in the absorption $\rho(z)$ times the detuning $k_r v_r$:

$$\delta(t, z) = \frac{k_r v_r}{\hbar\omega_L \rho(z)} \int_0^t \frac{dI(z, \tau)}{dz} d\tau. \quad (3.2)$$

These equations are interdependent, and cannot be in general solved analytically.

Figure 1a shows the velocity and detuning as a function of position in space for three different imaging times, calculated numerically. All calculations in this chapter were done for a cloud of ^{40}K atoms, as that is relevant to our experiment described in the next chapter. The resonant wavelength is $\lambda_L = 770.11$ nm, the natural linewidth of the transition is $\Gamma = 6.035$ MHz, the resulting saturation intensity and recoil velocity are $I_{\text{sat}} = 17.5$ W/m² and $v_r = 0.01297$ m/s.

3.2 Perturbative treatment

We can treat these equations perturbatively in time. To first order, we can set the detuning in Eq. 3.1 to $\delta = 0$, assume $I(z)$ is time independent, and plug that into Eq. 3.2 to obtain

$$\delta(t, z) = \frac{k_r v_r}{\hbar\omega_L \rho(z)} \int_0^t -\rho(z)\sigma_0 \frac{I(z)}{1 + I(z)/I_{\text{sat}}} d\tau \quad (3.3)$$

$$= \frac{k_r v_r \sigma_0}{\hbar\omega_L} \frac{I(z)}{1 + I/I_{\text{sat}}} t. \quad (3.4)$$

This can then be recursively plugged into Eq. 3.1 to obtain

$$\frac{d}{dz} \frac{I(z, t)}{I_{\text{sat}}} = -\rho(z) \sigma_0 \frac{I(z, t)/I_{\text{sat}}}{1 + 4 \left(\frac{k_r v_r \sigma_0}{\hbar \omega_L \Gamma} \frac{I(z)}{1+I/I_{\text{sat}}} \right)^2 t^2 + I(z, t)/I_{\text{sat}}}. \quad (3.5)$$

Integrating both sides of the above equation, we obtain a perturbative equation to second order in time [39]:

$$\sigma_0 n = \ln(I_0/I_f) + \frac{I_0 - I_f}{I_{\text{sat}}} + \frac{(k_r v_r t)^2}{3} \left(\frac{I_{\text{sat}}}{I_f + I_{\text{sat}}} - \frac{I_{\text{sat}}}{I_0 + I_{\text{sat}}} + \ln \left(\frac{I_f + I_{\text{sat}}}{I_0 + I_{\text{sat}}} \right) \right). \quad (3.6)$$

In Fig. 1b, we examine for what imaging times the above perturbative equation, as well as the model that completely ignores recoil induced detuning, is valid. We do this by performing numerical simulations to extract a value for the final intensity I_f and using Eq. 1.27 and Eq. 3.6 to extract values $\sigma_0 n$ that would be deduced from experiment. We find that within the recoil time, both analytic expressions start to differ from the true atomic column density by over 5%, and the perturbative model of Eq. 3.6 quickly diverges thereafter.

In the following sections, we describe two versions of numerical simulations that we have performed in order to appropriately extract atomic column densities from experimental data.

3.3 Stationary atom model

In order to numerically simulate the imaging process, we assume a Gaussian distribution of atoms along the propagation direction, $\rho(z) = n/\sqrt{2\pi w e^{(-z^2/2w^2)}}$. The dependence of the result on the choice of cloud width w is discussed in the next chapter. We divide the cloud into small bins along z . For the initial version of the simulation, the atoms were assumed to stay within the same bins for the entire duration of the imaging pulse, i.e. the cloud shape remained constant. We

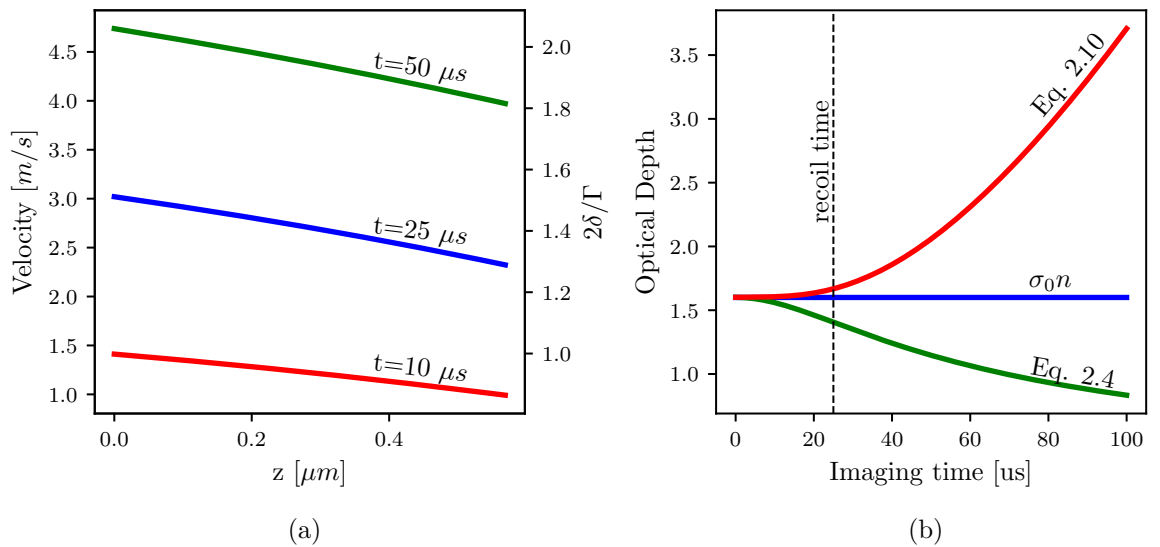


Figure 1: (a) Dependence of velocity and detuning on position simulated for ^{40}K at three different imaging times and a probe intensity $I_0 = 0.8I_{\text{sat}}$. (b) Column densities deduced from optical depths obtained from recoil detuning corrected simulation of on-resonant imaging of ^{40}K atoms at probe intensity $I_0 = 0.8I_{\text{sat}}$. The blue line is the input column density $\sigma_0 n = 1.6$. The green line is the high probe intensity corrected column density given by Eq. (1.27). The red line is the column density as expanded to second order in time, Eq. (3.6).

then used Eqs. 3.1-3.2 to numerically propagate the probe intensity and detuning as a function of both time and space. The algorithm used is detailed by Alg. 1.

Algorithm 1 Stationary atom model

```

 $I[n = 0, t] = I_0$  { $n$  is the bin index,  $t$  is the time index,  $I$  is in units of  $I_{\text{sat}}$ }
```

 $\delta[n, t = 0] = 0$ {light initially resonant, δ in units of $\Gamma/2$ }
 $H_f = 0$ {Radiant fluence seen by camera after passing through cloud}
for $t = 0$ to t_f **do** {loop over time steps}
 for $n = 1$ to N **do** {loop over bins, N is total bin number}
 $A = \sigma_0 \rho[n] dz$ { dz is the size of spatial step}
 $B = v_r dt / (\hbar c \rho[n])$ { dt is the size of the time step}
 $I[n, t] = I[n - 1, t] - AI[n - 1, t] / (1 + \delta[n, t - 1]^2) + I[n - 1, t]$ {Eq. (3.1)}
 $\delta[n, t] = \delta[n, t - 1] + B(I[n - 1, t] - I[n, t])$ {Eq. (3.2)}
end for
 $H_f = H_f + I[N, t] dt$ {collecting total fluence seen by the camera}
end for
 $OD^{\text{sim}1} = -\ln(H_f / I_0 t_f)$

We call the optical depth obtained in this way $OD^{\text{sim}1}$, to distinguish if from the simulated optical depth via the method described in the next section.

The validity of this model can be checked by considering limits where the equations are analytically solvable. For short imaging times, the recoil-induced detuning should not contribute to the optical depth, and therefore Eq. 1.27 should become exact. This is seen in Fig. 2a, where the imaging pulse is only 3 μs long and the simulated optical depth (blue dots) agrees with that given by Eq. 1.27 for all intensity regimes.

Even at longer imaging times, the problem can be analytically solved for limits of both high and low intensity compared to the saturation intensity. At intensities $I \gg I_{\text{sat}}$, even far detuned atoms will scatter light at their maximum, and we can assume $\delta^2/\Gamma^2 \ll I/I_{\text{sat}}$, reducing back to Eq. 1.27. At extremely low intensities, atoms will scatter very little light and the detuning $\delta^2/\Gamma^2 \ll 1$, again reducing back to Eq. 1.27. As seen in Fig. 2 b,c the simulation agrees with the analytic Eq. 1.27 in the limit of both high and low intensities. But, as the imaging time increases, the disagreement due to recoil induced detuning grows.

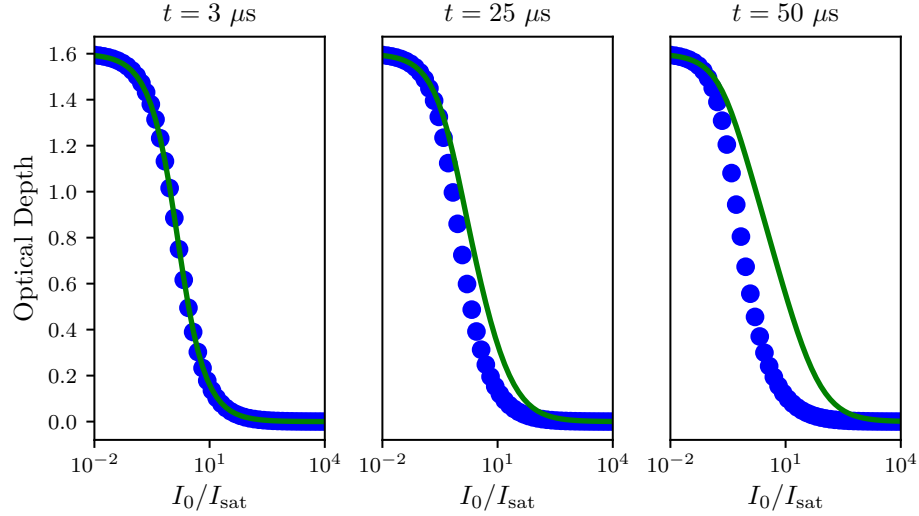


Figure 2: Optical depth as a function of probe intensity as predicted by the simulation (blue symbols) and by Eq. (1.27) (green curves), for three different imaging times. As expected, the predictions agree in both the high and low intensity limits, and differ for probe intensities comparable to the saturation intensity and longer imaging times.

The simulation allows us to extract both the intensity and the detuning as a function of both time and position. We can use this information to infer the velocity and therefore the displacement of the atoms during the imaging pulse, and check if our assumption that the atoms stay in their original 'bins' during the image pulse is valid. Figure 3a shows the position, deduced by integrating the recoil-induced velocity, as a function of time of the first, middle, and last spatial 'bin' for a probe intensity slightly above saturation, $I = 1.2I_{\text{sat}}$. As seen in the figure, not only do the atoms move beyond their 'bins', but also at long imaging times the first atoms (which have absorbed the most light) overtake the last ones. Therefore, the atomic cloud does not maintain shape during the imaging pulse, and our initial assumption is invalid.

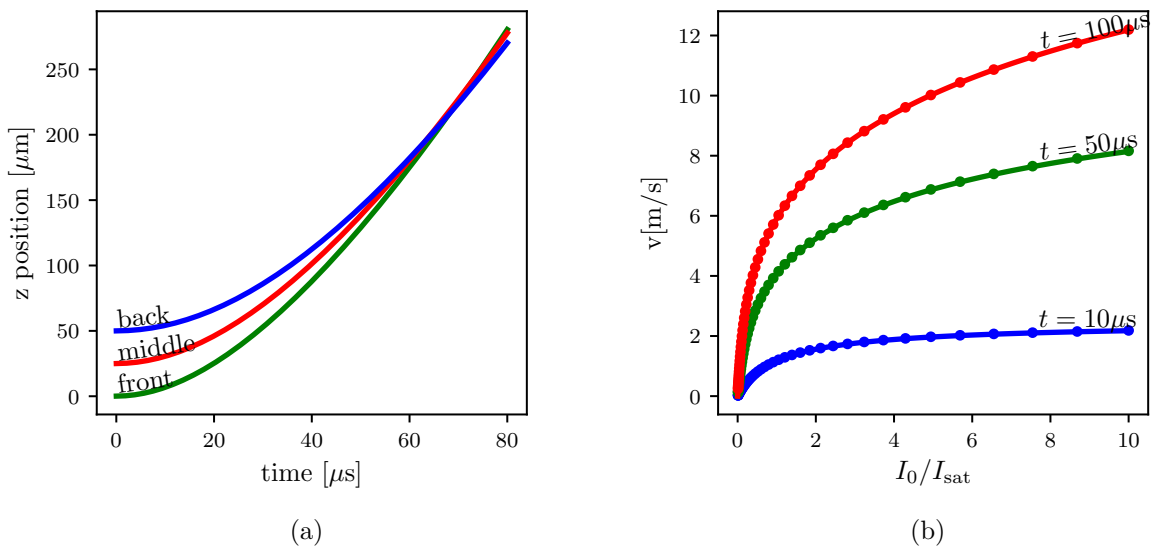


Figure 3: (a) Position of atoms as a function of imaging time for atoms in the first (solid green), middle (dashed red), and last (dotted blue) bins of the simulated density distribution for an initial cloud $50 \mu\text{m}$ in extent. The probe intensity used in this calculation was $1.2 I_{\text{sat}}$, and the column density was $\sigma_0 n = 1.6$. (b) The velocity of a single composite atom as a function of probe intensity for various imaging times. Simulation data (dots) and numerical solutions of Eq. (3.7) (lines) are in agreement.

3.4 Traveling atom model

To model the recoil-induced detuning effect during the imaging pulse taking into account the potentially significant spatial displacement of the atoms, we performed a second version of our simulation. In this version, we clumped some number of atoms N_{ca} into a single composite atom, and then tracked the detuning, velocity and position of each composite atom as a function of imaging time. Tacking individual atoms would be computationally inaccessible for reasonable cloud sizes. The algorithm used is given by Alg. 2.

Algorithm 2 Travelling atom model

```

 $z[n] = z_0, \delta[n] = 0$  {initialize position and detuning for each composite atom,
labeled by index  $n$ }
 $O[i] = n$  {make a list of composite atom indexes, ordered by position}
 $I[n = 0, t] = I_0$  {  $t$  is the time index,  $I$  is in units of  $I_{sat}$ }
 $H_f = 0$  {Radiant fluence seen by camera after passing through cloud}
for  $t = 0$  to  $t_f$  do {loop over time steps}
    for  $i = 1$  to  $N$  do {loop over superatoms}
         $n = O[i]$  {apply probe intensity to composite atoms in order of appearance}
         $A = \sigma_0 N_{sa} dz$  {dz is length over which atoms were grouped into single composite atom}
         $B = v_r dt / (\hbar c N_{sa})$  {dt is the time step}
         $I[n, t] = I[n - 1, t] - AI[n - 1, t] / (1 + \delta[n]^2 + I[n - 1, t])$  {Eq. (3.1)}
         $\delta[n] += B(I[n - 1, t] - I[n, t])$  {Eq. (3.2), detuning in units of  $\Gamma/2$ }
         $z[n] += dt \Gamma \delta / 2k$  { $k$  is the wavenumber,  $\Gamma \delta / 2k$  is the velocity at  $\delta$  detuning}
    end for
     $O[i] = \text{sort}(n, \text{key} = z[n])$  {sort composite atom indexes by current position}
     $H_f H_f + I[N, t] dt$  {collecting total fluence seen by the camera}
end for
 $OD^{\text{sim2}} = -\ln(H_f / I_0 t_f)$ 

```

To check the validity of this version of the simulation, we check the velocity of a composite atom as a function of time in an analytically solvable limit. In this case, we take the limit of a single composite atom, such that the intensity seen by the composite atom becomes time independent. This simplifies Eqs. 3.1 and 3.2 to only carry time dependence in the detuning term, and we can then plug Eq. 3.1

into Eq. 3.2 and differentiate both sides with respect to time to obtain

$$\frac{d\delta(t)}{dt} = \frac{\Gamma k_r v_r}{2} \frac{I/I_{\text{sat}}}{1 + 4\delta^2/\Gamma^2 + I/I_{\text{sat}}}. \quad (3.7)$$

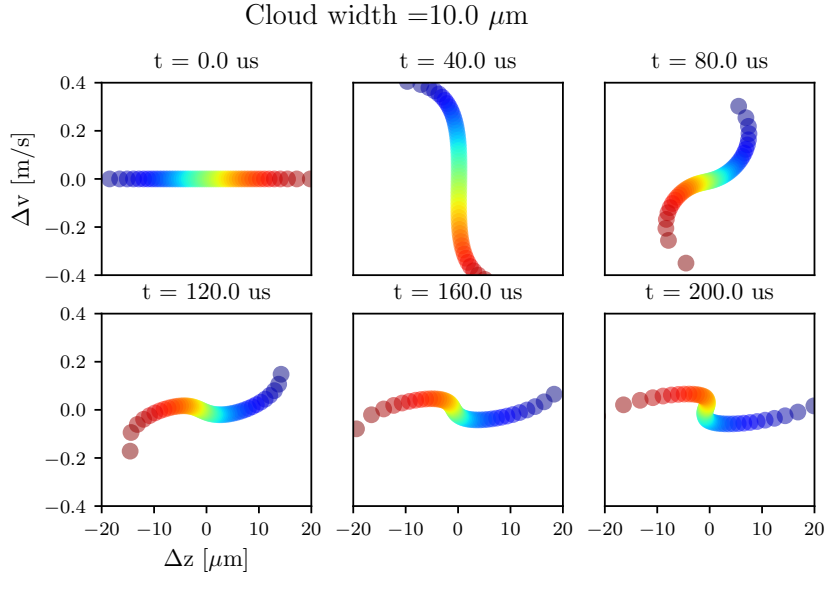
Equation (3.7) can be solved numerically, and is in agreement with our simulation, as seen in Fig. 3(b).

We then used this version of the simulation to look at the motion of composite atoms as a function of imaging time in phase space (ie, velocity and position). Some examples of this motion can be seen in Fig. 4. As seen in the figure, the atomic cloud is significantly distorted during the imaging pulse and the atoms perform some crazy acrobatics.

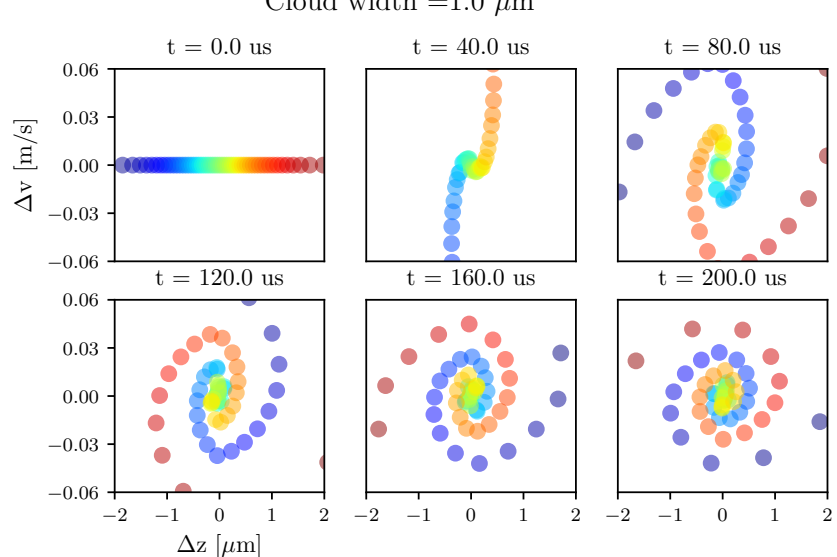
It remains to check how the atoms' acrobatics affect the resulting optical depth, ie the attenuation of the probe beam. To do this, we compare the optical depths generated by our stationary atom model, OD^{sim1} , and by our travelling atom model, OD^{sim2} . The results of this comparison are seen in Fig. 5(a). As seen from the figure, the optical depths predicted by the two versions of the simulation are negligibly small - $|OD^{\text{sim1}} - OD^{\text{sim2}}| / OD^{\text{sim1}} \leq 0.005$. We also checked the effect of having different initial distributions of atoms in space by varying the initial function $\rho(z)$ and keeping the total atom number constant. We found the effect of this to be negligible as well. Therefore, to infer atomic column densities from observed optical depths, it is sufficient to use the stationary atom model.

3.5 Calibration of saturation intensity

Saturation intensity is an intrinsic property of the atom, so the idea of calibrating it may be confusing. However, there are several experimental parameters that may influence exactly what value of I_{sat} is appropriate to use in Eq. 3.1 and 3.2, such as losses in the imaging system and polarization of the probe beam. In



(a)



(b)

Figure 4: Phase space evolution of an atomic cloud exposed to probe light with intensity $\tilde{I}_0 = 1.2$. We defined $\Delta v = v - \langle v(t) \rangle$ and $\Delta z = z - \langle z(t) \rangle$, subtracting out the center of mass position and velocity of the cloud. The column density $\sigma_0 n$ is 1.6, and the initial cloud is a Gaussian with a width of $10 \mu\text{m}$ in (a) and $1 \mu\text{m}$ in (b). The center of mass velocities $\langle v \rangle$ are $(0, 3.41, 5.26, 6.52, 7.50, 8.32)$ m/s sequentially, and are the same for both initial cloud widths.

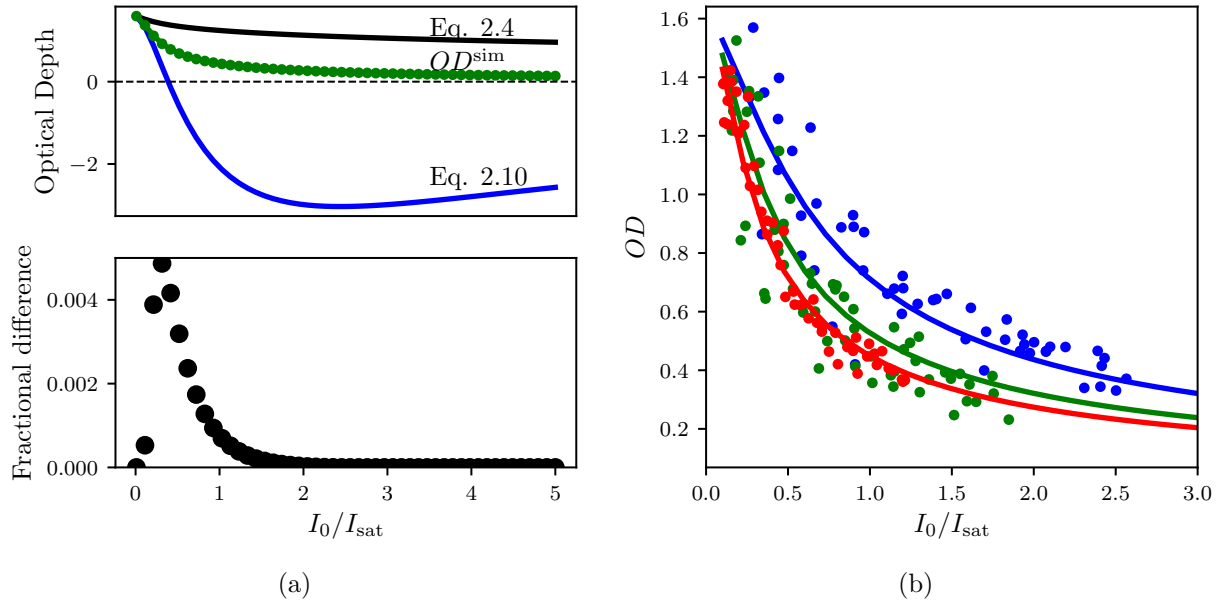


Figure 5: (a) Top. Optical depth as a function of probe intensity for an imaging time $t = 100 \mu\text{s}$. $OD^{(1)}$ and $OD^{(2)}$ are optical depths predicted from a given column density by Eq. (1.27) and (3.6) respectively. The two versions of simulated optical depth, $OD^{\text{sim}1}$ (green curve) and $OD^{\text{sim}2}$ (green dots) are plotted. Bottom. The fractional difference between two versions of the simulated OD , $|OD^{\text{sim}1} - OD^{\text{sim}2}| / OD^{\text{sim}1}$. (b) The optical depth as a function of probe intensity for three imaging times: $t = 40 \mu\text{s}$ (cyan), $t = 75 \mu\text{s}$ (magenta), $t = 100 \mu\text{s}$ (red). The dots represent experimental data and the lines represent the best fit of simulated data. The optimal fit parameters pictured are a $\sigma_0 n$ of 1.627(5) and saturation intensity of 29(7) counts/ μs .

addition, we have no direct experimental access to the total radiant fluence (time integral of intensity) seen by the camera. Instead, the light hitting the charge-coupled device (CCD) camera triggers some number of photoelectrons to be registered. The proportionality between the number of photons hitting the camera and the number of photoelectrons it triggers is called the quantum efficiency q_e of the camera. The number of these photoelectrons, after some electronic gain and noise introduced during the readout process, is then read out as a number of 'counts' registered on each pixel. The camera-dependent factors influencing how the number of counts depends on the number of incoming photons can be convolved with the experimental factors of probe polarization and optical loss into a single calibration of the effective saturation intensity in units of 'counts' output by the camera per unit time.

To calibrate this effective I_{sat} in camera counts per unit time, we absorption imaged our cloud of ^{40}K atoms for a range of probe intensities for three different values of imaging time: $40 \mu\text{s}$, $100 \mu\text{s}$, and $200 \mu\text{s}$. We select a small region in the center of the cloud, where we can assume the atomic column density $\sigma_0 n$, and the initial probe intensity I_0 to be roughly constant. We then average the values of I_0 and I_f over this region and plot the final intensity I_f as a function of I_0 . We then used the optical depth predicted by our simulation OD^{sim} and used that to simultaneously fit the three curves with I_{sat} and $\sigma_0 n$ as fit parameters, as shown in Fig. 5(b). As can be seen from the figure, this procedure not only allows us to read off I_{sat} in units of camera counts per μs , but also shows that our simulation accurately reproduces the differences in OD dependence on imaging time.

3.6 SNR optimization

Using the simulations described in the previous sections, we can create a lookup table of atomic column densities as a function of initial and final probe intensities I_0 and I_f for any given imaging time. This lookup table can be then used to interpret

experimental data and obtain the atom number in regimes where the recoil-induced detuning is significant. This procedure can also be used to propagate photon shot noise into uncertainty in measured atom number.

We consider Poisson distributed photon shot noise, converting into shot noise on photoelectrons triggered inside the CCD. The standard deviation will then be proportional to $q_e \sqrt{N_p}$, where q_e is the quantum efficiency of the camera and N_p is the photon number. This uncertainty can be then propagated via the lookup table into uncertainty on the measured atomic column density $\delta_{\sigma_0 n}$. The signal-to-noise ratio (SNR) can then be expressed as $\sigma_0 n / \delta_{\sigma_0 n}$.

We study the SNR as a function of imaging time and initial probe intensity for a few different atomic column densities. Some representative data is shown in Fig. 6. As seen in Fig. 6(a), for a wide range of atomic column densities, extending the imaging time beyond 40 μs no longer yields significant improvements in SNR. There is, however, a factor of 1.5 improvement between using an imaging time of 10 μs , where the simple model given by Eq. 1.27 is appropriate, and 40 μs . Therefore, there are significant gains that can be made by going to longer imaging times and making use of the simulated lookup table.

This simulation allowed us to interpret experimental data. For a given imaging time, we created a look-up table of predicted optical depth as a function of probe intensity and atomic column density. We then found the observed optical depth on this table, with the given probe intensity, and inferred the atomic density. The uncertainty in the measured intensities can be propagated through this procedure, and we established optimal imaging parameters to maximize the SNR of this detection scheme. Figure 6(b) illustrates that the optimal initial probe intensity is different for different atom numbers. For low atom numbers, $\sigma_0 n \approx 0.1$, a probe intensity of $I_0 \approx 0.6 I_{\text{sat}}$ is best.

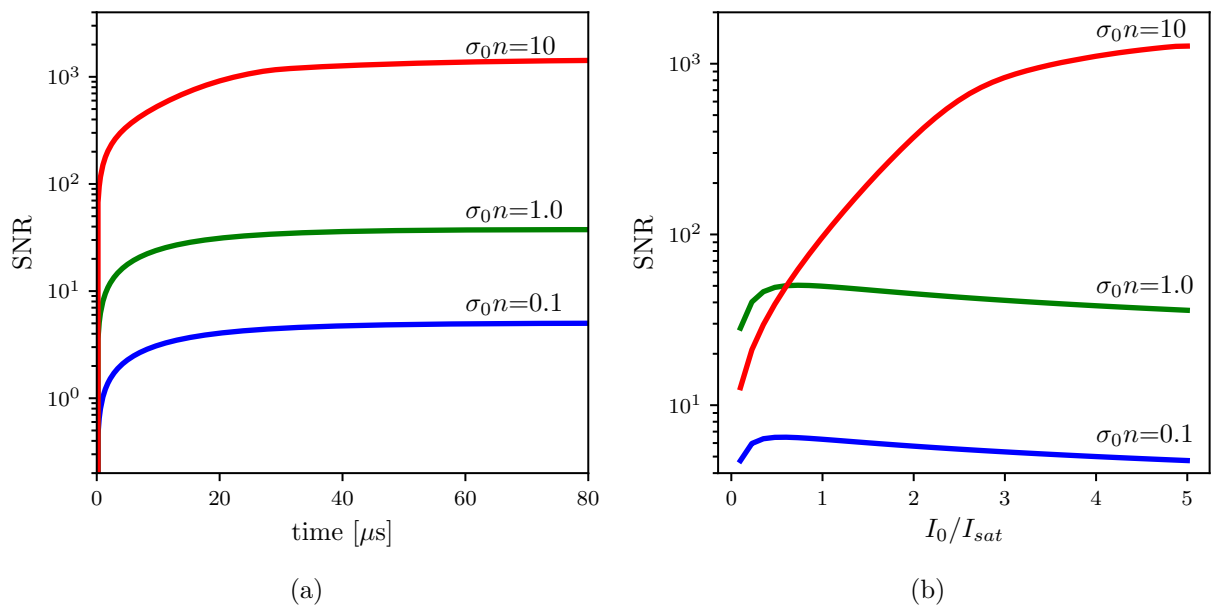


Figure 6: SNR for three different column densities after correcting for recoil induced detuning. (a) SNR as a function of imaging time for a probe intensity of $I_0 = 5.0I_{sat}$ and (b) SNR as a function of probe intensity for an imaging time of $50 \mu\text{s}$.

Appendix 4: Direct Imaging of Scattering Near a Feshbach Resonance

In this chapter, we describe our experiment directly imaging *s*-wave scattering halos of ${}^{40}\text{K}$ atoms in the vicinity of a Fesbach resonance between the $|F = 9/2, m_F = -9/2\rangle$ and $|F = 9/2, m_F = -7/2\rangle$ internal states. We used this data to extract the location of the magnetic fields resonance of $20.206(15)$ mT and a width of $1.0(5)$ mT, similar to the accepted values of $20.210(7)$ mT and $0.78(6)$ mT [23]. The data presented in this chapter was previously reported in [38].

We first introduced Feshbach resonances in section 2.2.2. Although Feshbach resonances are extremely useful for studying and manipulating Fermi gases, their resonant magnetic field values are difficult to predict analytically and are commonly computed via numerical models based on experimental input parameters [40–42] or determined experimentally [43, 44]. There have been a variety of experimental techniques used to characterize Feshbach resonances, including measuring atom loss due to three-body inelastic scattering, measurement of re-thermalization timescales, and anisotropic expansion of the cloud upon release from a confining potential, all of which infer the elastic scattering cross section from collective behavior of the cloud [45–47].

Here, we present an alternative technique, where we directly image the enhancement in elastic scattering due to the resonance. We collided pairs of ultra-cold Fermi gases and directly imaged the resulting *s*-wave scattered atoms as a function of magnetic field strength. This allowed us to observe the enhancement in scatter-

ing without relying on proxy effects. We measured the fraction of atoms scattered during the collision, and from this fraction deduced the resonant magnetic field and the width of the resonance.

In our dilute DFGs, even with the resonant enhancement of the scattering cross section, only a small fraction of the atoms scattered as the clouds passed through each other. This made direct detection of scattered atoms difficult due to detection uncertainty that disproportionately affected regions of low atomic density. To optimize the signal-to-noise ratio (SNR) for low atom numbers, we absorption imaged with fairly long, high-intensity pulses — a non-standard regime, where the atoms acquired a velocity during imaging and the resulting Doppler-shift was non-negligible. Simulation of the absorption imaging process was necessary for an accurate interpretation of these images, as described in Chapter 3. Using the simulation-corrected images, we extracted the fraction of atoms scattered in our collision experiment.

4.1 Experimental procedure

We prepared our degenerate ${}^{40}\text{K}$ clouds as described in section 2.3.5. After this preparation, we used adiabatic rapid passabe (ARP) to transfer the degenerate cloud of ${}^{40}\text{K}$ atoms in the $|F = 9/2, m_F = 9/2\rangle$ state into the $|F = 9/2, m_F = -9/2\rangle$ state by using a 3.3 MHz rf field and sweeping the bias magnetic field from -0.518 mT to -0.601 mT in 150 ms.

Following the state transfer, we had two versions of the protocol – one for approaching the Feshbach resonance from higher fields and one for approaching it from lower fields. For approaching the resonance from lower fields, we proceeded by ramping the bias magnetic field to 19.05 mT, turning on a 42.42 MHz RF field, and then sinusoidally modulating the bias field at 125 Hz for 0.5 s, with a 0.14 mT amplitude, decohering the ${}^{40}\text{K}$ state into an equal mixture of $|F = 9/2, m_F = -9/2\rangle$ and $|F = 9/2, m_F = -7/2\rangle$. For approaching the resonance from higher fields, the

same was done at a bias field of 21.71 mT and an RF frequency of 112.3 MHz. The depolarization allowed the ^{40}K atoms to interact and re-thermalize, allowing us to further evaporate in the dipole trap [48]. Since ^{87}Rb is heavier than ^{40}K , we were able to evaporate the ^{40}K atoms past the point where ^{87}Rb atoms were no longer suspended against gravity and had been completely removed. These hyperfine states of ^{40}K were then used to study their Feshbach resonance.

After evaporation, we ramped the bias field in a two-step fashion to the desired value B near the Feshbach resonance. We approached the field using our quad coils in Helmholtz configuration (0.19 mT/A, see sec. 2.3.2) to bring the magnetic field to a setpoint 0.59 mT away from B , $B - 0.59$ mT when approaching from below and $B + 0.59$ mT from above. We held the atoms at this field for 100 ms to allow the eddy currents induced by the large quad coils to settle, and then used our lower inductance biasZ coils (0.017 mT/A, see sec. 2.3.2) to quickly change the field the remaining 0.59 mT. This allowed us to study the resonance from both sides without the added losses associated with going through the resonance [16].

Once at the intended bias field, we split the cloud into two spatially overlapping components with opposing momenta and observed scattering as they moved through each other and separated. These counterpropagating components were created using an $8E_{\text{L}}$ deep near resonant ($\lambda_{\text{L}}=766.704$ nm) 1-d retro-reflected optical lattice (see sec. 2.3.1), where $E_{\text{L}} = \hbar^2 k_{\text{L}}^2 / 2m_{\text{K}}$ is the lattice recoil energy and $\hbar k_{\text{L}} = 2\pi\hbar/\lambda$ is the recoil momentum. We rapidly pulsed this lattice on and off with a double-pulse protocol [49, 50]. The pulse sequence was optimized to transfer most of the atoms into the $\pm 2\hbar k_{\text{L}}$ momentum states. Since the initial Fermi gas had a wide momentum spread (in contrast to a BEC, which has a very narrow momentum spread), and the lattice pulsing is a momentum dependent process [49], not all the atoms were transferred into the target momentum states. We experimentally optimized our pulse times to minimize the atoms remaining in the zero momentum

state. The optimized pulse times were $23\ \mu\text{s}$ for the first pulse, $13\ \mu\text{s}$ off interval, and $12\ \mu\text{s}$ for the second pulse [50].

We then released the atoms from the trap and allowed 1 ms for the two opposite momentum states within the cloud to pass through each other, scattering on the way. For the data taken coming from below the Feshbach resonance, we then simply ramped down the field and imaged the atoms. For the data taken coming from above the Feshbach resonance, we ramped the field back up, retreating through the resonance if it had been crossed and thereby dissociating any molecules that were created, and then quickly ramped the field back down and imaged the atoms. We used a $40\ \mu\text{s}$ imaging pulse with $I_0/I_{\text{sat}} \approx 0.6$ at the center of the probe laser. The total time-of-flight was $t_{TOF} = 6.8\ \text{ms}$.

The magnetic fields produced by the combination of our quad and biasZ coils in the regime of interest were independently calibrated by rf-spectroscopy. We prepared ^{40}K atoms in the $|F = 9/2, m_F = -9/2\rangle$ state and illuminated them with an rf-field with some frequency ν_{rf} . We then ramped our high-inductance coils to variable set points, followed by an adiabatic $250\mu\text{s}$ ramp of $2.84\ \text{mT}$ in the lower inductance coils. We then used Stern-Gerlach and observed the fractional population in the $|F = 9/2, m_F = -9/2\rangle$ and $|F = 9/2, m_F = -7/2\rangle$ states as a function of the high-inductance coil current. We fit the fractional population curve to a Gaussian, and considered the center of the fit to be on-resonant, with an uncertainty given by the Gaussian width. We used the Breit-Rabi formula [ADD CITATION TO THIS ONCE ITS PUT INTO THE HYPERFINE SECTION OF ATOM LIGHT CHAPTER] to determine the resonant field value at ν_{rf} . We did this for 5 different rf frequencies, and acquired a field calibration with an uncertainty of $0.3\ \text{mT}$, which was included in the listed uncertainty on the center field of the Feshbach resonance.

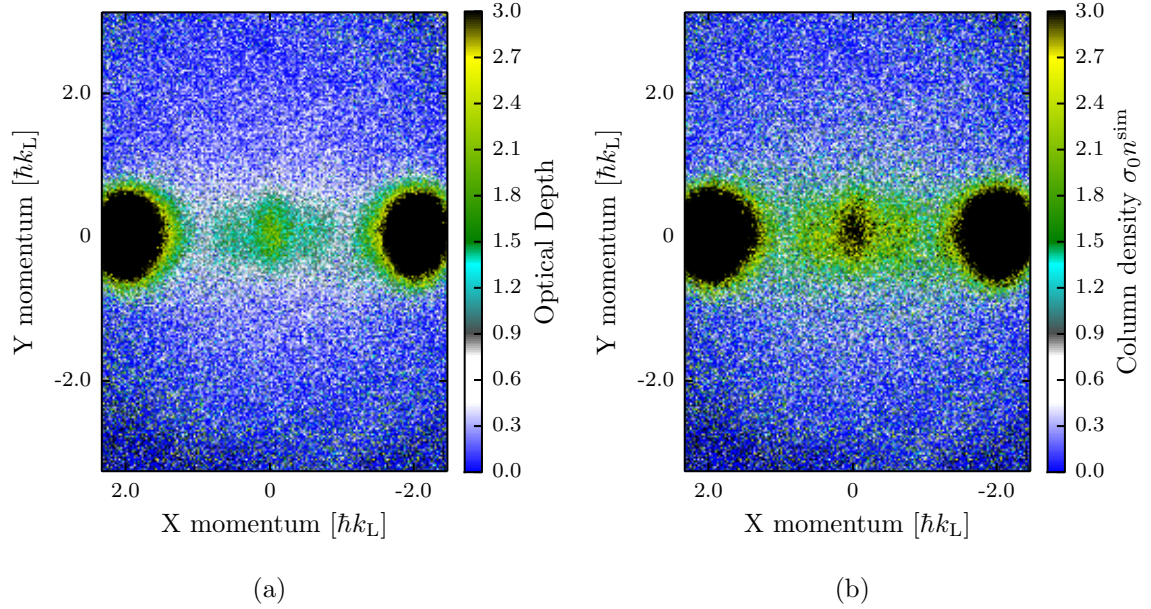


Figure 1: An example of our absorption image after 6.8 ms TOF. The 1-D lattice imparts momentum along e_x . The two large clouds on the left and right are the atoms in the $\pm 2k_L$ momentum orders that passed through each other unscattered. The smaller cloud in the center is the atoms that remained in the lowest band of the lattice after pulsing, and thus obtained no momentum. The thin spread of atoms around these clouds is the atoms that underwent scattering. This image was taken coming from below the Feshbach resonance at 20.07 mT. (a) Raw optical depth, (b) atomic column density obtained by comparing to simulated ODs , $\sigma_0 n^{\text{sim}}$

4.2 Data analysis

We first processed each image by comparing the observed ODs to simulations taking into account the recoil induced detuning as described in Chapter 3. An example of images before and after processing are shown in Fig. 1. To improve the signal and mitigate our shot to shot number fluctuations, we took 15 nominally identical images for each data point.

We counted the fraction of atoms that experienced a single scattering event for each of the fifteen images at a given bias magnetic field. Single scattering events are easily identified, as two atoms that scatter elastically keep the same amplitude of momentum, but depart along an arbitrary direction. Therefore, an atom traveling

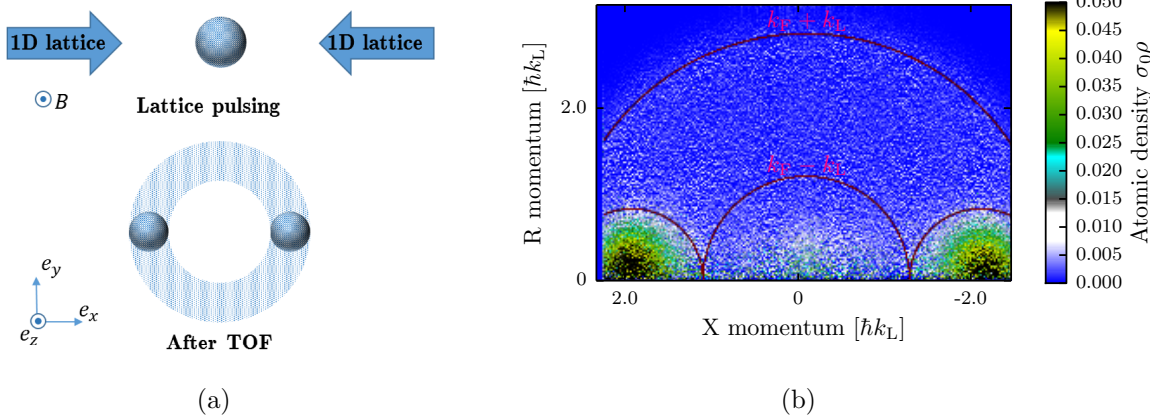


Figure 2: (a) Our experimental setup. After time-of-flight, the two clouds traveling along $\pm \hat{e}_x$ directions have separated and the atoms that underwent a single scattering event were evenly distributed in a scattering halo around the unscattered clouds. The 1-D lattice defined the axis of cylindrical symmetry. (b) Inverse Abel transformed image. The atoms within the Fermi momentum k_F of each unscattered cloud center are in the unscattered region and counted towards the total unscattered number. The atoms outside the radius $k_L - k_F$ but inside $k_L + k_F$ while also being outside the unscattered region are counted towards the number of single scattered atoms.

at $2\hbar k_L$ to the right that collides elastically with an atom traveling at $-2\hbar k_L$ to the left will depart with equal and opposite momenta $2\hbar k_L$ at an arbitrary angle, and in a time-of-flight image such atoms will lie in a spherical shell, producing the scattering halo pictured in Fig. 2(a).

Absorption images captured the integrated column density along e_z , a projected 2D atomic distribution. To extract the radial dependence of the 3D distribution from the 2D image, we performed a standard inverse Abel transform. The inverse Abel transform assumes cylindrical symmetry, which was present in our case, with the axis of symmetry along e_x , defined by the lattice. We neglect the initial asymmetry of the trap, as during time-of-flight the atoms travel far beyond the initial extent of the cloud ($r_x, r_y, r_z \approx (45, 48, 15)$ μm , while the cloud width after TOF is $\approx 82 \mu\text{m}$ in each direction. We thus obtained the atomic distribution $\rho(r, \theta)$ as a function of r , the radial distance from the scattering center, and θ , the angle

between r and symmetry axis e_x , integrated over ϕ , the azimuthal angle around the x axis.

We then extracted the number of scattered atoms N_{scat} as a fraction of the total atom number N_{tot} for each image, as shown in Fig. 2(b). The unscattered atom number was the number of atoms in the two unscattered clouds. The number of atoms that underwent a single scattering event was the number of atoms outside the Fermi radius of the unscattered clouds, but inside the arc created by rotating the Fermi momentum k_F around the original center of the cloud (red arcs in Fig. 2(b)). For both the scattered and unscattered numbers, we accounted for atoms that fell outside the field of view of our camera by multiplying the counted atom number by a factor of the total area as defined by the radii divided by the visible area on the camera. The atoms in the center region were not counted as they were originally in the zero momentum state and could not contribute to the scattering halo under study.

We fit the fraction of scattered atoms versus the total atom number for each of the 15 images taken at the same bias magnetic field to a line constrained to be zero at zero. The slope of this fit was taken to be the value of $N_{\text{scat}}/N_{\text{tot}}^2$ at that bias magnetic field, and the variance of the fit gave the uncertainty on that data point. This uncertainty reflected our shot to shot number fluctuations, which produced variable atomic densities and thus influence the scattered fraction.

We then deduced the resonant field value B_0 and width of the resonance Δ , the parameters in Eq. (2.26). Since we were in the low energy regime (the atomic momentum was much smaller than the momentum set by the van der Waals length $k_L + k_F \ll 1/l_{\text{vdW}}$, and we were well below the p-wave threshold temperature [48]), the scattering cross-section was given by $\sigma = 4\pi a^2$.

The scattering cross-section σ gives the probability $P_{\text{scat}} = \sigma N/A$ that a single particle will scatter when incident on a cloud of atoms with a surface density of

N/A , where A is the cross-sectional area of the cloud and N is the number of atoms in the cloud. In our case, each half of the initial cloud, with atoms number $N_{\text{tot}}/2$, is incident on the other half. Thus, the number of expected scattering events is $N_{\text{scat}} = (N_{\text{tot}}/2)\sigma(N_{\text{tot}}/2) = \sigma N_{\text{tot}}^2/4A$. Assuming A is constant for all our data, we can define a fit parameter $b_0 = 4\pi a_{\text{bg}}^2/4A$, where a_{bg} is the background scattering length. We can thus adapt Eq. (2.26) to obtain the fit function

$$\frac{N_{\text{scat}}}{N_{\text{tot}}^2} = b_0 \left(1 - \frac{\Delta}{B - B_0}\right)^2 + C. \quad (4.1)$$

We found that our imaging noise skewed towards the positive, giving rise to a small background offset. We accounted for this in our fit by including a constant offset parameter C .

4.3 Results

Our final data is presented in Fig. 3. The red curve depicts a best fit of the model given in Eq. (4.1). The fit parameters we extracted were $\Delta = 1(5)$ mT, $B_0 = 20.206(15)$ mT, $b_0 = 5(3) \times 10^{-3}$ and $C = 8(1) \times 10^{-4}$. To obtain the fit, we used data taken by approaching the resonance from above for points above where we expected the resonance to be and data taken approaching the resonance from below for points below. We also excluded from the fit data points very near the resonance, as there the assumption $\sigma\rho \ll 1$, where ρ is the atom number per unit area, is no longer valid and the problem must be treated hydrodynamically.

The accepted values for the ${}^{40}\text{K}$ s-wave Feshbach resonance for the $|9/2, -9/2\rangle$ and $|9/2, -7/2\rangle$ states are $B_0 = 20.210(7)$ mT and $\Delta = 0.78(6)$ mT [23], which is in good agreement with our findings. Some potential sources of systematic uncertainty that we did not account for include scattering with atoms that did not receive a momentum kick from the lattice pulsing or the impact of multiple scattering events.

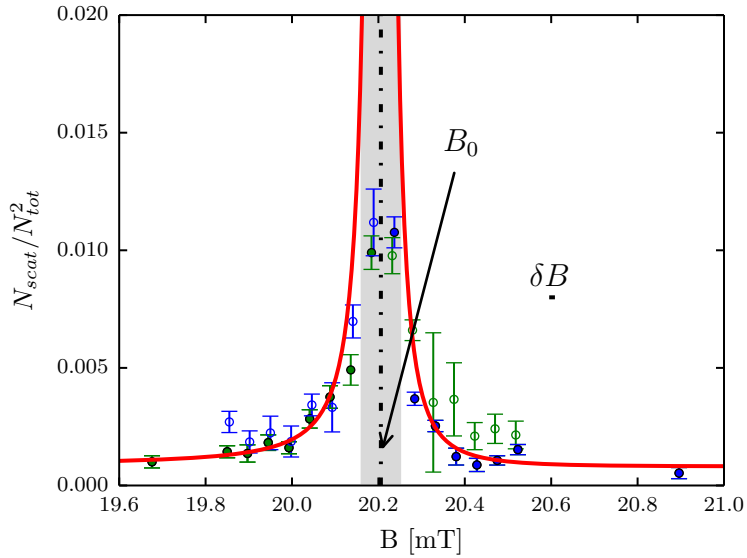


Figure 3: Normalized scattered population plotted versus bias field B . Green dots represent data taken coming from below the resonance, and blue dots represent the data taken coming from above the resonance. The red curve depicts the best fit, where data coming from above the resonance was used above the resonance and data coming from below the resonance was used below the resonance to create the fit; the unused data points are indicated by hollow dots. The regime where the scattering length is likely large enough for the atoms to behave hydrodynamically is shaded in gray, and data points in that area were also excluded from the fit. Resonant field value B_0 as found in this work and our systematic uncertainty in the bias magnetic field δB_0 are indicated.

Appendix 5: Synthetic Magnetic Fields in Synthetic Dimensions

In condensed matter, 2-D systems in high fields have proved to be of great technological use and scientific interest. The integer quantum Hall effect (IQHE) [51], with it's quantized Hall resistance, had given rise to an ultra-precise standard for resistivity. It was also one of the first examples of topology playing an important role in physics—the precise quantization of the Hall conductance is guaranteed by the non-trivial topology of the system [1]. This quantizes the magnetic flux into flux quanta of $\Phi_0 = 2\pi\hbar/e$, where e is the electron charge, and leads to a new 'plateau' in the resistivity when an additional quantum of flux is threaded through the system.

In the IQHE system, the underlying lattice structure of metal is effectively washed out—the magnetic flux per individual lattice plaquette is negligible. However, new physics arises when the magnetic flux per plaquette is increased to some non-negligible fractionj of the flux quantum, giving rise to the Hofstadter butterfly [52]. These regimes are har to reach experientally, since the typical plaquette size in crystalline material is of order a square angstrum, and the magnetic field necessary to thread create a magnetic flux of Φ_0 through such a narrow area is of order $\approx 10^4$ Tesla, not accessable with current technology.

Several platforms have, however, reached the Hofstadter regime by engineering systems with large effective plaquette size, in engineered materials [53, 54], and in atomic [55–60] and optical [61] settings. Here, we use the approach of synthetic dimensions [62] to reach the Hofstadter regime. We demonstrate the non-trivial topology of the system created, and use it to image skipping orbits at the edge of

the 2-D system—a hallmark of 2-D electron systems in a semiclassical treatment.

The work described in this chapter was published in [63].

5.1 Synthetic dimensions setup

Any internal degree of freedom can be thought of as a synthetic dimension—the different internal states can be treated as sites along this synthetic direction. As long as there is some sense of distance along this direction, i.e. some of the internal states are ‘nearest neighbors’ while others are not, this is a meaningful treatment. In our case an effective 2-D lattice is formed by sites formed by a 1-D optical lattice along a ‘real’ direction, here \mathbf{e}_x , and the atom’s spin states forming sites along a ‘synthetic’ direction, \mathbf{e}_s .

The experimental setup for this system is schematically represented in 1a. The BEC is subject to a 1-D optical lattice, formed by a retro-reflected beam of $\lambda_L = 1064\text{nm}$ along \mathbf{e}_x . A bias magnetic field B_0 along \mathbf{e}_z separates the different spin states. The spin states can be thought of as sites along a synthetic dimension even without any coupling field. However, only once a coupling field is present do they acquire a sense of distance. We couple them via rf or Raman coupling, which only couples adjacent spin states. The Raman beams illuminating the atoms are along the same \mathbf{e}_x direction as the 1-D optical lattice. The rf field has components both along the \mathbf{e}_x and \mathbf{e}_y .

Figure 1b sketches out the effective 2-D lattice created. Here, we have labelled the lattice sites along the ‘real’ direction \mathbf{e}_x by site index j . In the tight binding approximation, we can describe a lattice hopping between adjacent sites with tunneling amplitude t_x . Similarly, the sites along the ‘synthetic’ dimension are labelled by site index m (identical to spin projection quantum number m_F), and the rf or Raman coupling here plays the role of a tunneling amplitude t_s . In the case of rf coupling, there is no momentum kick associated with spin exchange, and both t_x

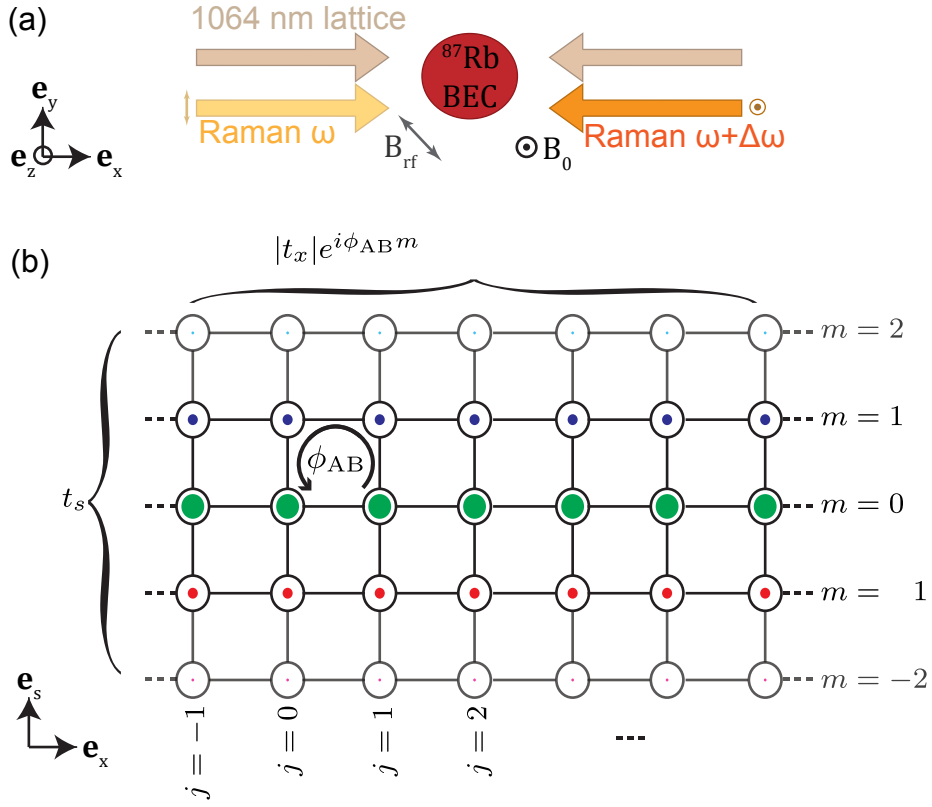


Figure 1: Setup of effective 2-D lattice. (a) Beam geometry. The BEC is subject to a bias magnetic field B_0 in the \mathbf{e}_z direction. The 1-D lattice beam and Raman beams are both along the \mathbf{e}_x direction, and the rf field can be applied with projections onto both the \mathbf{e}_x and \mathbf{e}_y . (b) Schematic of the effective 2-D lattice. Sites along \mathbf{e}_x are formed by the 1-D optical lattice and labelled by site number j . Sites along the synthetic direction \mathbf{e}_s are formed by the spin states: 3 sites for atoms in the $F = 1$ manifold and 5 sites for atoms in $F = 2$. These sites are labelled by m . Raman transitions induce a phase shift, which can be gauge transformed into a tunneling phase along the \mathbf{e}_x direction. This leads to a net phase when hopping around a single lattice plaquette of ϕ_{AB} .

and t_s are real.

In the case of Raman coupling, however, there is a momentum kick of $2k_R$ associated with every spin transfer, and therefore a phase factor of $\exp(2ik_Rx)$ with every spin 'tunneling' event. Since position x is set by the 1-D lattice, $x_j = j\lambda_L/2 = j\pi/k_L$, and the space dependent phase factor is $\exp(2\pi ik_R/k_L j)$. An absolute phase change in the wavefunction is not meaningful. However, a phase acquired when going around a plaquette and coming back to the same place is meaningful, as one could imagine one atom staying at the same site and the other going around a plaquette and coming back to detect the phase difference. In this setup, the phases acquired while going around a single plaquette are, starting at some lattice site $|j, m\rangle$, are: 0 (for tunneling right to $|j + 1, m\rangle$), $2\pi ik_R/k_L(j + 1)$ (for tunneling up to $|j + 1, m + 1\rangle$), 0 (for tunneling left to $|j, m + 1\rangle$) and $-2\pi ik_R/k_L j$ (for tunneling back down to $|j, m\rangle$). The total phase acquired is thus $\phi_{AB} = 2\pi k_R/k_L$, independent of the starting lattice site. Since the absolute phase does not matter and only the value of $t \phi_{AB}$, we can perform a phase transformation that shifts the tunneling phase onto the spatial direction, defining $t_x = |t_x| \exp(i\phi_{AB}m)$ and $t_s = |t_s|$, as labelled in Figure 1b.

To see how this phase implies an effective magnetic field, we draw an analogy to the Aharonov-Bohm effect [64, 65] from quantum mechanics. In this effect, consider an infinite solenoid with an electric current running through it. The magnetic field B in this setup exists only inside the solenoid, while the magnetic vector potential persists outside the solenoid. However, if two electrons are sent on a trajectory around the solenoid, even though they never pass through any magnetic field, they nevertheless acquire a relative phase that can be detected by interfering them with each other. This relative phase is given by $\phi_{AB} = 2\pi\Phi/\Phi_0$, where $\Phi = B * A$ is the magnetic flux through the solenoid (A is the area pierced by the magnetic field) and $\Phi_0 = h/e$ is the flux quantum, with e the electron charge. Since in our system,

the atoms acquire a phase when they perform a closed loop around a single lattice plaquette. Therefore, they behave as though there was an infinite solenoid piercing each plaquette with a magnetic field going through it, and the flux per plaquette in units of the flux quantum is $\Phi/\Phi_0 = \phi_{AB}/2\pi = k_R/k_L$. For the case of rf coupling, the phase acquired at every transition is 0 and the fluxss $\Phi/\Phi_0 = 0$.

5.2 Hamiltonian of the effective 2-D system

5.2.1 Hamiltonian

The full Hamiltonian of this system, without making the tight binding approximation, can be written down by combining the lattice Hamiltonian (eqn. 1.34) and the rf (eqn. 1.44) or Raman Hamiltonian (eqn. 1.47). To do this, we write a new basis that encompasses both the momentum and the spin degrees of freedom. For the lattice Hamiltonian, we used the momentum basis

$$\begin{pmatrix} \vdots \\ |q + 4k_L\rangle \\ |q + 2k_L\rangle \\ |q\rangle \\ |q - 2k_L\rangle \\ |q - 4k_L\rangle \\ \vdots \end{pmatrix}. \quad (5.1)$$

For the Raman Hamiltonian in the $F = 1$ manifold, we used the spin and momentum basis

$$\begin{pmatrix} |k_x - 2k_R, -1\rangle \\ |k_x, 0\rangle \\ |k_x + 2k_R, 1\rangle \end{pmatrix}. \quad (5.2)$$

In a lattice, the momentum k_x becomes crystal momentum q . For every state in the lattice basis, we now expand to three states, one for each spin state, with the appropriate momentum shifts. We obtain

$$\left(\begin{array}{c} \vdots \\ |q + 2k_L - 2k_R, -1\rangle \\ |q + 2k_L, 0\rangle \\ |q + 2k_L + 2k_R, 1\rangle \\ |q - 2k_R, -1\rangle \\ |q, 0\rangle \\ |q + 2k_R, 1\rangle \\ |q - 2k_L - 2k_R, -1\rangle \\ |q - 2k_L, 0\rangle \\ |q - 2k_L + 2k_R, 1\rangle \\ \vdots \end{array} \right) . \quad (5.3)$$

In this basis, we combine the lattice and Raman Hamiltonians (ommitting the kinetic energy in the other two directions) in an infinite block matrix form as

$$H = \left(\begin{array}{ccc} \ddots & & \\ & \mathbf{H}_R(2k_L) & \frac{\mathbf{v}_0}{4} & \mathbf{0} \\ & \frac{\mathbf{v}_0}{4} & \mathbf{H}_R(0) & \frac{\mathbf{v}_0}{4} \\ & \mathbf{0} & \frac{\mathbf{v}_0}{4} & \mathbf{H}_R(-2k_L) \\ & & & \ddots \end{array} \right) , \quad (5.4)$$

where $\mathbf{H}_R(x)$ is the Raman Hamiltonian with a momentum shift of x :

$$\mathbf{H}_R(n2k_L) = \begin{pmatrix} \frac{\hbar^2(q+n2k_L-2k_R)^2}{2m} + \hbar\delta & \hbar\Omega/2 & 0 \\ \hbar\Omega/2 & \frac{\hbar^2(q+n2k_L)^2}{2m} - \hbar\epsilon & \hbar\Omega/2 \\ 0 & \hbar\Omega/2 & \frac{\hbar^2(q+n2k_L+2k_R)^2}{2m} - \hbar\delta \end{pmatrix}, \quad (5.5)$$

the matrix $\frac{\mathbf{V}_0}{4}$ is a 3x3 diagonal matrix lattice coupling strength $\frac{\mathbf{V}_0}{4}$ on the diagonal, and $\mathbf{0}$ is a 3x3 matrix of zeros. This extends in both directions with $\mathbf{H}_R(2nk_L)$ on the diagonal blocks and $\frac{\mathbf{V}_0}{4}$ as the first off-diagonal blocks and $\mathbf{0}$ everywhere else.

This Hamiltonian is easily extended to higher F values by replacing the Raman blocks $\mathbf{H}_R(x)$ with the corresponding Raman coupling Hamiltonian from eqn. 1.48, and extending the diagonal matrix $\frac{\mathbf{V}_0}{4}$ and the zero matrix $\mathbf{0}$ to be $(2F+1)\times(2F+1)$.

For computational convenience, we convert to lattice recoil units, $E_L = \hbar^2 k_L^2 / 2m$, $k_L = 2\pi/\lambda_L$. Then the diagonal blocks become

$$\mathbf{H}_R(n)/E_L = \begin{pmatrix} (q + n - \phi_{AB}/2\pi)^2 + \hbar\delta & \hbar\Omega/2 & 0 \\ \hbar\Omega/2 & (q + n)^2 - \hbar\epsilon & \hbar\Omega/2 \\ 0 & \hbar\Omega/2 & (q + n + \phi_{AB}/2\pi)^2 - \hbar\delta \end{pmatrix}, \quad (5.6)$$

where $\hbar\delta$, $\hbar\Omega$ and $\hbar\epsilon$ are now written in units of E_L , q is written in units of k_L and we have used the fact that $\phi_{AB}/2\pi = k_R/k_L$. The off-diagonal blocks $\frac{\mathbf{V}_0}{4}$ will be the same 3x3 diagonal matrices, with $\frac{\mathbf{V}_0}{4}$ in units of E_L .

This Hamiltonian can be written for general values of F in the presence of Raman coupling and a 1-D optical lattice as

$$H = \sum_{m=-F, n=-\infty}^{F, \infty} H_0 + H_R + H_L,$$

where the diagonal term

$$H_0 = (\hbar^2 (q - 2m\Phi/\Phi_0 - 2n)^2 k_L^2 / 2m + \hbar\delta m + \hbar\epsilon m^2) |q + n2k_L, m\rangle \langle q + n2k_L, m|$$

includes the kinetic energy as well as the two-photon Raman detuning from resonance δ and the quadratic Zeeman shift ϵ . The second term represents the Raman coupling with coupling strength $\hbar\Omega$, with anisotropic tunneling arising from the spin-dependent prefactor (Clebsch-Gordan coefficient):

$$H_R = \hbar\Omega\sqrt{F(F+1) - m(m+1)} / 2\sqrt{2} |q + n2k_L, m\rangle \langle q + n2k_L, m+1| + \text{H.c.}$$

Here, H.c. stands for Hermitian conjugate. The third term represents lattice coupling to higher order lattice states, with lattice depth V_0 :

$$H_L = V_0/4 |q + n2k_L, m\rangle \langle q + (n+1)2k_L, m| + \text{H.c.}$$

5.2.2 Band structure

The band structure of this Hamiltonian is presented in Figure 2. Here, we have restricted ourselves to the lowest lattice band. We can do this because the energy splitting between the lowest and second lowest lattice band is of order $4E_L$ (see Figure 5), while the width of the lowest band, given by the amplitude of the approximate sinusoid, is of order $0.3E_L$ for our range of lattice depths, around $5.0E_L$. As long as the Raman coupling stays small compared to the lattice band spacing,

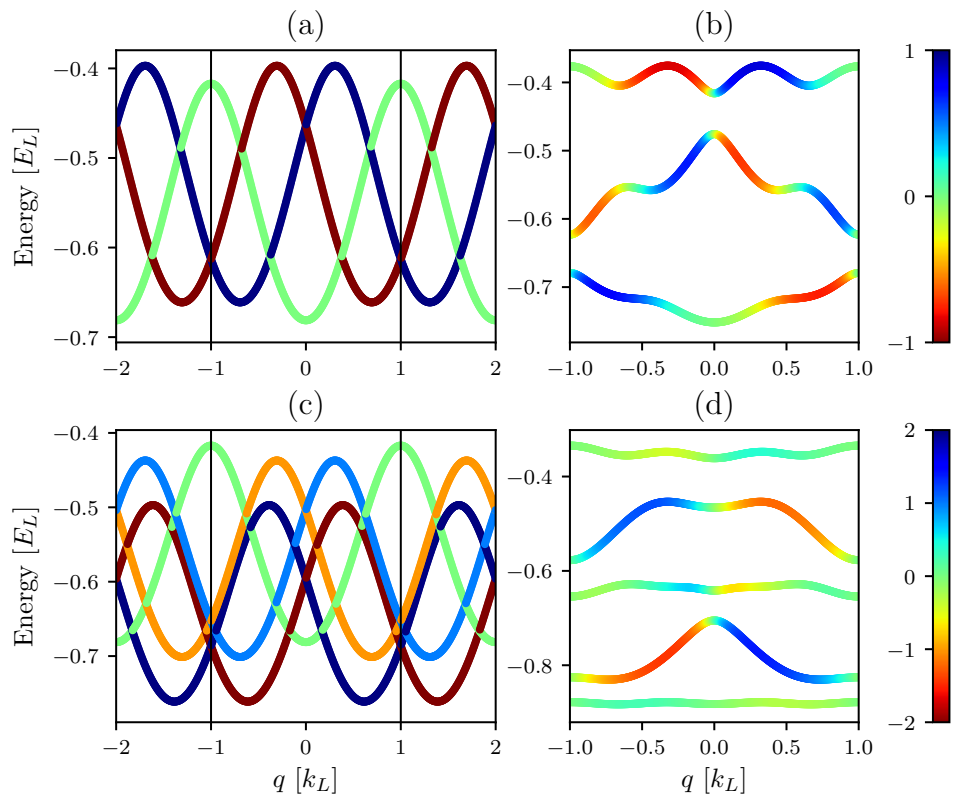


Figure 2: Band structure of the synthetic dimensions Hamiltonian, eqn. 5.4. For all panels, the detuning $\hbar\delta = 0$ and the quadratic shift $\hbar\epsilon = 0.02E_L$. (a) $F = 1$, $\hbar\Omega = 0.0$. (b) $F = 1$, $\hbar\Omega = 0.5$. (c) $F = 2$, $\hbar\Omega = 0.0$. (d) $F = 2$, $\hbar\Omega = 0.5$.

the higher lattice bands are energetically separated enough that they can be ignored.

Therefore, we can think of the Raman coupling analogously to the free space Raman coupling (see section 1.6.2), except instead of free space parabolas each spin state gets a lowest lattice band sinusoid. Figure 2a shows this in the limit of no Raman coupling, $\Omega = 0$, but with the lattice on at $V_0 = 4.0E_L$. The quadratic Zeeman shift is $\hbar\epsilon = 0.02E_L$ and the detuning $\delta = 0$. The $m_F = -1$ sinusoid is shifted $2k_R$, similarly to section 1.6.2, but since the sinusoid is periodic with $2k_L$, it folds into the first Brillouin zone of the lattice, such that the nearest minimum to $q = 0$ is at $q = 2k_R - 2k_L = (2\phi_{AB}/2\pi - 2)k_L$. The edges of the Brillouin zone are marked by horizontal lines. The color indicates magnetization $\langle m \rangle = \sum_{m_F} m_F * n_{m_F}$, where n_{m_F} is the fractional population in the m_F state. In synthetic dimensions language, $\langle m \rangle$ is the expectation value of position along \mathbf{e}_s .

In Figure 2b, we have restricted ourselves to the first Brillouin zone and turned on the Raman coupling to $\hbar\Omega = 0.5E_L$. The crossings of the bands in Figure 2a become avoided crossings, and the lowest band now has a spin dependence on crystal momentum. Figure 2c-d shows the same progression for the $F = 2$ manifold. Figure 2c is taken in the limit of $\hbar\Omega = 0.0$. All of the 5 spin states get 'folded' back into the first Brillouin zone due to the lattice periodicity of the bands. The different heights of the sinusoids are due to the quadratic Zeeman shift $\hbar\epsilon = 0.02E_L$. The lattice depth is again $V_0 = 5.0E_L$ and detuning $\hbar\delta = 0$. In Figure 2d we have restricted ourselves to the first Brillouin zone and turned on the Raman coupling to $\hbar\Omega = 0.5E_L$. Note that the inverted hyperfine structure in 2c (meaning that the quadratic shift pushed the $m_F = 0$ state up rather than down in energy compared to the others), combined with the Raman coupling serves to make the lowest band in the $F = 2$ manifold close to flat.

5.2.3 Calibration

To calibrate the lattice depth V_0 in the synthetic dimensions system, we can simply calibrate the lattice depth without Raman or rf coupling as described in Section 1.5.3. However, we are operating at very low Raman coupling strengths, $\hbar\Omega \approx 0.5E_L$. This is necessary because in the synthetic dimensional system the Raman coupling plays the role of tunneling, which has to be small to approximate the tight binding limit. At these low Raman couplings, simple pulsing as described in Section 1.6.3, as the contrast of the Rabi oscillations would be too low to resolve. Therefore, we calibrate the Raman coupling and detuning with the full synthetic dimensions system, where the 'folding in' effect of the lattice makes the higher Raman bands much closer energetically than without the lattice, leading to larger contrast and allowing for accurate calibration.

To do this, we must first adiabatically load the lowest 1-D lattice band. To do that, we must ramp on the lattice potential on a time scale slow compared to the band spacing, $\approx 4E_L$. This gives $t \approx \hbar/4E_L = 0.12$ ms. Figure 3a shows the full ramping scheme. We ramp the lattice on in ≈ 20 ms. Then, we must pulse on the Raman coupling on a time scale fast compared to the spin sub-band level spacing to produce Rabi oscillations, but still adiabatic with respect to the lattice spacing to avoid exciting to the higher lattice band. We ramp the Raman beams on in $300\ \mu\text{s}$. Then, the system is held on for a variable amount of time before all light is snapped off and the atoms are allowed to expand in time-of-flight. For the case of $F = 2$ atoms, the transfer to the $F = 2$ manifold is done in the 1-D lattice before the Raman beams are ramped on to minimize the time spend in the $F = 2$ manifold.

Figure 3c,d shows sample time-of-flight images during the calibration procedure for $F = 1$ and $F = 2$ respectively. The vertical axis is \mathbf{e}_x , aligned with the

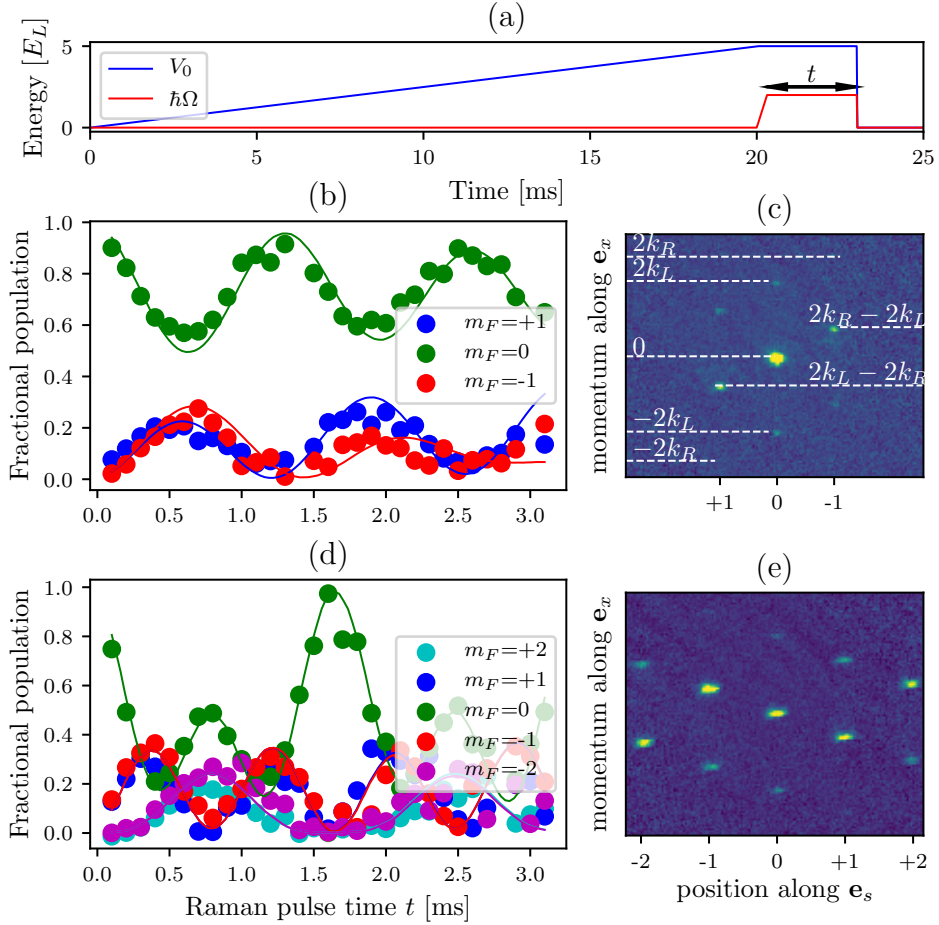


Figure 3: Calibration of synthetic dimensions lattice. (a) Ramping procedure. The blue line represents the 1-D lattice depth as a function of time and the red line represents Raman coupling as a function of time. Both are held on for a variable amount of time t , producing Rabi oscillations. (b) Example of fractional populations in different m states as a function of time t in the $F = 1$ manifold. Dots indicate data and lines indicate the best fit to theory, with parameters $\hbar\Omega = 0.56 \pm 0.01 E_L$ and $\hbar\delta = 0.029 \pm 0.002 E_L$. (c) Example time-of-flight image in the $F = 1$ manifold. A Stern-Gerlach gradient pulse separates different m states along the horizontal axis, while the lattice and Raman beams give momentum along the vertical axis. (d) Example of fractional populations in different m states as a function of time t in the $F = 2$ manifold. Dots indicate data and lines indicate the best fit to theory, with parameters $\hbar\Omega = 0.61 \pm 0.002 E_L$ and $\hbar\delta = 0.002 \pm 0.001 E_L$. (e) Example time-of-flight image in the $F = 2$ manifold. A Stern-Gerlach gradient pulse separates different m states along the horizontal axis, while the lattice and Raman beams give momentum along the vertical axis.

lattice and Raman beams. Since the atoms have expanded in time-of-flight, this axis corresponds to the momentum k_x . The horizontal axis of the image is the axis along which a Stern-Gerlach magnetic field gradient, separating the different spin states, is applied. Therefore, this axis is the position m along the synthetic dimension \mathbf{e}_s . In the effectively 2-D synthetic dimensions lattice language, this is a 'hybrid' imaging technique—imaging momentum along one lattice direction and position along the other.

Figure 3c labels some notable momentum orders. The central order is at $k_x = 0$, where the atoms start before the experiment. Two higher lattice orders, at $k_x = \pm 2k_L$, are populated for the same spin $m = 0$. $k_x = \pm 2k_R$ is labelled, but not visibly populated, to indicate where the orders would appear if only Raman coupling was present with a higher coupling strength. Due to the 'folding in' effect of the lattice, the brightest orders of the $m = \pm 1$ states appear at $k_x = \pm(2k_L - 2k_R)$. The $F = 2$ states follow the same pattern, not labelled in Figure 3e as there are too many orders.

For each value of the time t we sum up the total optical depth in all of the orders of each spin state to obtain fractional populations for each spin state as a function of time. An example scan in the $F = 1$ manifold is shown in Figure 3 b. The colored dots represent the data for different spin states, and the lines represent the best fit to theory. Here, the significant detuning makes populations in the $m = \pm 1$ states unequal. An example scan in the $F = 2$ manifold is shown in Figure 3e. Here, the detuning is small and states with opposite spin oscillate in approximate unison.

5.2.4 Tight binding approximation

The synthetic dimensions Hamiltonian can be approximated in the tight binding limit as:

$$H = - \sum_{j,m} t_x e^{i\phi_{AB}m} |j+1, m\rangle \langle j, m| + t_s(m) |j, m+1\rangle \langle j, m| + A_m |j, m\rangle \langle j, m| + h.c., \quad (5.7)$$

where j and m label sites along \mathbf{e}_x and \mathbf{e}_s respectively, as shown in Figure 1b. $t_s = |t_s|$ and $t_x = |t_x| \exp(-i\phi_{AB}m)$ are the associated tunnelings. A_m captures the spin dependent diagonal elements, detuning $\hbar\delta$ and quadratic shift $\hbar\epsilon$. Here, we have implicitly restricted ourselves to the lowest 1-D lattice band, and assumed that tight binding, ie confinement at discrete lattice sites, is a good approximation (see 1.5.2). t_s is not a spin dependent quantity for $F = 1$ atoms, but is for $F = 2$, where differences in Clebsch-Gordan coefficients create non-uniform tunneling. In the limit of zero detuning and neglecting the quadratic shift as well as the t_s dependence on spin, this becomes the traditional Harper-Hofstadter Hamiltonian

$$H = - \sum_{j,m} t_x e^{i\phi_{AB}m} |j+1, m\rangle \langle j, m| + t_s |j, m+1\rangle \langle j, m| + h.c. \quad (5.8)$$

We can transform this Hamiltonian into momentum space along \mathbf{e}_x by plugging the Fourier transform formula

$$|j, m\rangle = \frac{1}{\sqrt{N}} \sum_{k_j} e^{-ik_j j} |k_j, m\rangle \quad (5.9)$$

into the above Hamiltonian to obtain

$$H = -\frac{1}{N} \sum_{k_j, m} t_m |k_j, m+1\rangle \langle k_j, m| + h.c. + 2t_x \cos(k_j - \phi_{AB}) |k_j, m\rangle \langle k_j, m| + A_m |k_j, m\rangle \langle k_j, m| \quad (5.10)$$

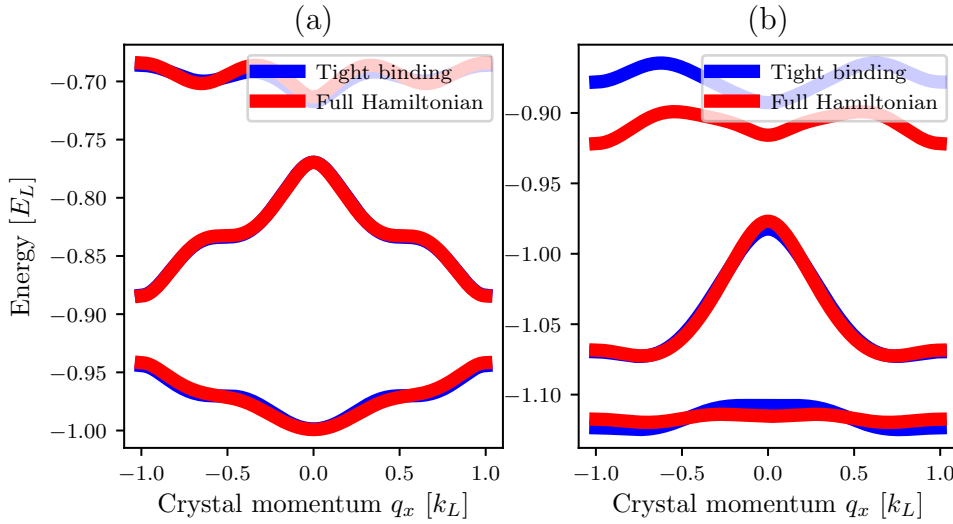


Figure 4: Band structure of the tight binding versus full Hamiltonian. $V_0 = 6.0E_L$, giving $t_x = 0.1E_L$, $\hbar\delta = 0$, $\hbar\epsilon = 0.02E_L$, $\hbar\Omega = 0.5E_L$. (a) $F = 1$, fitted value $t_s = 0.154E_L$. (b) $F = 2$, fitted value $t_s = 0.284$.

To go from the full Hamiltonian, eqn. 5.4, to the tight binding Hamiltonian we must find appropriate values for t_s and t_x . We find $|t_x|$ by treating the 1-D lattice independently, and matching the tight binding band to the lowest full lattice band. For most of the experiments described in the chapter, the lattice depth was $V_0 = 6E_L$, corresponding to $|t_x| \approx 0.01E_L$. To find the appropriate value of t_s , we fit the full synthetic dimensions band structure to the tight binding band structure eqn. 5.10 with t_s as a free parameter.

Figure 4 shows the overlayed band structure of the full Hamiltonian, eqn. 5.4, and the best fit tight binding band structure, eqn. 5.10. To fit, we minimize the square difference between the energies in the lowest two bands, relevant to our experiment.

5.3 Eigenstates of the synthetic 2-D lattice

After calibrating the synthetic dimensional lattice via pulsing, we can study the eigenstates of the lowest band of the system by adiabatically loading, i.e. ramping both the lattice and Raman or rf coupling on on a time scale slow compared to the magnetic band spacing. Along the synthetic direction, in the $F = 1$ manifold, there are no $m = \pm 2$ sites. This can be thought of as hard wall boundary conditions at the $m = \pm 2$ sites, confining the atoms in the allowed $m = 0, \pm 1$ sites. Therefore, we can consider the position eigenstates along the synthetic direction in relation to eigenstates of a square well potential.

Figure 5a shows a time-of-flight image of an adiabatically loaded synthetic dimensions lattice eigenstate with rf coupling along the synthetic direction. The vertical axis is single site resolved spin states m . The horizontal axis is momentum along the \mathbf{e}_x direction. Note that for each site m the distribution of momenta k_x is symmetric. Figure 5b shows the fractional population in each site m , summed over all momenta k_x . In the case of rf coupling, $\phi_{AB} = 0$ and the effective magnetic flux $\Phi_{AB}/\Phi_0 = 0$. Therefore, the fractional population along the spin direction looks simply like a discretized ground state probability distribution of the square well potential.

Figure 5c-h shows analogous data with Raman coupling along the synthetic direction. Figure 5d,g are the time-of-flight image and corresponding fractional populations of atoms adiabatically loaded from the $m_F = 0$ spin state, corresponding to the central minimum ($q = 0$) of the lowest band in Figure 2b. There are two key differences between this case and the rf case Figure 5a-b. First, the momenta of the different spin states are no longer symmetric, as explained in sec. 5.2.3. Second, the fractional populations in Figure 5g are no longer simply the discretized ground state probability distribution of the square well potential—it is a narrowed version

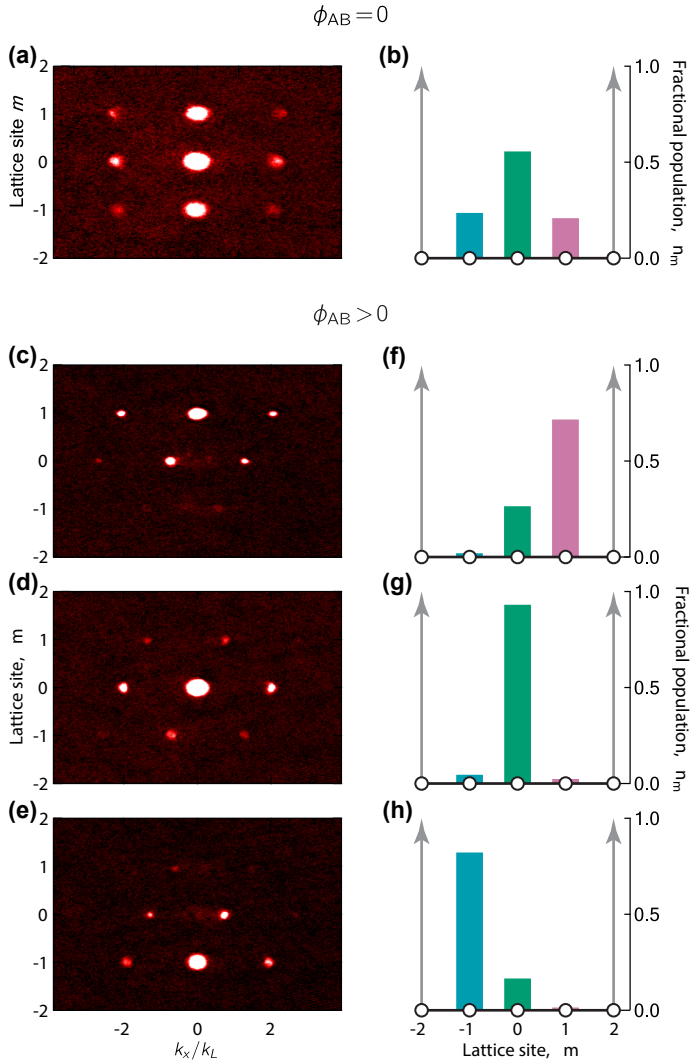


Figure 5: Eigenstates of the synthetic dimensions lattice. Left column: time-of-flight images, with position along \mathbf{e}_s on the vertical axis and momentum along \mathbf{e}_s on the horizontal. Right column: fractional populations in each site m . (a,b) Rf coupling, resulting in $\phi_{AB} = 0$. (c,f) Raman coupling, resulting in $\phi_{AB} > 0$, adiabatically loaded from the $m_F = 1$ state. (d,g) Raman coupling, resulting in $\phi_{AB} > 0$, adiabatically loaded from the $m_F = 0$ state. (e,h) Raman coupling, resulting in $\phi_{AB} > 0$, adiabatically loaded from the $m_F = -1$ state.

of it, more strongly concentrated in the $m = 0$ site.

This can be understood by analogy with a 2D electron system in a perpendicular magnetic field, confined in one dimension with hard walls. Along the confined direction, the wavefunction is localized to the scale of the magnetic length $l_B = \sqrt{\hbar/qB}$, with the center position at $k_x l_B^2$ in the bulk state, where $\hbar k_x$ is the electrons canonical momentum. In our system, the magnetic length $l_B = \sqrt{a^2\Phi_0/2\pi\Phi_{AB}}$, or in units of the lattice period a , $l_B^* = \sqrt{3/2\pi}$; this explains the narrowing of the bulk state in Figure 5g.

In the 2D electron system, at large $|k_x|$, the electron becomes localized near the edges, lifting the degeneracy of the otherwise macroscopically degenerate Landau levels. In our case, stable edge states appeared as the additional minima in Figure 2b, at $q \approx \pm 0.66k_L$. We loaded these edge states by starting in the $m_F = \pm 1$ states before adiabatically turning on the synthetic dimensions lattice to obtain eigenstates displayed in Figure 5c,f and Figure 5e,h respectively. These edge states predominantly occupy the edge sites in the synthetic direction, and are strongly confined there due to the narrow magnetic length. These localized edge states are the analog to the current-carrying edge states in fermionic integer quantum Hall effect systems [66].

5.4 Chiral edge currents

The same pulsing procedure that was used for calibration (sec. 5.2.3) can also be interpreted by analogy with the 2-D electron system. Figure 6a shows schematically what happens atoms are loaded from the $m = 0$ site into the lattice and tunneling along the synthetic dimension is pulsed on. Atoms begin analogues of cyclotron orbits, tunneling out into the edge $m = \pm 1$ sites and tunneling back to the bulk $m = 0$ state. The fractional populations in the three m sites as a function of time are shown in Figure 6b.

We performed this experiment for three different magnetic flux values: with rf coupling giving $\Phi_{AB}/\Phi_0 = 0$, with Raman coupling giving $\Phi_{AB}/\Phi_0 \approx 4/3$ and with inverted Raman coupling giving $\Phi_{AB}/\Phi_0 \approx -4/3$. The inverted Raman coupling was accomplished by switching the roles of the two Raman beams (see Figure ??a): the right going beam frequency was changed to $2\pi(\omega + \Delta\omega)$ and the left going beam frequency to $2\pi\omega$, resulting in the opposite recoil momentum for the same spin flip, flipping the direction of the effective magnetic field.

We define the current $I_{m=\pm 1} = n_m \langle v_m \rangle$, where n_m is the fractional population in site m and $\langle v_m \rangle$ is the expectation value of velocity along \mathbf{e}_x for atoms in sites m , as depicted in Figure 6a. The velocity is derived from the momentum measured in time-of-flight images. The chiral current of the system is then defined as $\mathcal{I} = I_1 - I_{-1}$. We calculate this chiral current for data in Figure 6b, with $\Phi_{AB}/\Phi_0 \approx 4/3$, displayed in red dots in Figure 6c. Atoms in the edge sites $m = \pm 1$ exhibit chiral motion, therefore the resulting chiral current is directly proportional to the fractional population in those sites and oscillates as a function of time in concert with the oscillation in Figure 6b. in Figure 6c also includes data for the $\Phi_{AB}/\Phi_0 \approx -4/3$ (solid black dots indicate data and solid black lines are from theory) and $\Phi_{AB}/\Phi_0 = 0$ (empty black dots). As seen in the figure, reversing the direction of the effective magnetic flux reverses the direction of the chiral currrent, and turning off the magnetic flux results in no net chiral current. The chiral current \mathcal{I} is normalized here by the tunneling velocity $2t_x/\hbar k_L$.

As the chiral current \mathcal{I} is proportional to the edge state population, we plot it as a function of the expectation value of the absolute value of m , $\langle |m| \rangle$, in Figure 6d. As expected, the chiral current is linear and positive for $\Phi_{AB}/\Phi_0 \approx 4/3$, negative for $\Phi_{AB}/\Phi_0 \approx -4/3$, and zero for $\Phi_{AB}/\Phi_0 = 0$. We call this slope \mathcal{S} . We then study the dependence of the chiral current on the strength of tunneling along the synthetic dimension, in units of the real axis tunneling t_s/t_x . We refer to this as

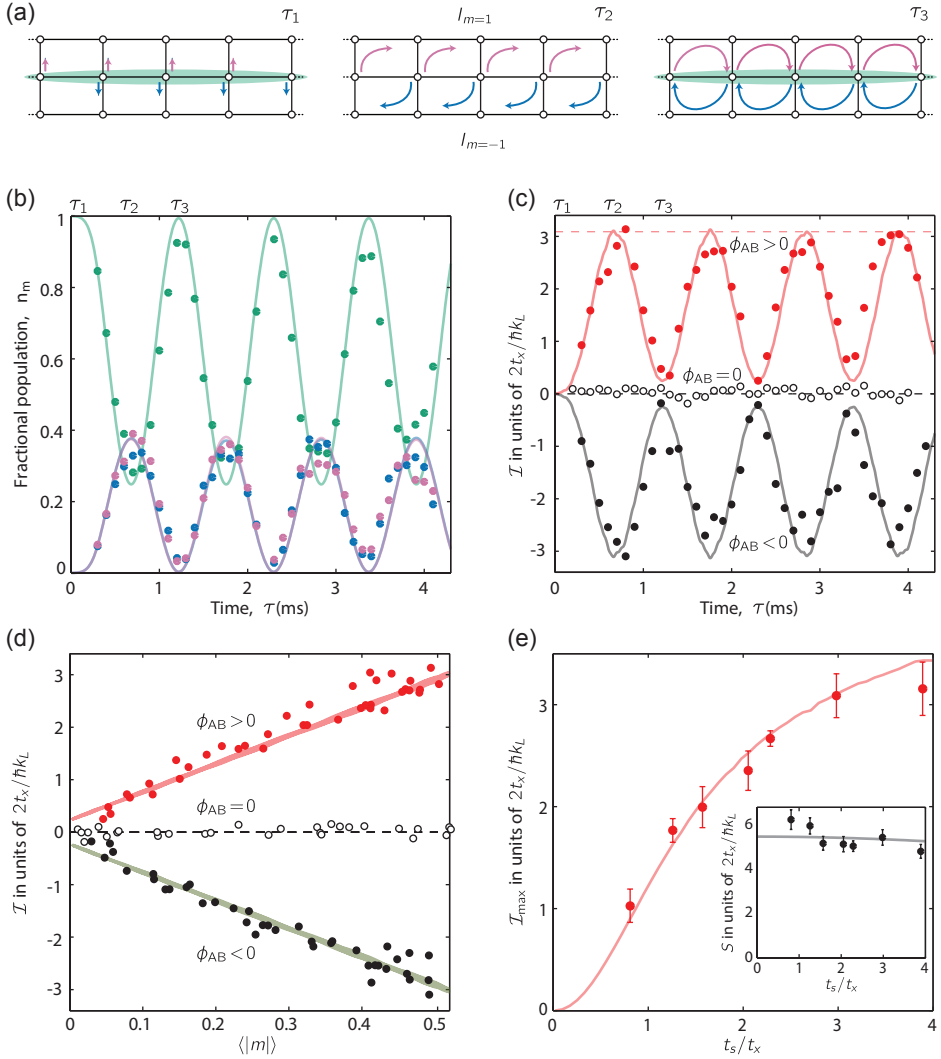


Figure 6: Measuring chiral currents in synthetic dimensions. (a) Schematic of the formation of chiral currents when the system is loaded into the bulk $m = 0$ site and tunneling along \mathbf{e}_s is turned on suddenly. (b) Fractional population in each spin state as a function of time for a system with $\phi_{AB} > 0$. Dots represent data and lines represent theory, with parameters $\hbar\Omega = 0.5E_L$, $V_0 = 6E_L$, $\hbar\delta = 0.001E_L$, and $\hbar\epsilon = 0.05E_L$. (c) Chiral current \mathcal{I} as a function of time for $\phi_{AB} > 0$ (red) $\phi_{AB} = 0$ (empty black dots) and $\phi_{AB} < 0$ (solid black). (d) Chiral current \mathcal{I} as a function of $\langle|m|\rangle$ for the three values of ϕ_{AB} . Solid lines calculated from theory, with the same parameters as in (b) for $\phi_{AB} \neq 0$, and with parameters $\hbar\Omega = 0.33E_L$, $V_0 = 6E_L$, $\hbar\delta = -0.01E_L$, and $\hbar\epsilon = 0.05E_L$ for $\phi_{AB} = 0$. (e) Peak chiral current \mathcal{I}_{\max} as a function of tunneling asymmetry t_s/t_x . Inset: slope of best fit lines of current \mathcal{I} as a function of $\langle|m|\rangle$ (as in (d)) as a function of tunneling asymmetry t_s/t_x : nearly independent.

the tunneling anisotropy: the asymmetry between the two dimensions. As shown in the inset to Figure 6e, the slope \mathcal{S} of the chiral current as a function of $\langle |m| \rangle$ is practically independent of the tunneling anisotropy. The small deviation from a flat line is explained by the deviation of our system from the tight binding model. However, the maximal chiral current attained during the pulsing experiment, \mathcal{I}_{\max} , depends strongly on the tunneling anisotropy (see Figure 6e). This is because the maximum fractional population in the edge states $\langle |m| \rangle$ increases with increased t_s . The increase is approximately linear at first, and then saturates at large t_s/t_x when the fractional population in the edge states $m = \pm 1$ approaches 1.

5.5 Observation of skipping orbits

Semiclassically, electrons in a 2-D material pierced by a magnetic field can be described in terms of cyclotron orbits in the bulk, as described in the previous section, and skipping orbits on the edge. Skipping orbits arise from electrons on the edge beginning cyclotron orbits, but hitting the edge of the system and being reflected and beginning the next cyclotron orbit. Due to the chirality of the cyclotron orbits, this results in the skipping orbits travelling in one direction along the top edge and in the opposite direction along the bottom edge.

We observed an analogue of these skipping orbits in our system. We performed the same experiment, pulsing on tunneling along the synthetic dimension, but this time initializing the system on the edge, as shown schematically in Figure 7a. To populate these states, we initially applied a detuning $\hbar\delta = \pm 0.087E_L$, tilting the potential along the synthetic direction as shown in Figure 7b. This made the initial state, $m = -1$ in the figure, a potential minimum. We then pulsed on the tunneling and observed the resulting dynamics.

Figure 7c shows the expectation value of position along \mathbf{e}_s as a function of time during the pulsing experiment. This expectation value is obtained by calculating

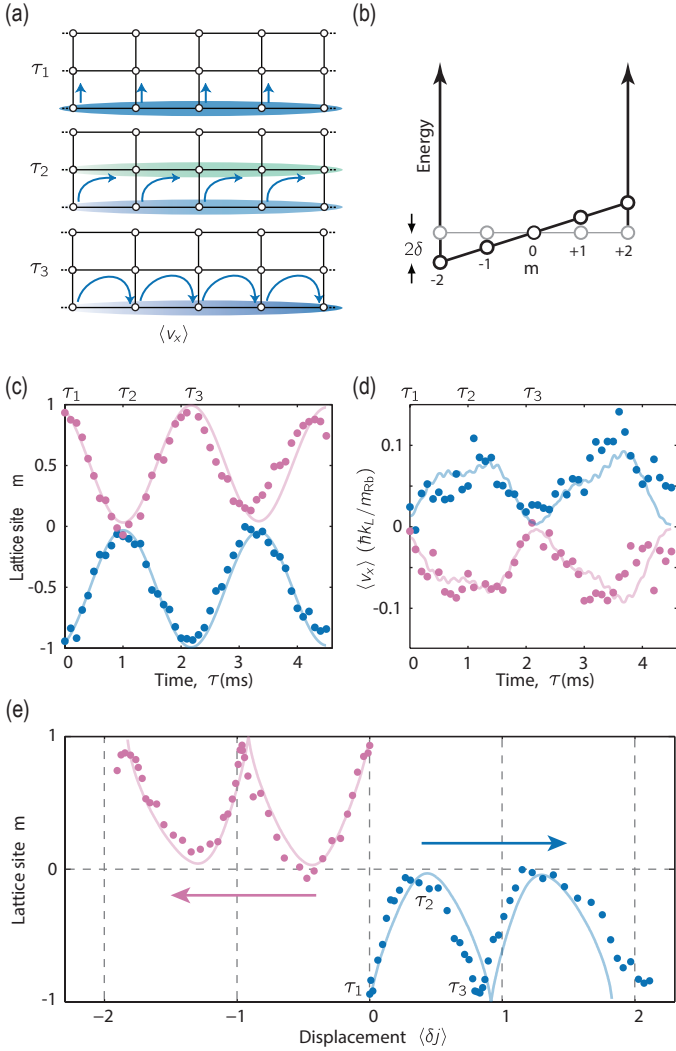


Figure 7: Imaging skipping orbits. (a) Schematic of pulsing experiment when atoms are initialized on the edge. (b) Schematic of the tilted box potential applied along the synthetic direction. (c) Expectation value of position along \mathbf{e}_s , $\langle m \rangle$, as a function of pulse time for atoms initialized in the $m = +1$ (red) and $m = -1$ (blue) states. Dots represent data and lines are from theory with parameters $\hbar\Omega = 0.41E_L$, $V_0 = 5.2E_L$, $\hbar\delta = \pm 0.087E_L$, and $\hbar\epsilon = 0.13E_L$. (d) Expectation value of the group velocity along \mathbf{e}_x , $\langle v_x \rangle$, for the same data as in (c). (e) Expectation value of displacement along \mathbf{e}_x , $\langle \delta j \rangle$ in units of lattice spacing, for the same data as in (c) and (d). The displacement was obtained by integrating $\langle v_x/a \rangle$, where a is the period of the optical lattice. Atoms initialized in $m = -1$ performed skipping orbits to the left, while atoms starting in $m = +1$ travelled to the right.

the fractional population n_m on each site m and summing $\langle m \rangle = \sum_m mn_m$. The red dots were obtained from an experiment where the atoms were initialized in the $m = 1$ site. The blue dots were obtained by starting in the $m = -1$ site. The expected position oscillated with time, as expected for Rabi oscillations. The same data was then used to extract the expected group velocity along \mathbf{e}_x , $\langle v \rangle = \sum_m n_m \langle v_m \rangle$ as a function of time. This is shown in Figure 7d. The group velocity oscillated with the expected position $\langle m \rangle$, and was positive for experiments starting in $m = -1$ and negative for experiments starting in $m = 1$.

We obtain the expected displacement in units of the lattice spacing a , $\langle \delta j \rangle$ along \mathbf{e}_x as a function of time by directly integrating the expected group velocity. The resulting displacement is shown in Figure 7e. As seen in the figure, for experiments initialized in $m = 1$, the atoms began cyclotron orbits, but reflected off the edge and performed skipping orbits towards the left. Likewise, atoms initialized in $m = -1$ performed skipping orbits along the opposite edge and in the opposite direction. This experiment presents the first direct observation of skipping orbit motion.

Appendix 6: Measuring Chern Number in Synthetic Dimensions

As discussed in Chapter 1, the 2D topological invariant as applied to band topology, the Chern number, is well defined for an infinite 2D system. For any finite system, the Chern number can be thought of as the Chern number of an infinite system that locally looks like the bulk of the finite system. This begs the question, how narrow can a system get for this extension of the definition of Chern number to still be meaningful?

In this chapter, we describe our experiment in measuring Chern number in the effectively 2-D synthetic dimensional lattice, as described in Chapter 5. This lattice was elongated along the real direction and extremely narrow along the synthetic direction, only 3 or 5 sites wide. We performed a transport experiment to sample the band structure of this system as a function of crystal momentum k_x along the real direction, and observed the resulting motion along the transverse, synthetic, direction, as shown schematically in Figure 1.

Figure 1a sketches the atoms loaded into the lowest band of the synthetic dimensions lattice in the $F = 2$ manifold of ^{87}Rb , creating 5 sites along the synthetic direction. As in Chapter 5, there was a 1D optical lattice along the longitudinal e_x direction, with lattice tunneling t_x between adjacent sites labelled by j . Internal spin states of the atoms defined sites along the transverse e_s direction, with tunneling t_s induced by either rf or Raman coupling. In the case of rf coupling, no phase was imprinted, $\phi_{AB} = 0$. In the case of Raman coupling, an overall phase $\phi_{AB} \neq 0$ was imprinted, and we choose the Landau gauge in which the phase is written on the

longitudinal tunneling coefficient $t_x = |t_x|e^{i\phi_{AB}m}$.

The histogram in Figure 1a shows the fractional populations n_m in each site m . An example hybryd TOF image (see sec. 5.2.3) is shown below in Figure 1c, with the central $m = 0$ order marked by red crosshairs. Then, a force is applied along the long (real) dimension of the system for some time Δt , and a transverse response is observed, as seen in Figure 1b. The fractional population has become maximized in the $m = 1$ site, and the sample hybrid TOF image in Figure 1d shows a displacement along the longitudinal momentum axis of Δq_x .

Due to the extremely narrow widths in the synthetic dimension, our measurement cannot be readily interpreted as a quantum Hall conductivity measurement, and a meaningful Chern number is not readily extracted that way, as discussed in sec. ???. However, we leverge the TKNN Diophantine equation [1] to perform an alternative measurement of the Chern number, discussed in ???. We show how this equation arises naturally in our synthetic dimensional system, and claim that with this metric we can extend the definition of the Chern meaningfully to systems as narrow as ours.

6.1 Experimental procedure

The setup for this experiment followed closely that of the original synthetic dimensions experiment, as described in sec. 5.1. In contrast with the experiment described in Chapter 5, we performed this experiment in both the $F = 1$ and $F = 2$ hyperfine manifolds of ^{87}Rb , creating both 3-site and 5-site wide strips. We began the experiment by adiabatically loading the full synthetic dimensional system for both $F = 1$ and $F = 2$, with both Raman coupling ($\Phi_{AB} \neq 0$) and rf coupling ($\Phi_{AB} = 0$).

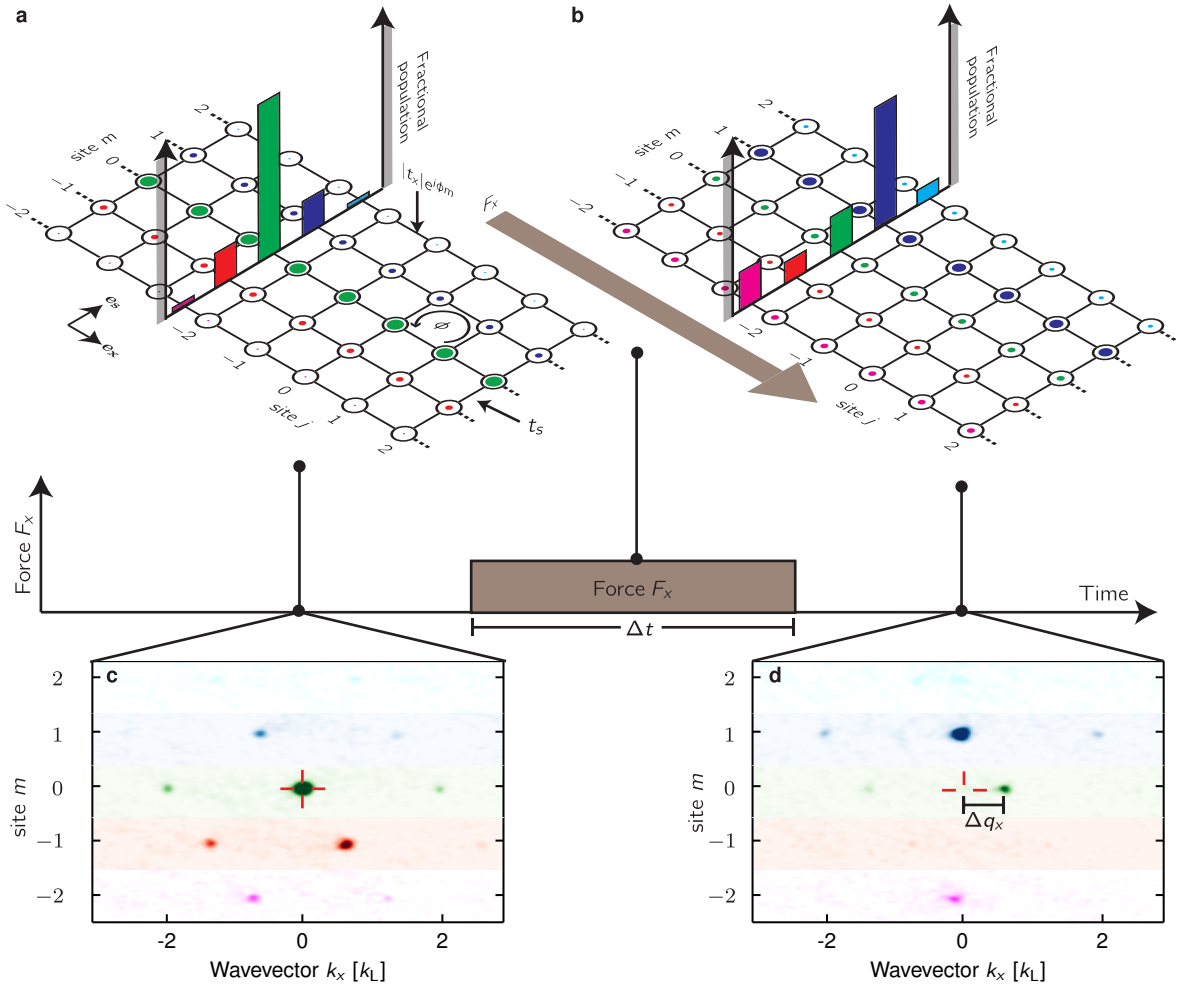


Figure 1: Quantum Hall effect in Hofstadter ribbons. (a) 5-site wide ribbon with real tunneling coefficients along e_s and complex tunneling coefficients along e_x , creating a non-zero phase ϕ around each plaquette. (b) After applying a force along e_x for a time Δt , atomic populations shift transversely along e_s , signaling the Hall effect. (c,d) TOF absorption images giving hybrid momentum/position density distributions $n(k_x, m)$. Prior to applying the force (c), the $m = 0$ momentum peak is at $k_x = 0$, marked by the red cross. Then, in (d), the force directly changed q_x , evidenced by the displacement Δq_x of crystal momentum, and via the Hall effect shifted population along e_s .

6.1.1 Loading procedures

The loading procedure for the Raman coupled case was as follows. Prepare a ^{87}Rb BEC (see sec. 2.3.3) in the $m_F = 0$ hyperfine state of the $F = 1$ manifold. Ramp on the 1D optical lattice along e_x adiabatically in 300 ms. For experiments in the $F = 2$ manifold, microwaves were then used to transfer into said manifold whiel already in the lattice [DONT REMEMBER EXACT PROCEDURE FOR THIS LOOK UP ON EXPERIMENT]. This was done after lattice loading to minimize the amount of time the atoms spent in the $F = 2$ manifold and thereby limit the spin-changing collisions and losses associated with that state [FIND CITATION FOR THIS]. Then, the Raman coupling field was ramped on adiabatically in 30 ms.

Loading the ground state of the $F = 2$ manifold presented a unique restriction, as illustrated by Figure 2. For the experiments described in Chapter 5, a bias magnetic field B_z was chosen such that the effectic quadratic Zeeman shift $\hbar\epsilon = 0.05E_L$, in lattice recoil energy units. However, in the $F = 2$ case at this field, with a lattice depth of $4.4E_L$, the $m_F = 0$ ground state does not adiabatically connect to the Raman-coupled ground state. This is because, as shown in the band structure in Figure 2a, the $m_F = \pm 2$ energies of the lattice-coupled system at $q_x = 0$ are lower in energy than the $m_F = 0$ state. Therefore, to avoid this issue, we chose a bias field such that the quadratic Zeeman shift was $\hbar\epsilon = 0.02E_L$. The band structure for this case is shown in Figure 2b. Here, the $m_F = 0$ sinusoid at crystal momentum $q_x = 0$ is still the lowest energy, and therefore connects adiabatically to the Raman coupled ground state.

For the case where tunneling along the synthetic dimension was provided by rf coupling ($\Phi_{AB} = 0$), the loading procedure was as follows. Start in the $F = 1, m_F = -1$ state, we turned the 1D optical lattice on adiabatically in 300 ms, same as the Raman case. For $F = 2$, we then transferred to the $F = 2, m_F = -2$ state [CHECK

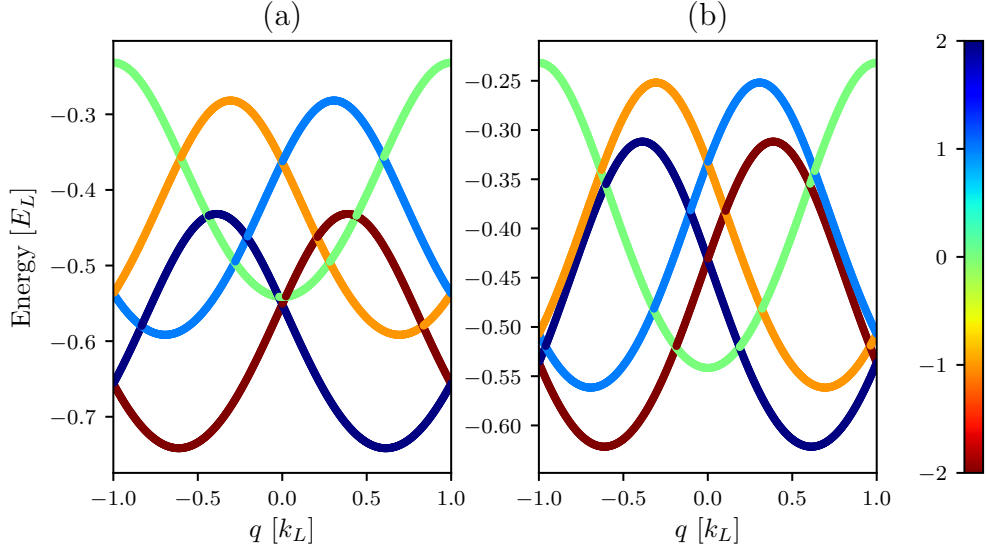


Figure 2: Band structure of the lattice-coupled system in $F = 2$. Here, lattice depth $V_0 = 4.4E_L$, Raman coupling $\hbar\Omega = 0$, and detuning $\hbar\delta = 0$. (a) Quadratic shift $\hbar\epsilon = 0.05E_L$. At $q_x = 0$, $m_F = 0$ is not the ground state. (b) Quadratic shift $\hbar\epsilon = 0.02E_L$. At $q_x = 0$, $m_F = 0$ is the ground state.

HOW THIS IS DONE]. Then, we set the bias field to a large detuning $\hbar\delta > 1E_R$. Implementing adiabatic rapid passage (see sec. 1.2.3), we then swept the field to resonance in ≈ 50 ms, thereby loading the rf coupled ground state. This is necessary in the rf case as opposed to the Raman case, because there is no momentum shift in the band structure, and therefore turning on the rf coupling opens up an avoided crossing at $q_x = 0$ and everywhere else, making it impossible to be adiabatic with respect to this turn on while on resonance.

6.1.2 Application of force and measurement

After adiabatically loading the ground state at $q_x = 0$ for all the configurations, we applied a constant force to the atoms, inducing a linear evolution of the crystal momentum given by

$$F_x = \hbar \frac{dq_x}{dt}. \quad (6.1)$$

To apply this force, we displaced the crossing beam of the ODT, such that

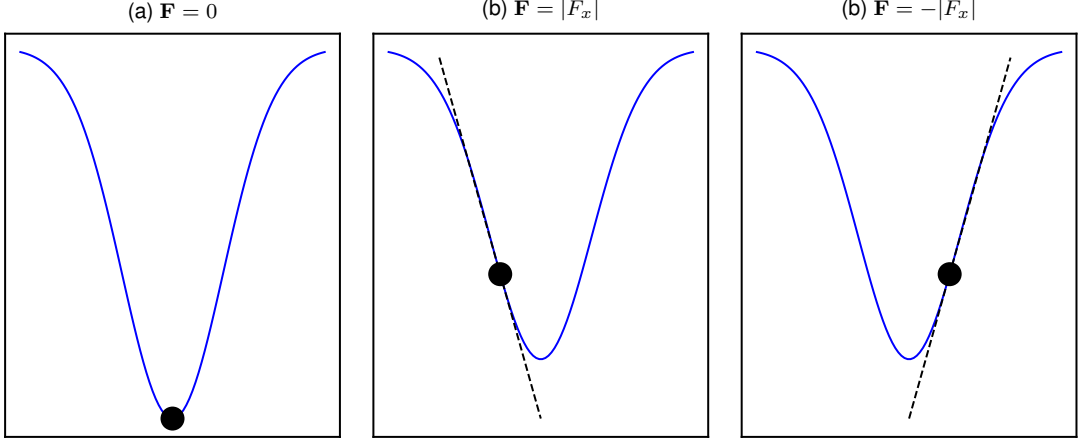


Figure 3: Application of a constant force by displacing a Gaussian beam potential. (a) Atoms are at the minimum of the Gaussian potential, not experiencing a force. (b) Beam is displaced to the left, atoms experience a local linear potential resulting in a constant positive force. (c) Beam is displaced to the right, atoms experience a local linear potential resulting in a constant negative force.

instead of being held at the potential minimum, the atoms were on an edge of the Gaussian beam, with a locally linear optical potential. This displacement was achieved by frequency shifting the AOM that controlled the split between the two ODT orders (see fig. 7). This is shown schematically in Figure 3. Figure 3a shows the atoms (indicated by a black dot) at the minimum of the gaussian crossing beam (potential in blue), with no force applied. Figure 3b shows the beam displaced to the right relative to the atoms, and the locally linear potential experienced by the atoms results in a positive force. Similarly, in Figure 3c the beam is displaced to the left resulting in a negative force.

An example of the resulting evolution of the system is shown in Figure 4. Figure 4a shows the lowest three bands of the Raman coupled synthetic dimensions band structure in the $F = 2$ manifold, for our approximate experimental parameters of $V_0 = 4.4E_L$, $\hbar\Omega = 0.5E_L$, $\hbar\delta = 0E_L$ and $\hbar\epsilon = 0.02E_L$. The starting point of the BEC at $q_x = 0$ is indicated by the black dot in the lowest band. The color indicates

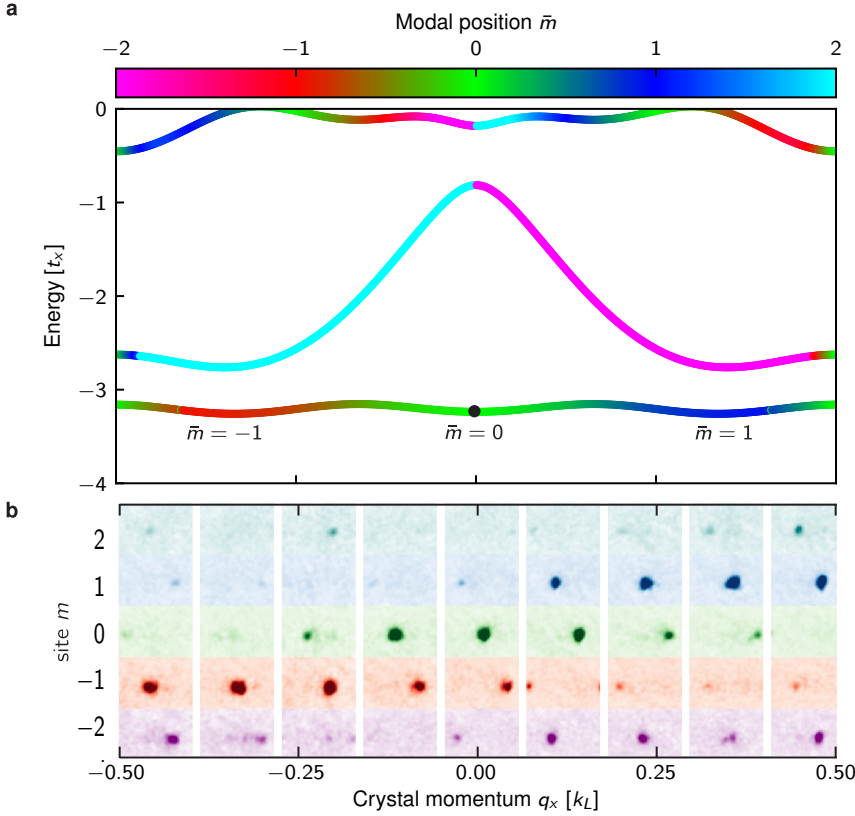


Figure 4: Band structure in a 5-site wide ribbon. (a) Band structure computed using full Hamiltonian for a $4.4E_L$ deep 1-D lattice ($\lambda_L = 1064$ nm), $0.5E_L$ Raman coupling strength ($\lambda_R = 790$ nm), and quadratic Zeeman shift $\epsilon = 0.02E_L$, giving $\Phi/\Phi_0 \approx 4/3$, $t_x = 0.078(2)E_L$, $t_s = 2.3(1)t_x$. The color indicates modal position \bar{m} . The black dot indicates the initial loading parameters. (b) TOF absorption images $n(k_x, m)$ for varying longitudinal crystal momenta q_x .

the modal position \bar{m} along the synthetic direction. Modal position is a slight variant on the magnetization used in sec. 5.2.2. The modal position was found by taking the fractional populations n_m in the different m sites at a given crystal momentum, and fitting them to a Gaussian distribution. The peak of the Gaussian distribution was taken as the modal position \bar{m} . In this experiment, we use \bar{m} as the metric of location along \mathbf{e}_s in favor of the more conventional magnetization given by $\langle m \rangle = \sum_m m * n_m$ to avoid the large uncertainties introduced in the magnetization from number fluctuations in the extremal $m = \pm F$ sites.

We displaced the crossing ODT beam to one side to apply a positive force,

inducing motion to the right $q_x \rightarrow q_x > 0$ in the band structure, for various amounts of time Δt inducing various changes in crystal momentum Δq_x . We then followed the same measurement protocol as described in sec. 5.2.3: we abruptly turned off the lattice, Raman or rf, and trapping ODT beams and allowed the atoms to expand in time-of-flight for 16 ms, mapping initial momentum k_x to position on the TOF images. During TOF, we applied a 2 ms [CHECK THIS NUMBER] Stern-Gerlach gradient pulse, separating the atoms according to site m along an axis perpendicular to e_x . We therefore performed a hybrid measurement of momentum k_x along the longitudinal e_x axis and single site resolved position m along the transverse e_s direction.

From these hybrid TOF images, we extracted the fractional population in each site m . In addition, from the change in position along the momentum axis k_x we detected the crystal momentum Δq_x for each image, as shown in Figure ??c,d. We therefore observed the evolution in the fractional populations and modal position as a function of q_x . Sample TOF images at different values of the crystal momentum are shown in Figure 4, with different single-site resolved imaging along e_s represented in the vertical direction, different m sites shaded in different colors, corresponding to the colorbar in Figure 4a. Similarly, the ODT crossing beam was displaced to the opposite side an equal amount, applying the same magnitude of force in the opposite direction and including motion to the left $q_x \rightarrow q_x < 0$ in the band structure. In this way, we obtained a complete map of the fractional populations n_m in each transverse site m for each value of the longitudinal crystal momentum q_x .

6.1.3 Density reduction

When force was applied to the atoms, their crystal momentum q_x evolved, and they were no longer confined to a minimum of the band structure. This opened up the possibility for two-body collisions between the atoms that conserved the overall

momentum and energy of the pair while changing the crystal momentum of each atom [67]. This lead to a smearing of the atoms along the crystal momentum axis, obscuring the measurement.

To mitigate this problem, it was necessary to cut down on the atomic density as much as possible while retaining enough atoms to observe a signal. In addition to re-shaping the ODT beam (see sec. 2.3.4.4), we also cut down the overall atom number after creating the BEC and before loading the synthetic dimensional lattice. Starting in $F = 1, m_F = 0$, we applied a microwave pulse resonant with the $|F = 1, m_F = 0\rangle \rightarrow |F = 2, m_F = -1\rangle$ transition for 1 ms [CHECK THIS NUMBER], until $\approx 80\%$ of the atoms were transferred to the $F = 2$ manifold. We then shined on the XZ probe beam to selectively blow away the $F = 2$ atoms, leaving ≈ 1000 atoms in the condensate.

6.1.4 Rf correction

For rf-coupled experiments, our loading procedure into the lowest band at $q_x = 0$ resulted in some latent non-adiabaticity that we could not get rid of or fully explain. This non-adiabaticity resulted in oscillations in the fractional populations n_m as a function of time, even though the rf-coupled band structure predicts no dependence of n_m on q_x . However, these oscillations were present as a function of time even when no force was applied to the atoms, indicating that these variations were dependent on time and on not q_x . Therefore, we used data obtained with no force applied to correct the time-dependent variation in data where the force was applied.

Our correction procedure is shown in Figure 5. Figure 5a,b,c shows the raw fractional populations as a function of time for the case where a force was applied to the right, to the left, and not at all, respectively. Note that the observed oscillations are quite large, but consistent between the three cases. This implies that

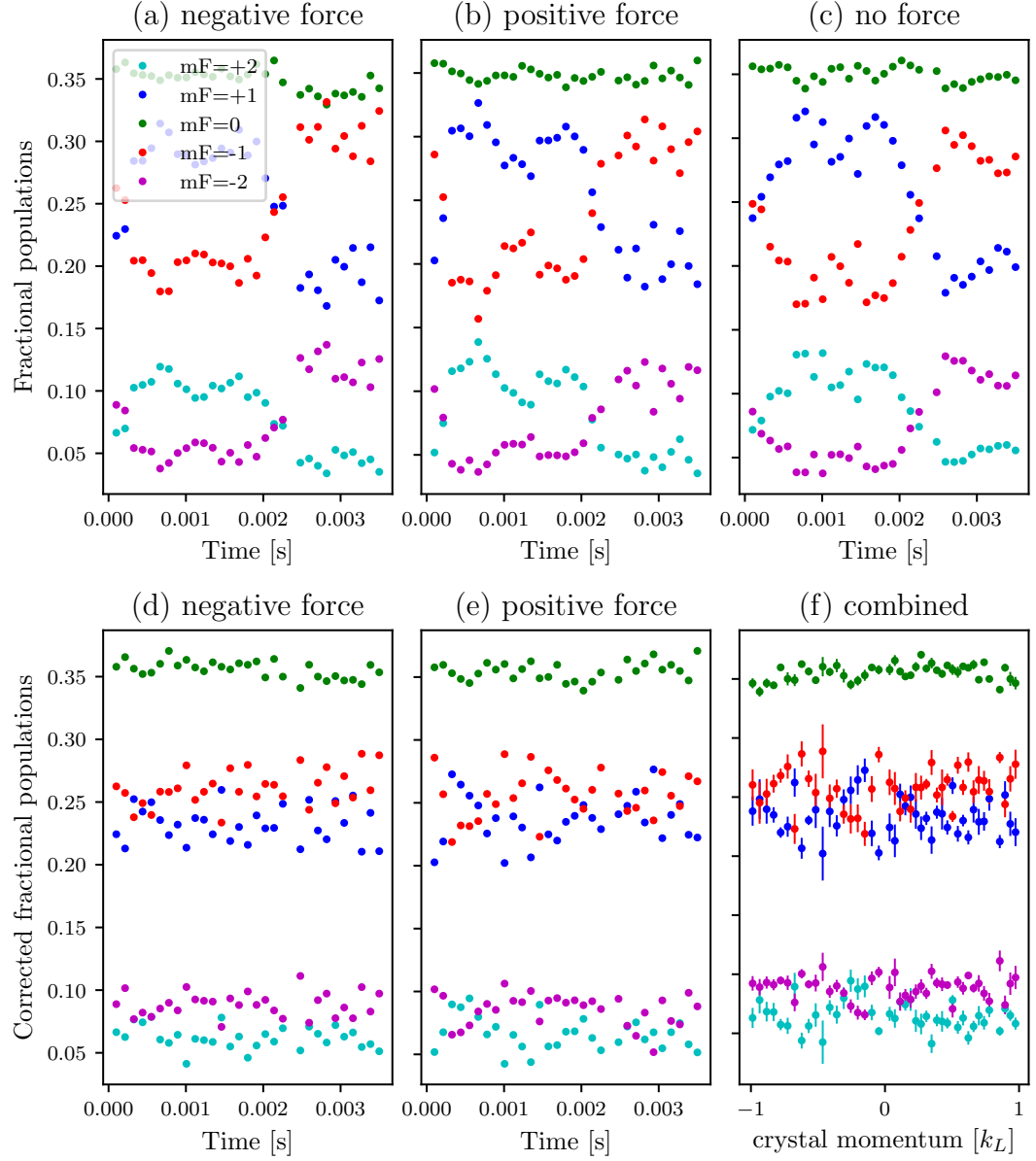


Figure 5: Correction of oscillations in rf coupled data. (a,b,c) Raw fractional populations n_m observed as a function of time Δt with (a) positive force applied, (b) negative force applied, and (c) no force applied. (d,e) Corrected fractional populations $n_m^{\text{corrected}}$ with (d) positive force applied, (e) negative force applied. (f) Corrected data as a function of crystal momentum for both force directions combined.

whatever mechanism is causing these oscillations is a time dependent one and not a consequence of any change in longitudinal crystal momentum q_x .

To correct the data and extract the change in fractional populations caused by varying q_x , we first calculate the change in fractional population as a function of time for the data with no force applied. This is given by $\Delta n_m^{F=0}(t) = n_m^{F=0}(t) - n_m^{F=0}(0)$. We then subtract this change from the data with force applied via $n_m^{F \neq 0, \text{corrected}}(t) = n_m^{F \neq 0}(t) - \Delta n_m^{F=0}(t)$. These corrected fractional populations as a function of time are shown in Figure 5d,e for positive and negative force, respectively. In Figure 5f, we have combined the corrected positive and negative force data and plotted it as a function of crystal momentum, effectively mapping out the fractional populations everywhere in the lowest band.

Field stabilization

6.2 Quantum Hall Effect interpretation

The measurement we performed is similar to a quantum Hall conductivity measurement: we pierced a 2D material with an effective magnetic field, applied a force (an electric field in a conventional quantum Hall setup), and observed a transverse response. To draw a more direct analogy, we can describe the quantum Hall effect from the microscopic perspective.

6.2.1 Microscoping view of QHE

In the quantum Hall effect, a longitudinal force F_{\parallel} , induced by an electric field $F_{\parallel} = eE_{\parallel}$, drives a transverse ‘Hall’ current density

$$j_{\perp} = \sigma_H E_{\parallel}, \quad (6.2)$$

where σ_H is the Hall conductivity. This transverse current density can be expressed as

$$j_\perp = n_{2D} v_\perp e, \quad (6.3)$$

where n_{2D} is the 2-D charge carrier density, v_\perp is the transverse velocity of the charge carriers and e is the electron charge. Choosing some increment of time Δt , we can express v_\perp and F_\parallel as

$$v_\perp = \frac{\Delta x_\perp}{\Delta t}, \quad (6.4)$$

and

$$F_\parallel = \hbar \frac{\Delta q_\parallel}{\Delta t}, \quad (6.5)$$

where q_\parallel is the crystal momentum along the direction of the force. Plugging this into eqn. 6.2, we obtain

$$n_{2D} e \frac{x_\perp}{\Delta t} = \hbar \frac{\Delta q_\parallel}{\Delta t} \frac{\sigma_H}{e} \quad (6.6)$$

Re-expressing n_{2D} in number of carriers N per plaquette, defining Δx_\perp as transverse displacement in units of lattice periods, we plug the above definitions into eqn. 6.2 to obtain

$$NG \frac{\Delta x_\perp}{\Delta q_\parallel} = \sigma_H \frac{h}{e^2}, \quad (6.7)$$

where G is the reciprocal lattice vector.

In addition, we know that the quantum Hall conductivity can be expressed in terms of the Chern numbers C_n of the occupied bands n as

$$\sigma_H = \frac{e^2}{h} \sum_n C_n. \quad (6.8)$$

In the conventional case of Landau levels, where each Landau level has a Chern number $C_n = 1$, this amounts to the number of filled bands ν , giving $\sigma_H = \nu e^2/h$. In our case, where the Chern number is not necessarily 1 and only the lowest band

is occupied, this instead reduces to the Chern number of the lowest band which we will just call C , giving $\sigma_H = Ce^2/h$. Plugging this into eqn. 6.7, we can write

$$NG \frac{\Delta x_{\perp}}{\Delta q_{\parallel}} = C \quad (6.9)$$

Therefore, if we observe (as was done in our measurement) the ratio of transverse displacement Δx_{\perp} to the longitudinal crystal momentum Δq_{\parallel} , we should be able to fit that to a line and directly extract the Chern number C .

6.2.2 Chern number from Hall conductivity

We used the prescription given in the previous section to extract a Hall conductivity and therefore a Chern number from our data. The results for a 5-site wide strip ($F = 2$) are shown in Figure 6a,b,c (top) for all values of flux studied: $\Phi/\Phi_0 = 0$, $\Phi/\Phi_0 \approx -4/3$, and $\Phi/\Phi_0 \approx 4/3$, respectively. We calculated the modal position \bar{m} (see sec. 6.1.2) of our atoms along \mathbf{e}_s as a function of longitudinal crystal momentum q_x . The data is represented by gray dots, with uncertainty bars reflecting the propagated standard uncertainty from averaging six identical runs. For zero flux $\Phi/\Phi_0 = 0$ (Fig. 6a), \bar{m} was independent of q_x ; in contrast, for non-zero flux $\Phi/\Phi_0 \approx \pm 4/3$ (Fig. 6b,c), \bar{m} depends linearly on q_x with non-zero slope.

Here, the change in \bar{m} was a transverse displacement Δx_{\perp} . We fit the modal position as a function of q_x to a line, black dashes in the figure. From the slope of the line, we used eqn. 6.9 to extract the Chern number. We obtained $C = 0.01(1)$, $0.87(3)$, and $-0.85(3)$ for zero, negative and positive flux respectively. This shows the correct qualitative behavior, but differs significantly from expected values of $0, \pm 1$.

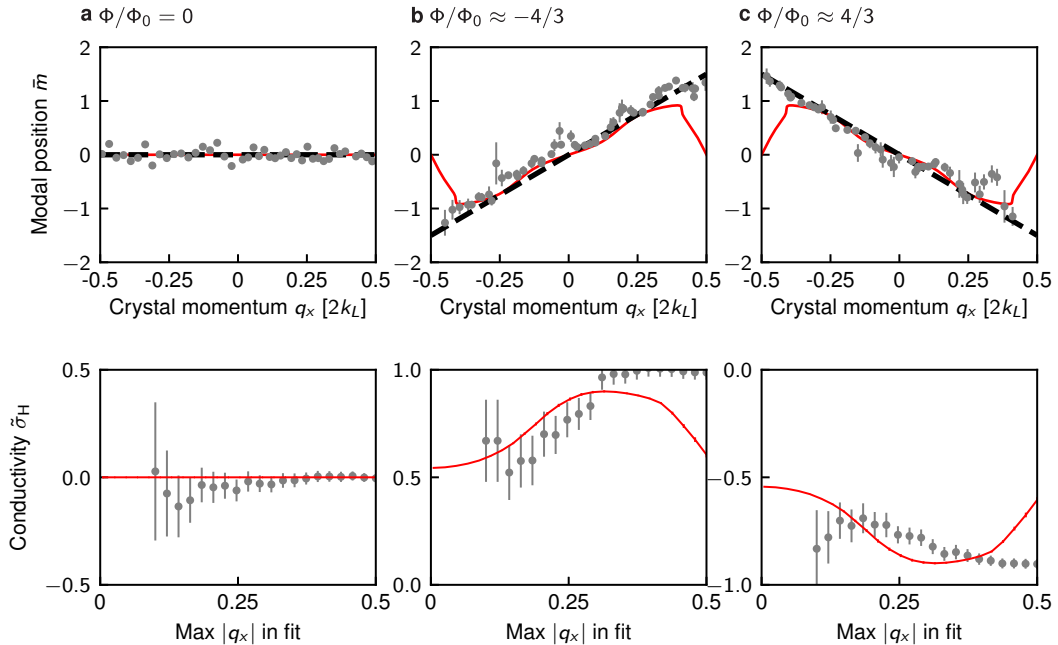


Figure 6: Hall displacement. Top: modal position \bar{m} is plotted as a function of q_x for the 5-site ribbon with flux **a.** $\Phi/\Phi_0 = 0$, **b.** $\Phi/\Phi_0 \approx -4/3$, **c.** $\Phi/\Phi_0 \approx 4/3$. Gray circles depict the measurements; black dashed lines are the prediction of our simple $\tilde{\sigma}_H$ and red curves are the expectation from the band structure of our thin ribbon. Bottom: Extracted conductivity from the slope of a line of best fit to the data (gray circles) and theory (red lines) as a function of maximum $|q_x|$ included in the fit range, for each flux value. As discussed in sec. 6.1.4, the $\Phi/\Phi_0 = 0$ data was compensated to account for non-adiabaticity in the loading procedure.

6.2.3 Inadequacy for narrow systems

The red curves in Fig. 6(top) show the expected behavior for our 5-site wide system for adiabatic changes in q_x as calculated from exact diagonalization of the full Hamiltonian (see sec. 5.2.1), always within the lowest band (Fig. ??a), i.e., Bloch oscillations. This theory predicts a nearly linear slope for small q_x sharply returning to $\bar{m} = 0$ at the edges of the Brillouin zone. A linear fit to this theory produces $\tilde{\sigma}_H \approx 0, 0.6$, and -0.6 for zero, negative and positive flux respectively, far from the Chern number. In addition, they differ significantly both from the data and from the linear fit at the edges of the Brillouin zone.

This discrepancy is resolved by recalling that Bloch oscillations require adiabatic motion, meaning no transition to higher bands can happen. This is possible in the narrow system under study, but quickly becomes impossible as the size of the system grows. This is illustrated in Figure ???. Figure ??a shows the band structure of our 5-site ($F = 2$) strip, with parameters used in the experiment. Here, there are non-negligible band gaps at the edges of the Brillouin zone between the lowest and second bands. With a weak enough force, the atoms could traverse this region slowly enough to be adiabatic with respect to this band gap. However, for a larger system, such as the 41-site wide system whose band structure is shown in Figure ??b, these band gaps become negligibly small and adiabaticity is impossible.

The departure of the data in Fig. 6(top) from the adiabatic theory (red lines) at the edges of the Brillouin zone indicates a partial break down of adiabaticity was present in our data. However, it is not a complete breakdown as the data also differs from the linear fit at the edges of the Brillouin zone. The data was somewhere in the partially adiabatic regime, only possible for our narrow system. This made neither the adiabatic theory, nor the linear fit assuming perfect non-adiabaticity, applicable to our system. Therefore, the linear fit is not a good measure of the Chern number

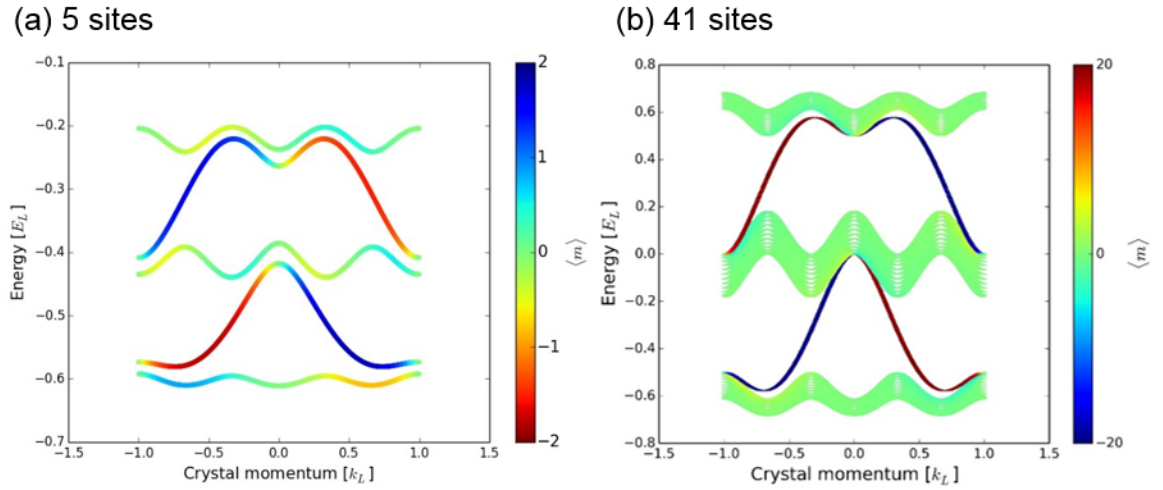


Figure 7: Band structure of the synthetic dimesnions lattice with flux $\Phi/\Phi_0 = -4/3$. (a) 5-site wide system with experimental parameters $V_0 = 4.4$, $\hbar\Omega = 0.5$, $\hbar\delta = 0$, and $\hbar\epsilon = 0.02$. There is a band gap between the first and second bands at the edge of the Brillouin zone. (b) 41-site wide system with parameters $V_0 = 4.4$, $\hbar\Omega = 0.5$, $\hbar\delta = 0$, and $\hbar\epsilon = 0$ and no Clebsch-Gordan coefficients included. The band gap between the first and second bands at the edge of the Brillouin zone is negligibly small.

for our system.

One might suspect that limiting the domain of the linear fit such that band edge effects are excluded would still provide a good measure of the Chern number. This is not the case, as can be seen in Fig. 6(bottom). Here, we plot the measured Chern number for a linear fit to our data (grey) and the adiabatic theory (red) for a limited range of crystal momenta q_x . The range of the fit is plotted on the x axis, ranging from only the center to the entire Brillouin zone. The slope of the best fit line for non-trivial topologies ($\Phi/\Phi_0 \neq 0$) and thus the measured Chern number, depends highly on the selected domain for both the theoretical (red) and experimental (black) data, and the appropriate choice of range is ambiguous. We conclude that for an extremely narrow system such as ours, a conductivity measurement is insufficient for determining the Chern number at reasonable tunneling strengths [68].

6.3 Measuring Chern number via Diophantine equation

To better identify the Chern number in our system, following theoretical work [68–72], we leveraged the TKNN Diophantine equation to determine the Chern number of our system. This equation states that for rational flux $\Phi/\Phi_0 = P/Q$ (for relatively prime integers P and Q) the integer solutions s and C to the Diophantine equation

$$1 = Qs - PC \quad (6.10)$$

uniquely¹ determine the Chern number C of the lowest band.

Surprisingly, the TKNN equation (Eqn. 6.10) has a direct interpretation in the physical processes present in our system. Although the Hofstadter Hamiltonian in Eqn. ?? is only invariant under m -translations that are integer multiples of

¹Subject to the constraint $|C| \leq |Q|/2$ [1, 73]. The integer s has no bearing on our argument, but has been interpreted as the charge transported when the periodic potential is adiabatically displaced [?, ?].

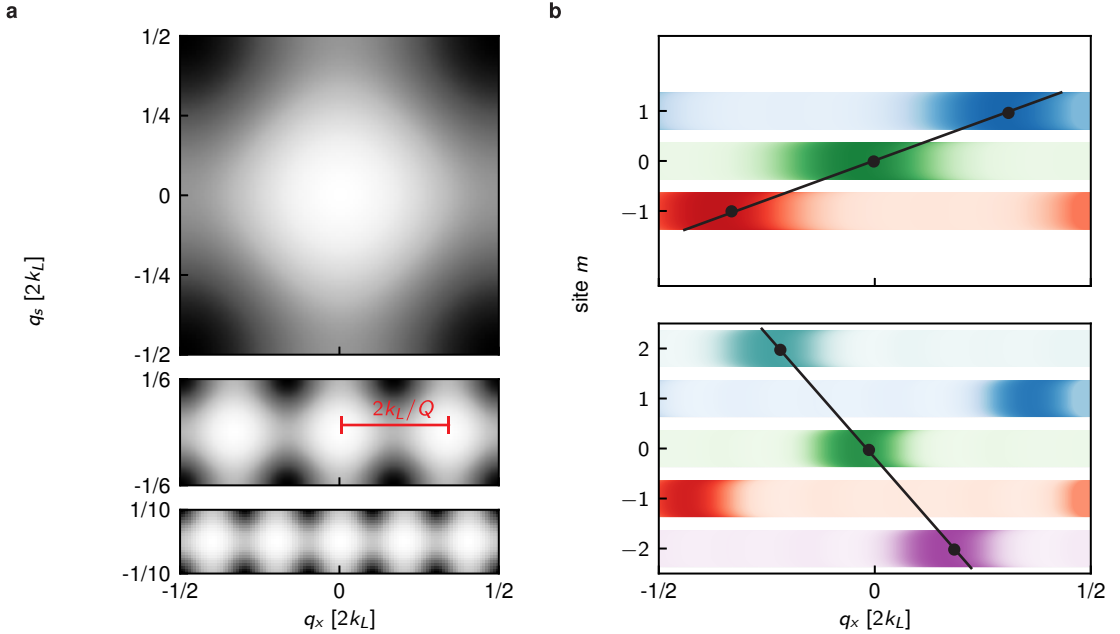


Figure 8: Chern number from the TKNN equation. (a). Lowest band energy within the Brillouin zone in an extended 2-D system, where q_x and q_s are crystal momenta along e_x and e_s , respectively. Top. $\Phi/\Phi_0 = 0$. Middle. $\Phi/\Phi_0 = 1/3$: Brillouin zone shrinks by a factor of 3 and becomes 3-fold degenerate, distance between adjacent energy minima spaced by $2k_L/Q$ is labeled. Bottom. $\Phi/\Phi_0 = 2/5$. (b). Fractional population in each spin state in the lowest band at $q_s = 0$. Top. $\Phi/\Phi_0 = 1/3$. Bottom. $\Phi/\Phi_0 = 2/5$. A momentum shift along e_x of $2k_L/Q$ is accompanied by an integer number of spin flips C . A line connecting magnetic states separated by $2k_L/Q$, with slope $C = 1$ (top) and -2 (bottom), is indicated.

Q , a so-called “magnetic-displacement” by $\Delta m = 1$ accompanied with a crystal momentum shift $\Delta q_x/2k_R = P/Q$ leaves Eqn. ?? unchanged. Together, these symmetry operations give a Q -fold reduction of the Brillouin zone along \mathbf{e}_s , and add a Q -fold degeneracy, as illustrated in Fig. 8a for $\Phi/\Phi_0 = 0, 1/3$, and $2/5$. Recalling that the Brillouin zone is $2\hbar k_L$ periodic along \mathbf{e}_x , it follows that a displacement by $2k_L/Q$ to the nearest symmetry related state involves an integer C magnetic displacements, shown in Fig. 8b for $\Phi/\Phi_0 = 1/3$ and $2/5$, given by solutions to $2k_L s - 2k_R C = 2k_L/Q$, where s counts the number of times the Brillouin zone was “wrapped around during the C vertical displacements. Because this is exactly the TKNN equation (6.10), we identify C as the Chern number.

Both C and s directly relate to physical processes. First, each time the Brillouin zone is wrapped around implying a net change of momentum by $2\hbar k_L$ a pair of photons must be exchanged between the optical lattice laser beams. Second, each change of m by 1 must be accompanied by a $2\hbar k_R$ recoil kick imparted by the Raman lasers as they change the spin state. This physical motivation of the TKNN equation remains broadly applicable even for our narrow lattice, providing an alternate signature of the Chern number.

The prescription we used to identify the Chern number from our data and theoretical calculations through the Diophantine equation argument is detailed in Figure 9. Figure 9a shows the fractional populations in each m site as a function of q_x for a 3-site wide strip ($F = 1$ data) with flux $\Phi/\Phi_0 \approx -4/3$. Each of the fractional populations (red, green, and blue representing $m = -1, 0$, and 1 respectively) was fit to a parabola to extract the peak. These peak locations were interpreted as the band structure minima corresponding to each m site. These points were then plotted as in Figure 9c, with site m as a function of its maximizing crystal momentum q_x . These points were then fit to a line, whose slope was identified as the Chern number C . The same prescription was used to obtain the theoretical predictions, as shown in Figure

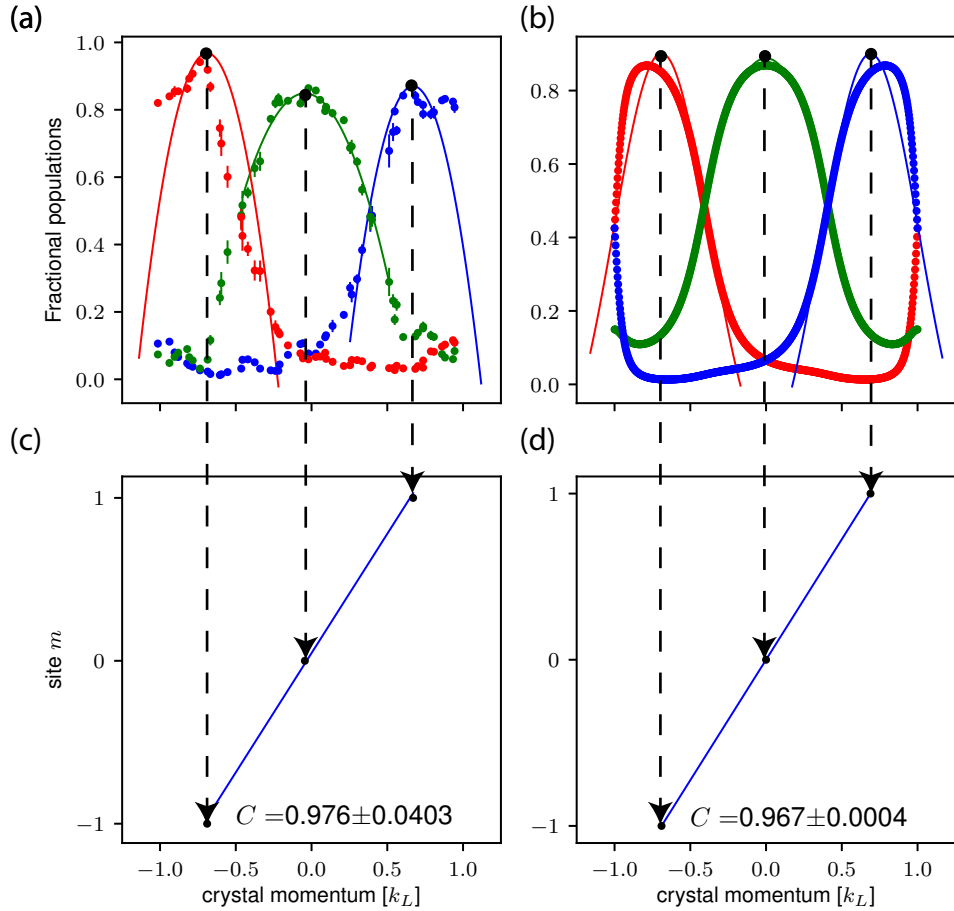


Figure 9: Calculating Chern number. (a) Fractional populations in $m = -1, 0$ and 1 sites (red, green, and blue respectively) as a function of q_x for data taken in a 3-site wide strip ($F = 1$ data) with flux $\Phi/\Phi_0 \approx -4/3$. Dots represent data, lines represent parabolic fits. (b) Theoretically calculated fractional populations for the same system. (c) Site m as a function of maximizing q_x from fits to data in (a). Best fit line to the three points has a slope corresponding to the Chern number C . (d) Site m as a function of maximizing q_x from fits to theory in (b). Best fit line to the three points has a slope corresponding to the Chern number C .

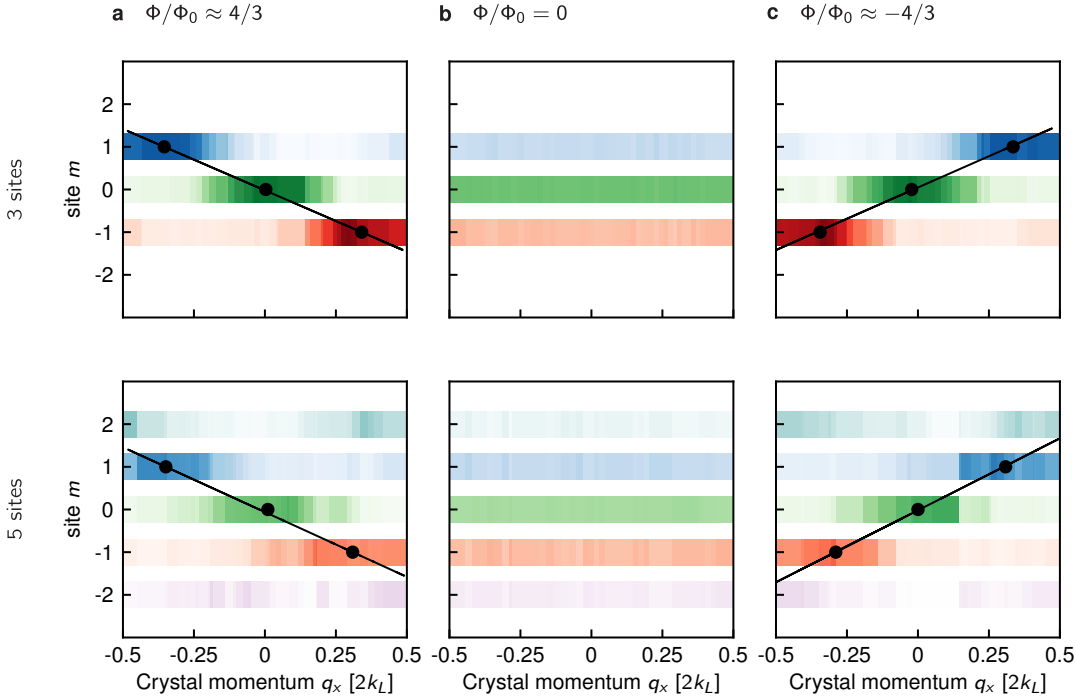


Figure 10: Chern number measurement. Lowest band fractional population measured as a function of crystal momentum in the e_x and position in the e_s . Darker color indicates higher fractional population. In the Raman-coupled cases, the points represent the fitted population maxima and the Chern number is extracted from the best fit line to those points. (a). 3-site (left) and 5-site (right) systems with positive flux. (b) 3-site (left) and 5-site (right) system with zero flux. (c). 3-site (left) and 5-site (right) systems with negative flux. The parameters for 3-site data were identical to those for 5-site data, see Fig. 6 a, except $t_s = 2.880(1)t_x$.

9b,d. The theoretical fractional populations were obtained from the eigenvectors corresponding to the lowest band of the full Hamiltonian, eqn. 5.2.1.

6.4 Results and conclusion

Figure 10 shows the full evolution of fractional population in each m site as a function of crystal momentum q_x in the lowest band, for all preparations studied in the experiment: 3- and 5-site wide strips, with fluxes $\Phi/\Phi_0 = 0, \approx \pm 4/3$. The black circles locate the peak of the fractional population in each spin state. From these data, we extract the Chern number through the procedure described in the

previous section.

For the 3-site wide ribbon ($F = 1$ data), we measured a Chern number of $0.99(4)$, $-0.98(5)$ for negative and positive flux respectively², in agreement with the exact theory which predicts $\pm 0.97(1)$, with uncertainties reflecting fit uncertainty of peak locations. For the 5-site wide ribbon, we measured $1.11(2)$, $-0.97(4)$, close to the theoretical prediction of $\pm 1.07(1)$. The deviation from unity results from $\Phi/\Phi_0 - 4/3 \approx 0.01$, a non-zero quadratic Zeeman shift, and $t_s > t_x$ allowing hybridization of the edge states [68].

Discussion: Chern number measured in this way as a function of coupling strength, size...

²Our Chern number extraction scheme fails for the rf case as the fractional populations are flat and there is no peak. We therefore assign a Chern number of 0 to flat distributions.

Bibliography

- [1] D. J. Thouless, M. Kohmoto, M. P. Nightingale, and M. den Nijs. Quantized hall conductance in a two-dimensional periodic potential. *Phys. Rev. Lett.*, 49:405–408, Aug 1982.
- [2] Xiao-Liang Qi and Shou-Cheng Zhang. Topological insulators and superconductors. *Rev. Mod. Phys.*, 83:1057–1110, Oct 2011.
- [3] Horst L. Stormer. Nobel lecture: The fractional quantum hall effect. *Rev. Mod. Phys.*, 71:875–889, Jul 1999.
- [4] N.W. Ashcroft and N.D. Mermin. *Solid State Physics*. Saunders College, Philadelphia, 1976.
- [5] Daniel Adam Steck. Rubidium 87 d line data. Available online, <http://steck.us/alkalidata>, April 2018. revision 2.1.5.
- [6] T. G. Tiecke. Properties of potassium. Available online, <http://www.tobiastiecke.nl/archive/PotassiumProperties.pdf>, May 2011. v1.02.

- [7] G. Breit and I. I. Rabi. Measurement of nuclear spin. *Phys. Rev.*, 38:2082–2083, Dec 1931.
- [8] H.J. Metcalf and P. van der Straten. *Laser Cooling and Trapping*. Graduate Texts in Contemporary Physics. Springer New York, 1999.
- [9] Nicola Marzari, Arash A. Mostofi, Jonathan R. Yates, Ivo Souza, and David Vanderbilt. Maximally localized wannier functions: Theory and applications. *Rev. Mod. Phys.*, 84:1419–1475, Oct 2012.
- [10] Karina Jimenez-Garcia. *Artificial Gauge Fields for Ultracold Neutral Atoms*. PhD thesis, Joint Quantum Institute, National Institute of Standards and Technology, and the University of Maryland, 2012.
- [11] K. Jiménez-García, L. J. LeBlanc, R. A. Williams, M. C. Beeler, A. R. Perry, and I. B. Spielman. Peierls substitution in an engineered lattice potential. *Phys. Rev. Lett.*, 108:225303, May 2012.
- [12] Daniel Adam Steck. Quantum and atom optics. Available online at <http://steck.us/teaching>, January 2015. revision 0.12.2.
- [13] C.J. Pethick and H. Smith. *Bose-Einstein Condensation of Dilute Gases*. Oxford University Press, Oxford, UK, 2005.
- [14] M. Egorov, B. Opanchuk, P. Drummond, B. V. Hall, P. Hannaford, and A. I. Sidorov. Measurement of *s*-wave scattering lengths in a two-component bose-einstein condensate. *Phys. Rev. A*, 87:053614, May 2013.
- [15] W. Ketterle and M. W. Zwierlein. Making, probing and understanding ultracold Fermi gases. In *Ultracold Fermi Gases, Proceedings of the International School of Physics ‘Enrico Fermi’, Course CLXIV*, Varenna, 20-30 June 2006.

- [16] C. Chin, R. Grimm, P. Julienne, and E. Tiesinga. Feshbach resonances in ultracold gases. *Rev. Mod. Phys.*, 82:1225–1286, 2010.
- [17] M. Greiner, C. A. Regal, and D. S. Jin. Emergence of a molecular Bose-Einstein condensate from a Fermi gas. *Nature*, 426(6966):537–540, 2003.
- [18] M. W. Zwierlein, C. A. Stan, C. H. Schunck, S. M. F. Raupach, S. Gupta, Z. Hadzibabic, and W. Ketterle. Observation of Bose-Einstein condensation of molecules. *Phys. Rev. Lett.*, 91:250401, 2003.
- [19] S. Jochim, M. Bartenstein, A. Altmeyer, G. Hendl, S. Riedl, C. Chin, J. Hecker Denschlag, and R. Grimm. Bose-Einstein condensation of molecules. *Science*, 302(5653):2101–2103, 2003.
- [20] M. Bartenstein, A. Altmeyer, S. Riedl, S. Jochim, C. Chin, J. Hecker Denschlag, and R. Grimm. Collective excitations of a degenerate gas at the bec-bcs crossover. *Phys. Rev. Lett.*, 92:203201, 2004.
- [21] T. Bourdel, L. Khaykovich, J. Cubizolles, J. Zhang, F. Chevy, M. Teichmann, L. Tarruell, S. J. J. M. F. Kokkelmans, and C. Salomon. Experimental Study of the BEC-BCS Crossover Region in Lithium 6. *Phys. Rev. Lett.*, 93:050401, 2004.
- [22] M. W. Zwierlein, C. A. Stan, C. H. Schunck, S. M. F. Raupach, A. J. Kerman, and W. Ketterle. Condensation of pairs of Fermionic atoms near a Feshbach resonance. *Phys. Rev. Lett.*, 92:120403, 2004.
- [23] C. A. Regal, M. Greiner, and D. S. Jin. Observation of resonance condensation of fermionic atom pairs. *Phys. Rev. Lett.*, 92(4), 2004.

- [24] Y.-J. Lin, A. R. Perry, R. L. Compton, I. B. Spielman, and J. V. Porto. Rapid production of ^{87}Rb bose-einstein condensates in a combined magnetic and optical potential. *Phys. Rev. A*, 79:063631, Jun 2009.
- [25] Lauren M. Aycock. *Topological excitations in a Bose gas and sexual harassment reported by undergraduate physicists*. PhD thesis, Cornell University, Ithaca, NY, 1 2017.
- [26] Lauren M. Aycock, Hilary M. Hurst, Dmitry K. Efimkin, Dina Genkina, Hsin-I Lu, Victor M. Galitski, and I. B. Spielman. Brownian motion of solitons in a bose-einstein condensate. *Proceedings of the National Academy of Sciences*, 114(10):2503–2508, 2017.
- [27] Christopher J. Fott. *Atomic Physics*. Cambridge University Press, Cambridge, UK, 2002.
- [28] E. A. Donley, T. P. Heavner, F. Levi, M. O. Tataw, and S. R. Jefferts. Double-pass acousto-optic modulator system. *Review of Scientific Instruments*, 76(6):063112, 2005.
- [29] Ryan Price. *Phase transitions in engineered ultracold quantum systems*. PhD thesis, University of Maryland College Park, Digital Repository at the University of Maryland, 6 2016.
- [30] E. Majorana. Atomi orientati in campo magnetico variabile. *Nuovo Cimento*, 9:43–50, Feb 1932.
- [31] C. V. Sukumar and D. M. Brink. Spin-flip transitions in a magnetic trap. *Phys. Rev. A*, 56:2451–2454, Sep 1997.
- [32] D. M. Brink and C. V. Sukumar. Majorana spin-flip transitions in a magnetic trap. *Phys. Rev. A*, 74:035401, Sep 2006.

- [33] J. Catani, P. Maioli, L. De Sarlo, F. Minardi, and M. Inguscio. Intense slow beams of bosonic potassium isotopes. *Phys. Rev. A*, 73:033415, Mar 2006.
- [34] Thomas Uehlinger. A 2-d magneto-optical trap as a high flux source of cold potassium atoms. Master's thesis, Swiss Federal Institute of Technology Zurich, Zurich, 5 2008.
- [35] E. Pedrozo-Peafiel, F. Vivanco, P. Castilho, R. R. Paiva, K. M. Farias, and V. S. Bagnato. Direct comparison between a two-dimensional magneto-optical trap and a zeeman slower as sources of cold sodium atoms. *Laser Physics Letters*, 13:065501, May 2016.
- [36] K. J. Weatherill, J. D. Pritchard, P. F. Griffin, U. Dammalapati, C. S. Adams, and E. Riis. A versatile and reliably reusable ultrahigh vacuum viewport. *Review of Scientific Instruments*, 80(2):026105, 2009.
- [37] D. Rio Fernandes, F. Sievers, N. Kretzschmar, S. Wu, C Salomon, and F. Chevy. Sub-doppler laser cooling of fermionic 40k atoms in three-dimensional gray optical molasses. *Europhysics Letters*, 100:63001, Dec 2012.
- [38] D. Genkina, L. M. Aycock, B. K. Stuhl, H-I Lu, R. A. Williams, and I. B. Spielman. Feshbach enhanced s-wave scattering of fermions: direct observation with optimized absorption imaging. *New Journal of Physics*, 18:013001, Dec 2015.
- [39] Lindsey J. LeBlanc. *Exploring many-body physics with ultracold atoms*. PhD thesis, University of Toronto, 2011.
- [40] E. Tiesinga, B. J. Verhaar, and H. T. C. Stoof. Threshold and resonance phenomena in ultracold ground-state collisions. *Phys. Rev. A*, 47(5, B):4114–4122, 1993.

- [41] M. Lysebo and L. Veseth. *Ab initio* calculation of Feshbach resonances in cold atomic collisions: *s*- and *p*-wave Feshbach resonances in ${}^6\text{Li}_2$. *Phys. Rev. A*, 79:062704, 2009.
- [42] B. Gao. Analytic description of atomic interaction at ultracold temperatures. II. Scattering around a magnetic Feshbach resonance. *Phys. Rev. A*, 84:022706, 2011.
- [43] S. Inouye, M. R. Andrews, J. Stenger, H. J. Miesner, D. M. Stamper-Kurn, and W. Ketterle. Observation of Feshbach resonances in a Bose-Einstein condensate. *Nature*, 392(6672):151–154, 1998.
- [44] S. L. Cornish, N. R. Claussen, J. L. Roberts, E. A. Cornell, and C. E. Wieman. Stable Rb-85 Bose-Einstein condensates with widely tunable interactions. *Phys. Rev. Lett.*, 85(9):1795–1798, 2000.
- [45] C. A. Regal and D. S. Jin. Measurement of positive and negative scattering lengths in a Fermi gas of atoms. *Phys. Rev. Lett.*, 90:230404, 2003.
- [46] K. M. O’Hara, S. L. Hemmer, M. E. Gehm, S. R. Granade, and J. E. Thomas. Observation of a strongly interacting degenerate Fermi gas of atoms. *Science*, 298(5601):2179–2182, 2002.
- [47] C. Monroe, E. Cornell, C. Sackett, C. Myatt, and C. Wieman. Measurement of Cs-Cs elastic scattering at $T = 30 \mu\text{K}$. *Phys. Rev. Lett.*, 70:414–417, 1993.
- [48] B. DeMarco, J. L. Bohn, J. P. Burke, M. Holland, and D. S. Jin. Measurement of *p*-wave threshold law using evaporatively cooled fermionic atoms. *Phys. Rev. Lett.*, 82:4208–4211, 1999.
- [49] S. Wu, Y.-J. Wang, Q. Diot, and M. Prentiss. Splitting matter waves using an optimized standing-wave light-pulse sequence. *Phys. Rev. A*, 71:043602, 2005.

- [50] M. Edwards, B. Benton, J. Heward, and C. W. Clark. Momentum-space engineering of gaseous bose-einstein condensates. *Phys. Rev. A*, 82:063613, 2010.
- [51] K. v. Klitzing, G. Dorda, and M. Pepper. New method for high-accuracy determination of the fine-structure constant based on quantized hall resistance. *Phys. Rev. Lett.*, 45:494–497, Aug 1980.
- [52] Douglas R. Hofstadter. Energy levels and wave functions of bloch electrons in rational and irrational magnetic fields. *Phys. Rev. B*, 14:2239–2249, Sep 1976.
- [53] M. C. Geisler, J. H. Smet, V. Umansky, K. von Klitzing, B. Naundorf, R. Ketzmerick, and H. Schweizer. Detection of a landau band-coupling-induced rearrangement of the hofstadter butterfly. *Phys. Rev. Lett.*, 92:256801, Jun 2004.
- [54] B. Hunt, J. D. Sanchez-Yamagishi, A. F. Young, M. Yankowitz, B. J. LeRoy, K. Watanabe, T. Taniguchi, P. Moon, M. Koshino, P. Jarillo-Herrero, and R. C. Ashoori. Massive Dirac Fermions and Hofstadter Butterfly in a van der Waals Heterostructure. *Science*, 340:1427, 2013.
- [55] P. Zoller D. Jaksch. Creation of effective magnetic fields in optical lattices: the hofstadter butterfly for cold neutral atoms. *New Journal of Physics*, 5(1):56, 2003.
- [56] M. Aidelsburger, M. Atala, M. Lohse, J. T. Barreiro, B. Paredes, and I. Bloch. Realization of the hofstadter hamiltonian with ultracold atoms in optical lattices. *Phys. Rev. Lett.*, 111(18):185301–, October 2013.
- [57] Hirokazu Miyake, Georgios A. Siviloglou, Colin J. Kennedy, William Cody Burton, and Wolfgang Ketterle. Realizing the harper hamiltonian with laser-assisted tunneling in optical lattices. *Phys. Rev. Lett.*, 111:185302, Oct 2013.

- [58] Gregor Jotzu, Michael Messer, Remi Desbuquois, Martin Lebrat, Thomas Uehlinger, Daniel Greif, and Tilman Esslinger. Experimental realization of the topological haldane model with ultracold fermions. *Nature*, 515(7526):237–240, Nov 2014.
- [59] M Aidelsburger, M Lohse, C Schweizer, M Atala, J T Barreiro, S Nascimbène, N. R. Cooper, I. Bloch, and N. Goldman. Measuring the Chern number of Hofstadter bands with ultracold bosonic atoms. *Nature Physics*, 11(2):162–166, December 2014.
- [60] M. Mancini, G. Pagano, G. Cappellini, L. Livi, M. Rider, J. Catani, C. Sias, P. Zoller, M. Inguscio, M. Dalmonte, and L. Fallani. Observation of chiral edge states with neutral fermions in synthetic hall ribbons. *Science*, 349(6255):1510–, Sep 2015.
- [61] M Hafezi, S Mittal, J Fan, A Migdall, and J M Taylor. Imaging topological edge states in silicon photonics. *Nat. Photon.*, 7(12):1001–1005, October 2013.
- [62] A. Celi, P. Massignan, J. Ruseckas, N. Goldman, I.B. Spielman, G. Juzeliunas, and M. Lewenstein. Synthetic gauge fields in synthetic dimensions. *Phys. Rev. Lett.*, 112(4):043001–, Jan 2014.
- [63] B. K. Stuhl, H.-I. Lu, L. M. Aycock, D. Genkina, and I. B. Spielman. Visualizing edge states with an atomic bose gas in the quantum hall regime. *Science*, 349(6255):1514–, Sep 2015.
- [64] Y. Aharonov and D. Bohm. Significance of electromagnetic potentials in quantum theory. *Phys. Rev.*, 115:485, 1959.
- [65] Yakir Aharonov and Ady Stern. Origin of the geometric forces accompanying berry’s geometric potentials. *Phys. Rev. Lett.*, 69(25):3593–3597, 1992.

- [66] Dario Hügel and Belén Paredes. Chiral ladders and the edges of quantum Hall insulators. *Phys. Rev. A*, 89(2):023619, 2014.
- [67] Gretchen K. Campbell, Jongchul Mun, Micah Boyd, Erik W. Streed, Wolfgang Ketterle, and David E. Pritchard. Parametric amplification of scattered atom pairs. *Phys. Rev. Lett.*, 96:020406, Jan 2006.
- [68] Samuel Mugel, Alexandre Dauphin, Pietro Massignan, Leticia Tarruell, Maciej Lewenstein, Carlos Lobo, and Alessio Celi. Measuring chern numbers in hofstadter strips. *SciPost*, 2017.
- [69] Zhoushen Huang and Daniel P. Arovas. Entanglement spectrum and wannier center flow of the hofstadter problem. *Phys. Rev. B*, 86:245109, Dec 2012.
- [70] Xiong-Jun Liu, K. T. Law, T. K. Ng, and Patrick A. Lee. Detecting topological phases in cold atoms. *Phys. Rev. Lett.*, 111:120402, Sep 2013.
- [71] Lei Wang, Alexey A. Soluyanov, and Matthias Troyer. Proposal for direct measurement of topological invariants in optical lattices. *Phys. Rev. Lett.*, 110(16):166802–, Apr 2013.
- [72] Dan-Wei Zhang and Shuai Cao. Measuring the spin chern number in time-reversal-invariant hofstadter optical lattices. *Physics Letters A*, 380(42):3541–3545, Oct 2016.
- [73] Mahito Kohmoto. Zero modes and the quantized hall conductance of the two-dimensional lattice in a magnetic field. *Phys. Rev. B*, 39:11943–11949, Jun 1989.